



HAL
open science

Deep learning massively accelerates super-resolution localization microscopy

Wei Ouyang, Andrey Aristov, Mickaël Lelek, Xian Hao, Christophe Zimmer

► **To cite this version:**

Wei Ouyang, Andrey Aristov, Mickaël Lelek, Xian Hao, Christophe Zimmer. Deep learning massively accelerates super-resolution localization microscopy. *Nature Biotechnology*, 2018, 36 (5), pp.460-468. 10.1038/nbt.4106 . pasteur-02074397

HAL Id: pasteur-02074397

<https://pasteur.hal.science/pasteur-02074397>

Submitted on 5 Mar 2020

HAL is a multi-disciplinary open access archive for the deposit and dissemination of scientific research documents, whether they are published or not. The documents may come from teaching and research institutions in France or abroad, or from public or private research centers.

L'archive ouverte pluridisciplinaire **HAL**, est destinée au dépôt et à la diffusion de documents scientifiques de niveau recherche, publiés ou non, émanant des établissements d'enseignement et de recherche français ou étrangers, des laboratoires publics ou privés.

2 **ANNA-PALM: Deep learning accelerates super-resolution localization**
3 **microscopy by orders of magnitude**

4

5

6 Wei Ouyang^{1,2,3}, Andrey Aristov^{1,2,3}, Mickaël Lelek^{1,2,3}, Xian Hao^{1,2,3}, Christophe
7 Zimmer^{1,2,3}

8

9 ¹ Institut Pasteur, Unité Imagerie et Modélisation, Paris, France

10 ² UMR 3691, CNRS

11 ³ C3BI, USR 3756, IP CNRS

12

13

14

15

16

17

18

19

20

21

22

23 Corresponding author: C. Zimmer

24 **The speed of super-resolution microscopy methods based on single molecule**
25 **localization, e.g. PALM or STORM, is severely limited by the need to record**
26 **many thousands of frames with a low number of observed molecules in each.**
27 **Here, we present ANNA-PALM, a computational strategy that uses artificial**
28 **neural networks to reconstruct super-resolution views from sparse, rapidly**
29 **acquired localization images and/or widefield images. Simulations and**
30 **experimental imaging of microtubules, nuclear pores and mitochondria show**
31 **that high-quality super-resolution images can be reconstructed from up to two**
32 **orders of magnitude fewer frames than usually needed, without**
33 **compromising spatial resolution. Super-resolution reconstructions are even**
34 **possible from widefield images alone, though adding localization data**
35 **improves image quality. We demonstrate super-resolution imaging of >1,000**
36 **fields of view containing >1,000 cells in ~3 h, yielding an image spanning**
37 **spatial scales from ~20 nm to ~2 mm. The drastic reduction in acquisition**
38 **time and sample irradiation afforded by ANNA-PALM enables faster and**
39 **gentler high-throughput and live cell super-resolution imaging.**

40
41 Fluorescence microscopy methods that overcome the diffraction limit of resolution
42 (~200-300 nm) allow imaging of biological structures with molecular specificity
43 closer to the molecular scale. Among super-resolution microscopy approaches,
44 those based on single molecule localization, such as PALM¹ or STORM² (hereafter
45 referred to collectively as PALM) are particularly attractive owing to their exquisite
46 spatial resolution and ease of implementation. In these methods, random subsets of
47 fluorophores are imaged in many consecutive diffraction-limited frames,
48 computationally localized to high precision, and the combined localizations are used
49 to generate a super-resolution view. In practice, typically 10^3 - 10^5 diffraction-limited
50 frames are needed to assemble a single super-resolution image. This requirement
51 follows from two conditions that must be simultaneously satisfied to ensure high
52 spatial resolution: (i) a low number (~ 10 - 10^2) of active fluorophores per frame, to
53 avoid overlaps between diffraction limited spots and enable precise localization of
54 individual molecules, and (ii) a large number of independent localizations to ensure
55 a sufficiently dense sampling of the underlying biological structures^{3,4}. The large
56 number of required frames makes localization microscopy inherently slow, thereby
57 limiting its potential for high-throughput imaging, where many fields of view (FoVs)
58 are to be imaged, and for imaging live cell dynamics. As a result, most localization
59 microscopy studies are restricted to analyzing a small number of cells (typically less
60 than ten).

61 Multiple approaches have been explored to accelerate localization
62 microscopy. Using bright dyes with rapid switching kinetics, high power lasers and
63 fast cameras allows to minimize exposure time without losing signal to noise

64 ratio^{5,6}, but reaching sub-millisecond exposure remains challenging, and intense
65 irradiation exacerbates phototoxicity in live cell imaging^{7,8}. Increasing the number
66 of active fluorophores per frame can reduce acquisition time, but despite algorithms
67 designed to handle overlapping fluorescent spots⁹⁻¹³ this approach necessarily
68 compromises spatial resolution^{14,15}.

69 Here, we introduce a computational strategy that allows reducing the total
70 number of frames and independent localizations without losing spatial resolution.
71 Unlike previous approaches, our method leverages the structural redundancy of
72 most biological images to reconstruct high quality images from vastly under-
73 sampled localization microscopy data. Our method leverages deep learning, which
74 employs artificial neural networks (ANNs) to learn complex non-linear mappings
75 between numerical inputs and outputs¹⁶. Accordingly, we call it ‘artificial neural
76 network accelerated PALM’, or ANNA-PALM.

77

78 **RESULTS**

79 **A deep learning approach to super-resolution image reconstruction**

80 We aim to reconstruct a super-resolution image of approximately similar
81 information content as a standard PALM acquisition (with K frames and N
82 localizations) from a much smaller number of raw frames ($k \ll K$) without changing
83 the average density of localizations, ρ , i.e. from a much smaller number of total
84 localizations ($n = \rho k \ll N = \rho K$). If PALM images are defined as 2D histograms of
85 independent localizations, this task can be formulated as restoring an image
86 corrupted by Poisson noise (and potentially additional forms of noise). Image

87 restoration is an ill-posed problem that has an infinity of solutions in the high-
88 dimensional space of all possible images, unless additional constraints (priors) are
89 imposed that restrict the solution to a lower dimensional subspace. Suitable
90 subspaces exist because most natural images are highly redundant, and can be
91 represented to very good approximation with a much smaller number of coefficients
92 than pixels, via appropriate functions that map feature space to pixel space^{17,18}. In
93 recent years, ANNs with multiple layers (deep nets) have proven very successful at
94 learning meaningful features and non-linear mappings for image classification,
95 segmentation, restoration and many other tasks^{16,18,19}. Inspired by these
96 developments, we designed ANNA-PALM, a deep learning approach for restoring
97 super-resolution views from under-sampled (sparse) localization microscopy data.

98 ANNA-PALM comprises a training stage and an inference stage (**Figure 1**).
99 For training (**Figure 1a**), a few super-resolution images representative of the
100 structure of interest (e.g. microtubules, nuclear pores, or mitochondria) are
101 obtained using standard PALM imaging, i.e. by acquiring long diffraction limited
102 image sequences (e.g. $K \sim 10^4 - 10^5$, $N \sim 10^5 - 10^7$) and processing them with
103 standard localization software²⁰, resulting in highly sampled (dense) PALM images.
104 In addition, a low resolution (widefield) image can also be acquired, as is commonly
105 done before single molecule imaging when bleaching out preactivated fluorophores.
106 Next, the dense PALM images are under-sampled by using a much smaller number
107 of input frames, $k \ll K$, thus yielding sparse PALM images from the same
108 localization data. Then, an ANN is trained to recover approximations of the dense
109 PALM images from these sparse PALM images (and the optional widefield image).

110 Once trained, the ANN is applied to new sparse PALM images (with or without a
111 widefield image), obtained from new image sequences with small numbers of
112 frames ($k \ll K$) -and hence in much shorter time- in order to reconstruct high
113 quality super-resolution images not previously seen (inference, **Figure 1b**).

114

115 **Neural net architecture and learning strategy**

116 Our ANN, hereafter called A-net, contains a total of 25 convolutional layers, and
117 roughly 42 million trainable parameters. A-net is adapted from the pix2pix
118 network²¹, which itself builds on U-nets²² and generative adversarial networks
119 (GANs)²³, two recent successful deep learning techniques. U-nets are special types of
120 convolutional neural networks (CNNs) that have proven effective at learning multi-
121 scale representations of images and accurate, pixel-wise mappings^{22,24}. GANs can
122 generate new samples from real image distributions using a generator network that
123 outputs synthetic images, and a discriminator network that outputs the probability
124 that an input image is real or synthetic, both networks being trained simultaneously
125 to compete against each other²³. Importantly, the generator can be conditioned on
126 input data (conditional GAN, or cGAN)^{21,23}, e.g. on images as in the pix2pix network.
127 We modified the pix2pix architecture to accept a computational switch as additional
128 input to handle multiple types of data, and introduced an additional network to
129 evaluate the consistency between the reconstructed image and the widefield input
130 image.

131 Training of our A-net proceeds as follows. Randomly under-sampled (i.e.
132 sparse) versions of PALM images are fed as input to the A-net, while the

133 corresponding dense PALM images are defined as the A-net’s targets, i.e. desired
134 outputs (**Figure 1a**). Additional, optional inputs are widefield images, if available,
135 and the switch, which indicates the image type when multiple types of images (e.g.
136 microtubules and nuclear pores) are used during training. ANN training requires
137 defining an objective function (also called loss), which measures how well the
138 outputs match the targets. We implemented a loss function containing three terms.
139 The first term measures the difference between the A-net output and the dense
140 PALM image. Instead of the widely used mean squared error (MSE), which poorly
141 reflects visual quality²⁵, we used a combination of the absolute difference (L1 norm)
142 with a multi-scale version of the structural similarity index, a perceptually
143 motivated quality metric shown to improve image restoration with deep learning
144 (MS-SSIM)²⁶. The second term measures the consistency between the A-net output
145 and the widefield image. Although in theory the latter should simply be a blurred
146 version of the PALM image, this is often not the case in practice²⁷. Therefore, we
147 introduced another CNN (with 4-layers), called ‘low resolution estimator’ to predict
148 the widefield image from the super-resolution image. The corresponding loss was
149 defined as the MS-SSIM between this CNN’s output and the observed widefield
150 image. (In absence of a widefield image, this loss is set to zero). The third term
151 contains a cGAN discriminator loss²¹, where the discriminator is a 5-layer CNN,
152 whose inputs are the sparse PALM (and widefield) image(s) and either the dense
153 PALM image or the output of the generator above; the discriminator’s output is
154 compared to 0s and 1s (for synthetic and real, respectively), respectively, via the
155 MSE. We use dropout²⁸ and extensive data augmentation, including random

156 rotations, translations, elastic deformations and addition of noise in the input image
157 to mimic false detections and unspecific labeling. As a result, only a few dense PALM
158 images are required for successful training without overfitting. On graphical
159 processing units (GPU), training ANNA-PALM from scratch takes on the order of
160 hours to days, but when starting from a previously trained A-net, retraining can be
161 done in an hour or less.

162 Once trained, the A-net can take sparse localization data with an optional
163 widefield image as input(s), and output a reconstructed super-resolution image in
164 less than a second (**Figure 1b**). In addition, the A-net produces an ‘error map’ that
165 measures the consistency of this super-resolution image with the widefield image²⁷
166 (when available) and can be used to estimate the degree of reliability and highlight
167 potential reconstruction artifacts. For more details, see **Online Methods** and
168 **Supplementary Note 1**.

169

170 **Validating ANNA-PALM on simulated images**

171 We first sought to validate ANNA-PALM on synthetic data. For this, we used
172 Brownian dynamics simulations²⁹ to generate 200 dense PALM images of semi-
173 flexible filaments mimicking microtubules, with a resolution $R_{loc} \approx 23$ nm. These
174 represent “perfect” PALM images that would be obtained with an infinite number of
175 localizations. We applied varying levels of Poisson noise to these perfect images to
176 create sparse PALM images corresponding to finite numbers of localizations
177 (**Supplementary Figure 1**). We then trained our A-net using the perfect images as

178 targets and the sparse images (and widefield image) as inputs, varying the number
179 of localizations over a large range.

180 Next, we applied the trained A-net to a distinct set of PALM images generated
181 by the same stochastic simulation (**Supplementary Figure 2**). **Figure 2a** shows a
182 widefield image and **Figure 2b** a corresponding sparse PALM image obtained from
183 $n=6,834$ localizations. Although curvilinear structures can be seen in this image
184 despite its sparsity, small-scale features remain highly ambiguous (**Figure 2b**,
185 inset), and the resolution according to a recently proposed five-fold Nyquist
186 criterion³ is limited by sampling to $R_{5 \times Nyq} \approx 85$ nm; according to this criterion,
187 $N > N_{5 \times Nyq} = 60,000$ localizations are needed to achieve 23 nm resolution
188 (**Supplementary Figure 3d**). **Figure 2c** shows the ANNA-PALM image
189 reconstructed from the wide-field image alone, which exhibits clear and continuous
190 filaments that were not previously recognizable. Most of the relatively isolated
191 filaments roughly agree with the perfect PALM image (**Figure 2e**). In the denser
192 regions, however, many small features are erroneous, e.g. filaments are incorrectly
193 joined, displaced, split or merged (**Figure 2c**, blue arrows and **Supplementary**
194 **Figure 4, top**). By contrast, the ANNA-PALM image reconstructed from the sparse
195 PALM image alone or in combination with the widefield image exhibits continuous
196 and sharp filaments in very good agreement with the perfect PALM image
197 (**Supplementary Figure 3b,c** and **Figure 2d,e,f**). The spatial resolution of these
198 reconstructed images is limited neither by diffraction nor sampling, but only by the
199 localization precision, and is thus $R_{loc} \approx 23$ nm, as in the perfect images
200 (**Supplementary Figure 3e,f**). These results indicate that high quality super-

201 resolution images can be obtained from only a small fraction of the number of
202 localizations traditionally required (here, approximately $\sim 11\%$ of $N_{5\times Nyq}$ above; see
203 **Supplementary Figure 3d**), hence enabling a strong reduction in acquisition time.
204 Nevertheless, reconstruction errors can still occur in areas where the sparse
205 localization data are most ambiguous, e.g. where filament density is highest
206 (**Figure 2d,e,f**, white arrow). These errors can be reduced by increasing the
207 localization number n , implying a trade-off between acquisition time and
208 reconstruction quality (**Supplementary Figure 4**).

209 To quantify this trade-off, we computed the MS-SSIM between reconstructed
210 ANNA-PALM and perfect PALM images ($n = \infty$) as function of localization number,
211 from $n \sim 200$ to $n \sim 2 \times 10^6$, in comparison with the standard PALM images
212 (**Figure 2g**). The MS-SSIM ranges from 0 to 1 and reaches 1 for perfect
213 reconstructions. For standard PALM images, the MS-SSIM increases monotonically,
214 as expected, from < 0.2 to > 0.95 for $n = 2 \times 10^6$ million localizations (**Figure 2g**, black
215 curve). Using only the sparse image as input, ANNA-PALM reconstructions achieve
216 MS-SSIM that are consistently higher and increase with localization number n much
217 more rapidly than standard PALM, already exceeding 0.9 for $n \approx 10,000$
218 localizations (**Figure 2**, dashed blue curve). ANNA-PALM achieves the same MS-
219 SSIM as standard PALM at the five-fold Nyquist sampling level (≈ 0.65) with only
220 $n = 2,248$ localizations instead of $n = 58,588$, suggesting a ~ 26 -fold speed-up. If the
221 widefield image is used as additional input, the MS-SSIM further increases, and
222 dramatically so for low localization numbers (**Figure 2g**, solid blue curve). For
223 example, with $n = 7,477$ localizations, ANNA-PALM achieves a MS-SSIM (≈ 0.95)

224 similar to standard PALM with $n = 644,844$, implying a speed-up of roughly two
225 orders of magnitude. (Note that, if the perfect PALM image was not available for
226 these quantifications, it could be replaced by the ANNA-PALM reconstruction of a
227 dense PALM image with a large number of localizations, e.g. $n = 10^5$, with similar
228 results- see **Supplementary Figure 5**).

229 As any image restoration method, ANNA-PALM can make errors. The low
230 resolution error map described above (**Figure 1b**) provides a means to estimate
231 where errors are most likely to occur. When applied to ANNA-PALM reconstructions
232 of a sparse PALM image, this error map highlights regions containing the highest
233 density of filament crossings, where reconstructions tend to be least accurate
234 (**Supplementary Figure 6i,k**). If we artificially displace a small piece of filament in
235 this image to simulate a false positive and a false negative in the reconstruction
236 (**Supplementary Figure 6b,d**, white and blue arrows, respectively), the affected
237 regions also light up in the error map (**Supplementary Figure 6j,l**). Thus, the error
238 map offers a useful tool to highlight regions most likely to contain reconstruction
239 errors, and conversely, to outline regions where reconstructions are most
240 trustworthy. Thus, simulations suggest that ANNA-PALM can considerably reduce
241 acquisition time in localization microscopy and also map reconstruction reliability.

242

243 **ANNA-PALM reconstructions of immunostained microtubules**

244 We next tested our method on real images of immunolabeled microtubules
245 (**Figure 3**). We trained our A-net on seven dense PALM images (with corresponding
246 widefield images) obtained during 10 minute long acquisitions ($K=60,000$;

247 $\Delta t=10$ ms exposure time) (not shown). We then considered a sparse PALM image of
248 microtubules in a distinct FoV obtained from only 9 s of acquisition ($k=300$; $\Delta t=30$
249 ms), together with a widefield image ($\Delta t=2 \times 50$ ms) (**Figure 3a,b**). Whereas
250 microtubule filaments can already be seen in this sparse PALM image, structural
251 details below the diffraction limit are hard to discern, making it difficult to follow
252 the path of individual filaments in the denser regions and to identify features such
253 as filament crossings (**Figure 3b**). By contrast, the ANNA-PALM images, whether
254 reconstructed from the widefield image alone, the sparse PALM image alone, or
255 both, all display sharp and continuous filaments and clearly reveal many structural
256 details (**Figure 3d-f**). Their resolution is similar to or even better than the dense
257 PALM image (**Supplementary Figure 7a**). As for the simulations, in regions where
258 microtubule filaments are isolated, the ANNA-PALM image reconstructed from the
259 widefield image alone is in good agreement with the dense PALM image
260 (**Figure 3d,g**). However, it is often incorrect in areas of high microtubule density
261 (e.g. **Figure 3d,g** white and gray arrows). Most of these reconstruction errors are
262 corrected when applying ANNA-PALM to the sparse PALM image instead
263 (**Figure 3e,h**). For example, parallel sections of two microtubules unresolved in the
264 widefield image and incorrectly merged in **Figure 3d** are now clearly separated and
265 positioned correctly, and missed portions of other filaments are now recovered
266 (**Figure 3h**, white and gray arrows). Counter-intuitively, the sparse PALM image
267 exhibits high signal in some locations where the dense PALM image does not,
268 presumably because of spurious localizations due e.g. to unspecific binding
269 (**Figure 3b**, blue arrow). Such signal can lead to incorrect features in the ANNA-

270 PALM reconstruction from the sparse localization data alone (**Figure 3e,h**, blue
271 arrows). However, when combining the widefield and sparse PALM data, these
272 artifacts are largely removed and reconstructions agree very well with the dense
273 PALM image (**Figure 3f,i**). Reconstruction quality increases with the number of
274 frames k (**Figure 3j**, **Supplementary Figures 8-9** and **Supplementary Video 1**).
275 More quantitatively, a MS-SSIM analysis similar to that for the simulated data above
276 (with the ANNA-PALM output of the dense PALM image defined as ground truth; see
277 **Supplementary Figures 5, 9f**) suggests that ANNA-PALM allows a hundred-fold
278 reduction of acquisition time compared to standard PALM (**Supplementary**
279 **Figure 9g**). **Supplementary Figure 10** shows other examples of sparse
280 microtubule images reconstructed by ANNA-PALM.

281 As for simulations above, we used the widefield image to compute an error
282 map (**Supplementary Figures 6,11**). Bright areas in this error map highlight
283 regions where the reconstruction indeed disagrees with the dense PALM image;
284 conversely, reconstructions are of high quality in the majority of regions where the
285 error map is dim (**Supplementary Figure 11d-f**). These results demonstrate
286 experimentally that ANNA-PALM can restore high quality approximations of super-
287 resolution images from much shorter acquisition time than typical for PALM
288 imaging, and also predict where reconstruction errors are most likely.

289

290 **ANNA-PALM enables high-throughput super-resolution imaging**

291 The drastic improvement in imaging efficiency afforded by ANNA-PALM permits
292 super-resolution imaging of orders of magnitude more cells and FoVs per unit time.

293 To demonstrate this, we used an automated acquisition protocol to image >1,000
294 cells with immunolabeled microtubules in 1,089 (33x33), partly overlapping, FoVs
295 of 55.3 μm x 55.3 μm each (**Figure 4, Supplementary Figure 12**). We first acquired
296 widefield images at each of these positions, in a total of \sim 12 minutes, mostly
297 consisting of stage stabilization delays (**Supplementary Figure 12a**). Next, we
298 obtained 1,089 sparse PALM images using only 10 s of imaging time per FoV
299 ($k=1,000$ frames, $\Delta t = 10$ ms), in a total of only \sim 3.1 hours (**Figure 4a**). Neither the
300 widefield nor the sparse PALM images provided much small scale information
301 (**Figure 4c, Supplementary Figure 12 c,e**). However, ANNA-PALM reconstructions
302 led to high quality super-resolution images, allowing to visualize the microtubule
303 network with clarity and to distinguish microtubule filaments in dense areas that
304 appeared as unstructured regions in the sparse PALM image (**Figure 4b,d**). The
305 FWHM across filaments in the reconstructed image was \sim 51 nm (**Figure 4d**), within
306 the range measured for the training data (**Supplementary Figure 7a**). Similar
307 images can be obtained by ANNA-PALM using the widefield images alone
308 (**Supplementary Figure 12**), although of lower quality, as discussed above.
309 Stitching the reconstructed images together yielded a single super-resolution image
310 that contained approximately seven billion 20x20 nm pixels and covered an area of
311 1.8 mm x 1.8 mm, thereby spanning almost five orders of magnitude in spatial scales
312 (**Figure 4b,d, Supplementary Figure 12b and Supplementary Video 2**).

313

314 **ANNA-PALM is robust to experimental perturbations**

315 ANNA-PALM can reconstruct accurate super-resolution images from sparse data
316 because it was trained on similar images before. This raises the question of whether
317 an ANN trained in one experimental condition can be successfully applied to
318 another condition. To test this, we used the A-net as trained above to analyze
319 microtubule images of cells subjected to drugs affecting the cytoskeletal network.
320 We first treated U373 cells with 1 μ M of Taxol, an antimetabolic agent that inhibits the
321 depolymerization of microtubules and increases their bending rigidity^{30,31}.
322 **Figure 5d** shows a sparse PALM image of these cells ($k=800$, $k\Delta t=8$ s), in which the
323 microtubule network is barely recognizable. By contrast, the ANNA-PALM
324 reconstructions clearly display a complex microtubule network and agree well with
325 the dense PALM image obtained from $K=60,000$ frames ($K\Delta t=10$ min)
326 (**Figure 5d,e,f**). These images display a larger density of straighter and more
327 parallel filaments with less frequent crossings than in the untreated cells
328 (**Figure 5a-c**), consistent with microtubule stabilization and increased rigidity³¹.

329 Next, we treated cells with 1 μ M of Nocodazole, a drug that, on the opposite,
330 promotes microtubule depolymerization and is expected to more dramatically alter
331 the cytoskeletal network³². Again, whereas the sparse image obtained from $k=300$
332 frames ($k\Delta t=3$ s) contained little exploitable information (**Figure 5g**), the ANNA-
333 PALM reconstruction offered clear and detailed views of the disrupted microtubule
334 network (**Figure 5h**), exhibiting a much smaller number of filaments, with higher
335 curvature, than in untreated cells. These reconstructions were in good (though not
336 perfect) agreement with dense PALM images obtained from $K=60,000$ frames
337 ($K\Delta t=10$ min) (**Figure 5i**). Thus, ANNA-PALM, when trained on microtubules in

338 one experimental condition, may be successfully applied to new experimental
339 conditions without retraining, thereby highlighting the method's robustness to
340 biologically relevant structural alterations.

341 We further asked if ANNA-PALM is robust to changes in technical imaging
342 conditions. To address this, we performed localization microscopy on microtubules
343 by simultaneously changing multiple important imaging parameters relative to the
344 training data. Instead of PALM/STORM, we used DNA-PAINT a technique where
345 single molecule detection relies on transient binding of fluorophore-conjugated
346 short DNA strands to complementary, antibody-conjugated, DNA strands³³, rather
347 than on fluorophore blinking. The continuously emitting freely diffusing dyes lead to
348 higher background noise in DNA-PAINT compared to PALM/STORM. Moreover, we
349 used primary mouse antibodies instead of rat antibodies, Cy3 dyes instead of Alexa-
350 647 dyes, and an EMCCD instead of a sCMOS camera. Despite all these differences,
351 when ANNA-PALM was applied without retraining on a sparse microtubule image
352 ($k=400$ frames, $k\Delta t=12$ s) , the reconstructed image still agreed very well with the
353 dense DNA-PAINT image obtained from $K=60,000$ frames ($K\Delta t=30$ min) (**Figure 5j-**
354 **I**). These data demonstrate the high robustness of ANNA-PALM to changes in
355 experimental imaging conditions.

356

357 **ANNA-PALM adapts to different biological structures**

358 To demonstrate that ANNA-PALM is not restricted to filamentary structure, we
359 turned to nuclear pores, a very different biological structure, and another popular
360 target of super-resolution imaging studies³⁴⁻³⁶. We retrained A-net simultaneously

361 on microtubule images and on a single PALM image of the nucleoporin gp210 in
362 immunolabeled nuclear membranes of *Xenopus* frog eggs^{34,36} ($K=30,000$). With the
363 switch (**Figure 1**) set to microtubules ('MT'), this newly trained A-net can still
364 reconstruct sparse images of microtubules as when trained exclusively on
365 microtubule data (**Supplementary Figure 13a-c**). We then applied the same A-net
366 with the switch set to nuclear pores ('NPC') to reconstruct a new sparse PALM
367 image of gp210 obtained from the first $k=3,000$ frames (**Figure 6a**). The sparsity of
368 this image makes it difficult to clearly distinguish individual nuclear pores. ANNA-
369 PALM, however, reconstructs a much clearer image, containing many easily
370 identifiable ring-like structures, as expected for nuclear pores³⁴ (**Figure 6b**), and in
371 good agreement with the dense PALM image obtained from $K=30,000$ frames (even
372 though the latter shows mostly incomplete, open rings, presumably due to
373 suboptimal labeling) (**Figure 6c**). An automated procedure based on cross-
374 correlation with a ring template indeed identified ~ 2.7 times more putative nuclear
375 pores from the ANNA-PALM image than the sparse image (**Supplementary Figure**
376 **14a-c**). Moreover, computed pore locations were in good agreement with a PALM
377 image of wheat germ agglutinin (WGA), a lectin that concentrates in the inner
378 nuclear pore channel³⁶ (**Supplementary Figure 14 d-f**). These results show that
379 ANNA-PALM can successfully analyze non-filamentary structures, when properly
380 retrained, and that a single ANN, with a simple computational switch, can
381 reconstruct very different types of structures.

382 Finally, we imaged TOM22, a protein of the mitochondrial outer membrane³⁷.
383 Whereas, at the resolution of our experiments, microtubules and nucleoporins are

384 essentially one-dimensional and zero-dimensional structures, mitochondrial
385 membranes are two-dimensional surfaces. Furthermore, their complex 3D
386 morphology might seem less predictable than filaments or nuclear pores, potentially
387 hampering ANNA-PALM reconstruction. Despite these differences, after being
388 trained on nine PALM images of TOM22 (with frame numbers ranging from
389 $K=24,000$ to $K=40,000$), ANNA-PALM reconstructions of distinct sparse PALM
390 images ($k=400$ frames) displayed mitochondrial morphologies in good agreement
391 with the dense PALM images (**Figure 6d-f**) - although the protein's localization
392 along the membrane was less well reproduced. Taken together, our results illustrate
393 the versatility of ANNA-PALM and its applicability to images of very different
394 structural content.

395

396 **Discussion**

397 We introduced ANNA-PALM, a computational method based on deep learning, that
398 reconstructs high quality super-resolution images from sparse, rapidly acquired,
399 single molecule localization data (and/or widefield images). Our method enables
400 considerable gains in acquisition time compared to standard localization
401 microscopy without increasing active fluorophore density, thereby preserving
402 spatial resolution. In fact, ANNA-PALM even improves spatial resolution when
403 applied to images of lower resolution than the training data
404 (**Supplementary Figures 7a, 10**), and greatly diminishes the detrimental effect of
405 drift. The improvement in imaging efficiency afforded by ANNA-PALM alleviates the
406 incompatibility between high resolution and high-throughput microscopy by

407 enabling super-resolution imaging of thousands of cells within a few hours or even
408 less (**Figure 4, Supplementary Figure 12**). This will facilitate super-resolution
409 studies of rare events, cellular heterogeneity and of partly stochastic structures such
410 as cytoskeletal polymers or chromosomes, whose characterization requires
411 statistics on many configurations^{38,39}. ANNA-PALM may also be beneficial for high-
412 throughput imaging screens, e.g. of drug treatments or gene knock-outs⁴⁰⁻⁴². In
413 addition, we envision applications to super-resolution imaging of large samples by
414 stitching together multiple images of spatially adjacent fields. The ability to generate
415 images spanning many orders of magnitude in scale could be well adapted to
416 expansion microscopy, a super-resolution technique that physically increases
417 sample size, but often requires tiling many fields of view to image even a single
418 cell^{43,44}. With correlative microscopy⁴⁵, it might also be possible to train ANNA-
419 PALM to reconstruct electron microscopy (EM) images from fluorescence images,
420 potentially extending the method to molecular resolutions currently out of reach of
421 localization microscopy. Adaptation of ANNA-PALM to 3D^{15,46} and multi-color^{47,48}
422 localization microscopy should be relatively straightforward. Localization
423 microscopy of cellular dynamics remains very challenging^{3,49}. By using much fewer
424 frames (or even only widefield images), ANNA-PALM could dramatically improve
425 the temporal resolution of live cell localization microscopy without sacrificing
426 spatial resolution or increasing phototoxicity and photobleaching. Thus, ANNA-
427 PALM provides multiple novel avenues for multi-scale imaging beyond standard
428 spatio-temporal resolution limits.

429 Nevertheless, important caveats should be stressed. First, although ANNA-
430 PALM can be applied successfully to very different types of images (**Figure 6**), the
431 method fails in absence of statistical redundancies between molecular localizations,
432 e.g. for entirely random distributions of molecules. Second, ANNA-PALM requires
433 prior training on dense PALM images with structures similar to those in the images
434 to be reconstructed. We showed that ANNA-PALM is robust, i.e. does not require
435 retraining, for some experimentally induced changes in structures and variations in
436 imaging parameters (**Figure 5**). Nevertheless, indiscriminate application of ANNA-
437 PALM to very different structures without retraining, or incorrect setting of the
438 switch, may result in artifacts (**Supplementary Figure 13h**). Third, even when
439 applied to data similar to the training images, ANNA-PALM can produce errors -as
440 any reconstruction method in a context of information scarcity. The frequency of
441 errors can be reduced by increasing the number of recorded frames, at the cost of
442 reduced acceleration (see **Figures 2,3** and **Supplementary Figures 4, 8, 9**). In
443 addition, ANNA-PALM can use widefield images to estimate the reliability of
444 reconstructions, thereby helping their interpretation, providing some protection
445 against artifacts and indicating when retraining may be needed (**Supplementary**
446 **Figures 11, 15**). Future work, e.g. using Bayesian deep learning⁵⁰, may provide
447 additional assessments of reconstruction uncertainty and shed more light on the
448 scope and limitations of our approach.

449 As a purely computational technique, ANNA-PALM does not necessitate any
450 changes to existing microscopy systems, but only requires one or a few standard
451 PALM images for training. To facilitate its adoption and future development, we

452 make our source code, an ImageJ plugin and a cloud-computing based web
453 application available on <https://annapalm.pasteur.fr/> along with sample data.
454 Because the performance of deep learning methods improves with the amount and
455 variety of training data, we designed our web application to enable sharing of data
456 and trained ANNs. As ANNA-PALM will learn from an increasing large and diverse
457 collection of images, we expect it to reach even higher accuracy or efficiency and to
458 expand its scope of application in the future.

459

460

461 **Acknowledgements**

462 We thank the following colleagues for useful discussions and suggestions and/or
463 critical reading of the manuscript: C. Leduc, S. Etienne-Manneville, S. Lévêque-Fort,
464 N. Bourg, A. Echard, J-B. Masson, T. Rose, P. Hersen, F. Mueller, M. Cohen, Z. Zhang,
465 and P. Kanchanawong. We also thank the four anonymous reviewers for their
466 constructive criticism, which led to significant improvements of ANNA-PALM. We
467 further thank O. Faklaris, J. Sellés and M. Penrad (Institut Jacques Monod), and F.
468 Montel (Ecole Normale Supérieure de Lyon) for providing *Xenopus* nuclear pore
469 data, B. Jian (Institut Pasteur) for TOM22 antibodies, and C. Leterrier for fixation
470 protocols. We thank E. Rensen and C. Weber for help with experiments and
471 suggestions, B. Lelandais for help with PALM image processing, J-B. Arbona for
472 polymer simulations and J. Parmar for suggestions that led to the name ANNA-
473 PALM. We thank the IT service of Institut Pasteur, including J-B. Denis, N. Joly, and S.
474 Fournier, for access to the HPC cluster and relevant assistance, and T. Huynh for
475 help with GPU computing. This work was funded by Institut Pasteur, Agence

476 Nationale de la Recherche grant (ANR 14 CE10 0018 02), Fondation pour la
477 Recherche Médicale (Equipe FRM, DEQ 20150331762), and the Région Ile de France
478 (DIM Malinf). We also acknowledge Investissement d’Avenir grant ANR-16-CONV-
479 0005 for funding a GPU farm used in this work. A.A. and X.H. are recipients of
480 Pasteur-Roux fellowships from Institut Pasteur. W.O. is a scholar in the Pasteur -
481 Paris University (PPU) International PhD program.

482
483

484 **Author contributions**

485 W.O.: conceived method, developed ANNA-PALM software and web application,
486 performed experiments and analyses. A.A., M.L., X.H.: performed experiments. C.Z.:
487 conceived method, supervised project and wrote manuscript.

488
489

490 **Competing financial interests statement**

491 W.O. and C.Z. are listed as inventors on European patent application EP17306022
492 filed by Institut Pasteur.

493
494

495 **REFERENCES**

496

- 497 1. Betzig, E. *et al.* Imaging intracellular fluorescent proteins at nanometer
498 resolution. *Science (80-.)*. **313**, 1642–1645 (2006).
- 499 2. Rust, M. J., Bates, M. & Zhuang, X. Sub-diffraction-limit imaging by stochastic
500 optical reconstruction microscopy (STORM). *Nat Methods* **3**, 793–795 (2006).
- 501 3. Legant, W. R. *et al.* High-density three-dimensional localization microscopy
502 across large volumes. *Nat. Methods* **13**, 359–365 (2016).
- 503 4. Deschout, H. *et al.* Precisely and accurately localizing single emitters in
504 fluorescence microscopy. *Nat. Methods* **11**, 253–266 (2014).
- 505 5. Jones, S. A., Shim, S. H., He, J. & Zhuang, X. Fast, three-dimensional super-
506 resolution imaging of live cells. *Nat Methods* **8**, 499–505 (2011).
- 507 6. Huang, F. *et al.* Video-rate nanoscopy using sCMOS camera-specific single-
508 molecule localization algorithms. *Nat. Methods* **10**, 653–8 (2013).
- 509 7. Carlton, P. M. *et al.* Fast live simultaneous multiwavelength four-dimensional
510 optical microscopy. *Proc. Natl. Acad. Sci. U. S. A.* **107**, 16016–22 (2010).
- 511 8. Stelzer, E. H. K. Light-sheet fluorescence microscopy for quantitative biology.
512 *Nat. Methods* **12**, 23–26 (2014).
- 513 9. Huang, F., Schwartz, S. L., Byars, J. M. & Lidke, K. A. Simultaneous multiple-
514 emitter fitting for single molecule super-resolution imaging. *Biomed. Opt.*
515 *Express* **2**, 1377–93 (2011).
- 516 10. Burnette, D. T., Sengupta, P., Dai, Y., Lippincott-Schwartz, J. & Kachar, B.
517 Bleaching/blinking assisted localization microscopy for superresolution
518 imaging using standard fluorescent molecules. *Proc Natl Acad Sci U S A* **108**,
519 21081–21086 (2011).
- 520 11. Simonson, P. D., Rothenberg, E. & Selvin, P. R. Single-molecule-based super-
521 resolution images in the presence of multiple fluorophores. *Nano Lett* **11**,
522 5090–5096 (2011).
- 523 12. Zhu, L., Zhang, W., Elnatan, D. & Huang, B. Faster STORM using compressed
524 sensing. *Nat. Methods* **9**, 721–723 (2012).
- 525 13. Cox, S. *et al.* Bayesian localization microscopy reveals nanoscale podosome
526 dynamics. *Nat Methods* **9**, 195–200 (2012).
- 527 14. Ram, S., Ward, E. S. & Ober, R. J. Beyond Rayleigh’s criterion: A resolution
528 measure with application to single-molecule microscopy. *Proc. Natl. Acad. Sci.*
529 **103**, 4457–4462 (2006).
- 530 15. Deschout, H. *et al.* Precisely and accurately localizing single emitters in
531 fluorescence microscopy. *Nat. Methods* **11**, 253–266 (2014).
- 532 16. LeCun, Y., Bengio, Y. & Hinton, G. Deep learning. *Nature* **521**, 436–444 (2015).
- 533 17. Michael, E. *Sparse and Redundant Representations: From Theory to*
534 *Applications in Signal and Image Processing*. Springer (Springer Verlag, 2010).
- 535 18. Hinton, G. E. & Salakhutdinov, R. R. Reducing the Dimensionality of Data with
536 Neural Networks. *Science (80-.)*. **313**, (2006).
- 537 19. Schmidhuber, J. Deep learning in neural networks: An overview. *Neural*
538 *Networks* **61**, 85–117 (2014).
- 539 20. Sage, D. *et al.* Quantitative evaluation of software packages for single-molecule
540 localization microscopy. *Nat. Methods* **12**, 717–724 (2015).

- 541 21. Isola, P., Zhu, J.-Y., Zhou, T. & Efros, A. A. Image-to-Image Translation with
542 Conditional Adversarial Networks. <http://arxiv.org/abs/1611.07004> (2016).
- 543 22. Ronneberger, O., Fischer, P. & Brox, T. U-net: Convolutional networks for
544 biomedical image segmentation. in *Medical Image Computing and Computer-*
545 *Assisted Intervention – MICCAI 2015. Lecture Notes in Computer Science*, **9351**,
546 234–241 (Springer International Publishing, 2015).
- 547 23. Goodfellow, I. *et al.* Generative Adversarial Nets. *Adv. Neural Inf. Process. Syst.*
548 *27* 2672–2680 (2014). doi:10.1017/CBO9781139058452
- 549 24. Ciresan, D., Giusti Alessandro, Luca, G. & Schmidhuber, J. Mitosis Detection in
550 Breast Cancer Histology Images with Deep Neural Networks. *Med. Image*
551 *Comput. Comput. Interv. – MICCAI 2013* **8150**, (2013).
- 552 25. Wang, Z. W. Z. & Bovik, A. C. A. C. Mean squared error: Love it or leave it? A
553 new look at Signal Fidelity Measures. *IEEE Signal Process. Mag.* **26**, 98–117
554 (2009).
- 555 26. Zhao, H., Gallo, O., Frosio, I. & Kautz, J. Loss Functions for Image Restoration
556 with Neural Networks. *IEEE Trans. Comput. IMAGING* **3**, 47–57 (2017).
- 557 27. Culley, S. *et al.* NanoJ-SQUIRREL: quantitative mapping and minimisation of
558 super-resolution optical imaging artefacts. *bioRxiv* 158279 (2017).
559 doi:10.1101/158279
- 560 28. Srivastava, N., Hinton, G., Krizhevsky, A., Sutskever, I. & Salakhutdinov, R.
561 Dropout: A Simple Way to Prevent Neural Networks from Overfitting. *J. Mach.*
562 *Learn. Res.* **15**, (2014).
- 563 29. Arbona, J.-M., Herbert, S., Fabre, E. & Zimmer, C. Inferring the physical
564 properties of yeast chromatin through Bayesian analysis of whole nucleus
565 simulations. *Genome Biol.* **18**, 81 (2017).
- 566 30. Arnal, I. & Wade, R. H. How does taxol stabilize microtubules? *Curr. Biol.* **5**,
567 900–908 (1995).
- 568 31. Wu, S. *et al.* Microtubule motors regulate ISOC activation necessary to
569 increase endothelial cell permeability. *J. Biol. Chem.* **282**, 34801–8 (2007).
- 570 32. De Brabander, M., De May, J., Joniau, M. & Geuens, G. Ultrastructural
571 immunocytochemical distribution of tubulin in cultured cells treated with
572 microtubule inhibitors. *Cell Biol. Int. Rep.* **1**, 177–83 (1977).
- 573 33. Schnitzbauer, J., Strauss, M. T., Schlichthaerle, T., Schueder, F. & Jungmann, R.
574 Super-resolution microscopy with DNA-PAINT. *Nat. Protoc.* **12**, 1198–1228
575 (2017).
- 576 34. Löscherger, A. *et al.* Super-resolution imaging visualizes the eightfold
577 symmetry of gp210 proteins around the nuclear pore complex and resolves
578 the central channel with nanometer resolution. *J. Cell Sci.* **125**, 570–5 (2012).
- 579 35. Szymborska, A. *et al.* Nuclear pore scaffold structure analyzed by super-
580 resolution microscopy and particle averaging. *Science* **341**, 655–8 (2013).
- 581 36. Sellés, J. *et al.* Nuclear pore complex plasticity during developmental process
582 as revealed by super-resolution microscopy. *Sci. Rep.* **7**, 14732 (2017).
- 583 37. Bellot, G. *et al.* TOM22, a core component of the mitochondria outer
584 membrane protein translocation pore, is a mitochondrial receptor for the
585 proapoptotic protein Bax. *Cell Death Differ.* **14**, 785–794 (2007).
- 586 38. Boettiger, A. N. *et al.* Super-resolution imaging reveals distinct chromatin

- 587 folding for different epigenetic states. *Nature* **529**, 418–422 (2016).
- 588 39. Zhang, Z., Nishimura, Y. & Kanchanawong, P. Extracting microtubule networks
589 from superresolution single-molecule localization microscopy data. *Mol. Biol.*
590 *Cell* **28**, 333–345 (2017).
- 591 40. Neumann, B. *et al.* Phenotypic profiling of the human genome by time-lapse
592 microscopy reveals cell division genes. *Nature* **464**, 721–727 (2010).
- 593 41. Beghin, A. *et al.* Localization-based super-resolution imaging meets high-
594 content screening. *Nat. Methods* **14**, 1184–1190 (2017).
- 595 42. Ouyang, W. & Zimmer, C. The imaging tsunami: Computational opportunities
596 and challenges. *Curr. Opin. Syst. Biol.* **4**, 105–113 (2017).
- 597 43. Chen, F., Tillberg, P. W. & Boyden, E. S. Expansion microscopy. *Science (80-.)*.
598 **347**, 543–548 (2015).
- 599 44. Chang, J.-B. *et al.* Iterative expansion microscopy. *Nat. Methods* (2017).
600 doi:10.1038/nmeth.4261
- 601 45. de Boer, P., Hoogenboom, J. P. & Giepmans, B. N. G. Correlated light and
602 electron microscopy: ultrastructure lights up! *Nat. Methods* **12**, 503–513
603 (2015).
- 604 46. Huang, B., Wang, W., Bates, M. & Zhuang, X. Three-dimensional super-
605 resolution imaging by stochastic optical reconstruction microscopy. *Science*
606 *(80-.)*. **319**, 810–813 (2008).
- 607 47. Bates, M., Huang, B., Dempsey, G. T. & Zhuang, X. Multicolor Super-Resolution
608 Imaging with Photo-Switchable Fluorescent Probes. *Science (80-.)*.
609 1146598v1 (2007).
- 610 48. Jungmann, R. *et al.* Multiplexed 3D cellular super-resolution imaging with
611 DNA-PAINT and Exchange-PAINT. *Nat. Methods* **11**, 313–318 (2014).
- 612 49. Shroff, H., Galbraith, C. G., Galbraith, J. A. & Betzig, E. Live-cell photoactivated
613 localization microscopy of nanoscale adhesion dynamics. *Nat Methods* **5**, 417–
614 423 (2008).
- 615 50. Kendall, A. & Gal, Y. What Uncertainties Do We Need in Bayesian Deep
616 Learning for Computer Vision? *Adv. Neural Inf. Process. Syst. 30 (NIPS 2017)*
617 *pre-proceedings* 5580–5590 (2017).
618

619 **FIGURE LEGENDS**

620

621 **FIGURE 1: Overview of ANNA-PALM**

622 ANNA-PALM consists of two main stages: **(a)** acquisition of training images using
623 standard localization microscopy (PALM) followed by artificial neural network
624 (ANN) training, and **(b)** reconstruction of super-resolution views and low resolution
625 error maps from new sparse PALM and/or widefield images (inference).

626 **(a)** Training images are obtained by acquiring one or a few long sequences, of
627 $K \sim 10^3 - 10^5$ diffraction limited, single molecule image frames, as in standard PALM
628 experiments; optionally, a widefield image W can also be acquired (top). The
629 acquisition time for each image sequence is $K\Delta t$, where Δt is the single frame
630 exposure time. Standard localization microscopy algorithms (grey 'localization'
631 boxes) are used to generate super-resolution images. For each experiment, a highly
632 sampled (dense) super-resolution image (PK) is generated using all (or in practice
633 $\geq 95\%$) available K frames. Sparse PALM images (P_k) from the same experiment are
634 obtained by using only $k \ll K$ frames. A switch (light blue) can be set to distinguish
635 different types of structures, e.g. nuclear pore complexes ('NPC'), mitochondria
636 ('Mito') or microtubules ('MT'). An ANN (labeled \mathcal{G} for 'generator', orange) is trained
637 by using the sparse PALM images P_k (plus an upsampled version L of the widefield
638 image W and the switch setting) as inputs and the corresponding dense PALM image
639 PK as target output. During training, the output of the generator \mathcal{G} (A_k) is compared
640 to the target image PK and the widefield image L (if available) via three loss, or error
641 functions (gray bordered boxes): (i) the 'super-resolution reconstruction error'

642 measures the difference between the reconstructed image A_k and the target PK
643 using a combination of the L1 norm and the MS-SSIM; (ii) the ‘low resolution
644 reconstruction error’ measures the MS-SSIM between the low resolution image WA
645 predicted from the reconstruction A_k and the low resolution image WP predicted
646 from the target image PK . Images WA and WP are predicted using a second ANN,
647 called low-resolution estimator (labeled Q , blue) that is trained to produce an
648 approximation of the actual widefield image W based on the MS-SSIM metric; (iii)
649 the ‘conditional GAN error’ uses a third ANN (labeled D for ‘discriminator’, red) that
650 attempts to distinguish between real dense PALM images PK and the generator’s
651 output A_k . The combined loss functions are iteratively optimized using stochastic
652 gradient descent. **(b)** A short sequence of diffraction limited single molecule images
653 (with $k \ll K$ frames, i.e. acquisition time $k\Delta t$), and an optional widefield image (W'),
654 are acquired. Standard localization algorithms generate a sparse (under-sampled)
655 PALM image ($P'k$). This sparse image $P'k$ (and the upscaled widefield image L' and
656 switch setting) are fed as inputs to the trained generator \mathcal{G} , which outputs a
657 reconstructed ANNA-PALM image ($A'k$). In addition, the low resolution estimator Q
658 predicts a low resolution image WA' , which can be compared to the input widefield
659 image W' via the MS-SSIM to produce a low resolution error map (top).

660

661 **FIGURE 2: Validation of ANNA-PALM on simulated images**

662 **(a)** Simulated widefield image of microtubules. **(b)** Simulated sparse PALM image of
663 microtubules with $n= 6,834$ localizations. **(c)** ANNA-PALM reconstruction using only
664 the widefield image **a** as input. **(d)** ANNA-PALM reconstruction using both the

665 widefield image **a** and the sparse PALM **b** image as inputs. **(e)** Simulated “perfect”
666 PALM image, equivalent to a PALM image with an infinite number of localizations
667 ($n=\infty$) and a resolution of 23 nm. This image was used to generate **a** (by convolution
668 with a Gaussian kernel approximating the microscope point spread function) and **b**
669 (by application of Poisson noise). **(f)** Merged image showing the perfect PALM image
670 **e** in green and the ANNA-PALM reconstruction **d** in red. Note that the ANNA-PALM
671 images **c,d** provide many high resolution details that are absent from the widefield
672 image **a** and the sparse PALM image **b** and that are in good (**c**) or very good (**d**)
673 agreement with the perfect PALM image **e**. Some reconstruction errors are
674 highlighted by arrows. Blue arrows in panel **c** point to errors of ANNA-PALM
675 reconstruction from the widefield image only, the white arrow in panel **d** points to
676 an error of ANNA-PALM reconstruction from both widefield and sparse PALM
677 images combined. Reconstruction errors diminish for larger numbers of
678 localizations, n (**Supplementary Figure 4**). **(g)** Reconstruction quality of PALM and
679 ANNA-PALM images, measured by the MS-SSIM with the perfect PALM image **e**, as
680 function of localization number n . Black curve: reconstruction quality of the
681 standard PALM images. Dashed blue curve: reconstruction quality of ANNA-PALM
682 using the sparse PALM images as input. Solid blue curve: reconstruction quality of
683 ANNA-PALM using both the sparse PALM and widefield images as inputs. Red
684 dashed line: reconstruction quality of ANNA-PALM using the widefield images as
685 input only. Dots are averages from 10 simulations; error bars show standard
686 deviations. The vertical dashed orange line indicates the minimum number of
687 localizations needed to achieve a resolution of $R_{5 \times Nyq} = 23$ nm according to the five-

688 fold Nyquist criterion³. The dashed grey line indicates the minimum number of
689 localizations needed to achieve a double mean nearest neighbor distance less than
690 23 nm. ANNA-PALM reconstructions from sparse PALM images only (i.e. without
691 widefield images) achieve the same average MS-SSIM as standard PALM at the five-
692 fold Nyquist sampling limit with 26 times less localizations (blue double arrow).
693 ANNA-PALM reconstruction quality is highest when using both widefield and sparse
694 PALM images as inputs.

695

696 **FIGURE 3: ANNA-PALM imaging of microtubules**

697 ANNA-PALM reconstructions of a localization microscopy image of immunostained
698 microtubules. **(a)** Widefield image. **(b)** Sparse PALM image obtained from the first
699 9 s of acquisition ($k=300$ frames, $n=11,740$ localizations). **(c)** Dense PALM image
700 obtained from a 15 min long acquisition ($K=30,000$ frames, $N=409,364$
701 localizations). **(d)** ANNA-PALM reconstruction from the widefield image **a** only.
702 **(e)** ANNA-PALM reconstruction from the sparse PALM image **b** only. **(f)** ANNA-
703 PALM reconstruction from the widefield image **a** and sparse PLAM image **b**
704 combined. In panels **b-f**, pixel values are linearly mapped to colors from the look-up
705 table shown below. Black and white correspond to values V_{\min} and V_{\max} ,
706 respectively, with $V_{\min}=0$ for all panels, $V_{\max}=3, 24, 102, 102$ and 102 for panels **b, c,**
707 **d, e** and **f**, respectively. **(g-i)** Merged images comparing ANNA-PALM
708 reconstructions from panels **d-f** to the dense PALM image **c**. ANNA-PALM
709 reconstructions are shown in red, the dense PALM image in green. **(j)** Gradual
710 improvement of image quality for increasing acquisition time $k\Delta t$, shown for the

711 area highlighted in the insets of panels **a-i**. Top row: sparse PALM images. Middle
712 row: ANNA-PALM reconstructions from the sparse PALM images only (without
713 widefield). Bottom row: ANNA-PALM reconstructions from the widefield and sparse
714 PALM images combined. **Supplementary Video 1** shows the gradual increase in
715 quality of PALM and ANNA-PALM images with increased acquisition time for the
716 larger region of interest shown in panels **a-i**.

717

718 **FIGURE 4: High-throughput imaging with ANNA-PALM**

719 Application of ANNA-PALM to high-throughput imaging of a 1.8 mm x 1.8 mm area
720 containing more than 1,000 cells. **(a)** Sparse PALM image of this area, constructed
721 by assembling a mosaic of $33 \times 33 = 1,089$ sparse PALM images of individual fields of
722 view, obtained from $k=1,000$ raw frames each (with $\Delta t=10$ ms exposure time per
723 frame, i.e. in $k\Delta t=10$ s). Total image acquisition time was $1,089 \times 10$ s, i.e. ~ 3.1 hours.
724 The sparsity of the image is not apparent at this large scale. **(b)** ANNA-PALM
725 reconstruction of the image in **a**, obtained by assembling a mosaic of 1,089
726 individual reconstructions (one per field of view). **(c)** Magnified view of the green
727 boxed region in **a**. The inset shows a further magnified view of the yellow boxed
728 region, highlighting the sparsity of the image. **(d)** Same as **c**, but for the ANNA-PALM
729 reconstruction. A line profile across a microtubule is shown, with a $\text{FWHM} \approx 51$ nm.
730 Non-linear contrast adjustment was applied manually for panels **a** and **b**, with black
731 corresponding to values of zero in both panels. In panels **c** and **d**, pixel values were
732 linearly mapped to colors from the look-up table in **Figure 3**; Black and white
733 correspond to values V_{\min} and V_{\max} , respectively, with $V_{\min}=0$ for all panels, and

734 $V_{\max}=3$ and 51 for panels **c** and **d**, respectively. See also **Supplementary Video 2** for
735 an animated 'zoom-in' highlighting the spatial scales covered by the assembled
736 image. See also **Supplementary Figure 12** for ANNA-PALM reconstructions of the
737 same area from the widefield images only.

738

739 **FIGURE 5: Robustness of ANNA-PALM to experimental perturbations**

740 This figure shows ANNA-PALM reconstructions using an ANN trained on PALM
741 images of microtubules in untreated cells and applied without retraining to sparse
742 localization images of microtubules in different experimental conditions: untreated
743 control cells (**a-c**); cells treated with 1 μM of Taxol (**d-f**); cells treated with 1 μM of
744 Nocodazole (**g-i**); untreated cells imaged with DNA-PAINT (**j-l**). (**a,d,g,j**) Sparse
745 localization images obtained from the first k frames of the acquired image sequence,
746 with $k=500, 800, 300,$ and 400 for **a, d, g,** and **j**, respectively. (**b,e,h,k**) ANNA-PALM
747 reconstructions using the sparse localization images immediately to the left as
748 input. (**c,f,i,l**) Dense localization images obtained from $K=60,000$ frames. Pixel
749 values are linearly mapped to colors from the look-up table in **Figure 3**. Black and
750 white correspond to values V_{\min} and V_{\max} , respectively, with $V_{\min}=0$ for all panels,
751 and $V_{\max}=10, 120, 90, 25, 150, 40, 18, 150, 50, 18, 120,$ and 200 for panels **a, b, c, d,**
752 **e, f, g, h, i, j, k,** and **l**, respectively.

753

754 **FIGURE 6: ANNA-PALM reconstructions of nuclear pores and mitochondria**

755 PALM and ANNA-PALM images of nuclear pores (**a-c**) and mitochondria (**d-f**).
756 (**a**) Sparse PALM image of the immunolabeled *Xenopus* nucleoporin gp210 obtained

757 from the first $k=3,000$ frames. Note that individual nuclear pores are hard to
758 identify. **(b)** ANNA-PALM reconstruction of image **a**. **(c)** Dense PALM image obtained
759 from all $K=30,000$ frames. **(d)** Sparse PALM image of the immunolabeled
760 mitochondrial outer membrane protein TOM22, obtained from the first $k=400$
761 frames. **(e)** ANNA-PALM reconstruction of image **d**. **(f)** Dense PALM image obtained
762 from all $K=30,000$ frames. Pixel values are linearly mapped to colors from the look-
763 up table shown in **Figure 3**. Black and white correspond to values V_{\min} and V_{\max} ,
764 respectively, with $V_{\min}=0$ for all panels, and $V_{\max}=3, 51, 3, 3, 128,$ and 18 for panels **a**,
765 **b, c, d, e,** and **f**, respectively

766 **ONLINE METHODS**

767

768 **Artificial neural network**

769 Our ANN, called ‘A-net’, is based on the pix2pix architecture²¹, which is a special
770 conditional generative adversarial network (cGAN)²³ for image to image
771 “translation”, i.e. mapping from one type of image to another. The A-net consists of
772 three distinct neural networks: (i) a generator network \mathcal{G} that produces the
773 reconstructed super-resolution image, (ii) a network Q called ‘low resolution
774 estimator’ that produces the low resolution error map, (iii) a cGAN discriminator
775 network D that provides the adversarial loss (**Figure 1a**). The generator network \mathcal{G}
776 builds on the U-net architecture, and consists of an encoder-decoder network with
777 skip connections²² and 16 convolutional layers. Its inputs and outputs are image
778 patches containing $(256m) \times (256m)$ pixels, where m is an integer (we used $m=1$ or 2
779 but this can be adjusted for different sizes of CPU/GPU memory or input images).
780 The input is a sparse PALM image, a widefield image upscaled to the same size (see
781 below), and a computational switch number that allows the network to switch
782 between different types of image structures (e.g. nuclear pores or microtubules).
783 The switch setting is encoded numerically and coupled by convolutional operations
784 into the A-net encoder. The output of the generator \mathcal{G} is a reconstructed image
785 (called ANNA-PALM reconstruction or ANNA-PALM image elsewhere) of the same
786 size as the input images. The low resolution estimator Q has four convolutional
787 layers. It takes the $(256m) \times (256m)$ dense PALM image patch or the ANNA-PALM
788 image patch as input and outputs a low resolution image with $(64m) \times (64m)$ pixels.

789 The cGAN discriminator network D has five convolutional layers. Its inputs are three
790 $(256m) \times (256m)$ pixel image patches (the sparse PALM image, the widefield image,
791 and either the ANNA-PALM reconstruction or the corresponding dense PALM
792 image), plus the upscaled widefield image, and its output is a $(30m) \times (30m)$ image
793 whose pixel values indicate whether the corresponding input patch is real (i.e. an
794 experimentally obtained conventional PALM image) or produced by the generator \mathcal{G} .
795 All convolutional layers are followed by batch normalization⁵¹. Dropout layers²⁸
796 (with dropout probability $p=0.5$) are introduced in the central layers of the A-net
797 generator and turned on during training, but switched off during inference.
798 Activation functions are rectified linear units (ReLU) $x \rightarrow \sup(x, 0)$ or “leaky” ReLUs
799 $x \rightarrow \sup(x, 0) + \inf(\epsilon x, 0)$ with $\epsilon = 0.2$ ⁵², except for the last layer of \mathcal{G} , which uses the
800 hyperbolic tangent $x \rightarrow \tanh(x)$ and the last layer of Q , which uses a sigmoid
801 function $x \rightarrow (1 + \exp(-x))^{-1}$. The A-net architecture is fully described in
802 **Supplementary Note 1 and Supplementary Tables 1-4.**

803

804 **Training objectives and error map**

805 Each of the three networks mentioned above (\mathcal{G} , Q , and D) is associated to a distinct
806 objective function - also called loss- and hereafter noted $\mathcal{L}_{\mathcal{G}}$, \mathcal{L}_Q , and \mathcal{L}_D respectively.
807 These loss functions are specified in detail below. In the following equations, for
808 notational simplicity, we designate the sparse input image as \mathbf{S} , the low resolution
809 (widefield) input image as \mathbf{W} , the corresponding dense PALM image (i.e. the target)
810 as \mathbf{T} , and the A-net’s output as $\mathbf{A} = \mathcal{G}(\mathbf{S}, \mathbf{W})$ (in **Figure 1a**, images \mathbf{S} , \mathbf{T} and \mathbf{A} are
811 labeled Pk, PK and Ak, respectively); the computational switch indicating the image

812 type is noted \mathbf{M} . Low resolution images produced by the low resolution estimator
 813 network Q from \mathbf{A} and \mathbf{T} are designated as $\mathbf{W}_A = Q(\mathbf{A})$ and $\mathbf{W}_T = Q(\mathbf{T})$,
 814 respectively.

815 The generator loss function \mathcal{L}_G is the sum of three terms. The first term of \mathcal{L}_G
 816 is the super-resolution reconstruction error, hereafter called $\mathcal{L}_{\text{SuperRes}}(\mathcal{G})$. This term
 817 penalizes the difference between the generator output \mathbf{A} and the target image \mathbf{T} .
 818 Based on a recent analysis of loss functions for image restoration with neural
 819 networks²⁶, we defined this difference as a weighted average of two quantities:
 820 (i) the multi-scale structural similarity index (MS-SSIM) between \mathbf{A} and \mathbf{T} and (ii) a
 821 modification of the L1 norm, where the absolute difference between \mathbf{A} and \mathbf{T} is
 822 smoothed by a Gaussian kernel:

$$\begin{aligned} \mathcal{L}_{\text{SuperRes}}(\mathcal{G}) &= \mathbb{E}_{(\mathbf{S}, \mathbf{T}, \mathbf{W}, \mathbf{M}) \sim p_{\text{data}}(\mathbf{S}, \mathbf{T}, \mathbf{W}, \mathbf{M})} [\rho (1 - MS_SSIM(\mathbf{A}, \mathbf{T})) + (1 \\ &\quad - \rho) \langle G_\sigma * |\mathbf{A} - \mathbf{T}| \rangle] \\ &= \mathbb{E}_{(\mathbf{S}, \mathbf{T}, \mathbf{W}, \mathbf{M}) \sim p_{\text{data}}(\mathbf{S}, \mathbf{T}, \mathbf{W}, \mathbf{M})} [\rho (1 - MS_SSIM(\mathcal{G}(\mathbf{S}, \mathbf{W}, \mathbf{M}), \mathbf{T})) + (1 \\ &\quad - \rho) \langle G_\sigma * |\mathcal{G}(\mathbf{S}, \mathbf{W}, \mathbf{M}) - \mathbf{T}| \rangle] \end{aligned}$$

823 where \mathbb{E} denotes expectation; $p_{\text{data}}(\mathbf{S}, \mathbf{T}, \mathbf{W}, \mathbf{M})$ is the joint probability density of the
 824 sparse PALM images \mathbf{S} , dense PALM images \mathbf{T} , widefield images \mathbf{W} and switch
 825 settings \mathbf{M} from the training data set; $MS_SSIM(\mathbf{A}, \mathbf{T})$ is the multi-scale structural
 826 similarity index between \mathbf{A} and \mathbf{T} ; G_σ is a Gaussian smoothing kernel; $*$ denotes
 827 convolution; $|\mathbf{A} - \mathbf{T}|$ is the absolute difference image (i.e. pixel (i,j) has value
 828 $|\mathbf{A}(i, j) - \mathbf{T}(i, j)|$ and $\rho \in [0, 1]$ is a scalar weight that balances the relative
 829 contributions of MS-SSIM and the modified L1 norm and is set to $\rho = 0.84$ as in ref.
 830 ²⁶.

831 The second term of $\mathcal{L}_{\mathcal{G}}$ is called $\mathcal{L}_{\text{LowRes}}(\mathcal{G}, Q)$ and measures the consistency
 832 between the low resolution images \mathbf{W}_A and \mathbf{W}_T predicted by the low resolution
 833 estimator network Q :

$$\begin{aligned}\mathcal{L}_{\text{LowRes}}(\mathcal{G}, Q) &= \mathbb{E}_{(\mathbf{S}, \mathbf{T}, \mathbf{W}, \mathbf{M}) \sim p_{\text{data}}(\mathbf{S}, \mathbf{T}, \mathbf{W}, \mathbf{M})} [1 - MS_SSIM(\mathbf{W}_A, \mathbf{W}_T)] \\ &= \mathbb{E}_{(\mathbf{S}, \mathbf{T}, \mathbf{W}, \mathbf{M}) \sim p_{\text{data}}(\mathbf{S}, \mathbf{T}, \mathbf{W}, \mathbf{M})} [1 - MS_SSIM(Q(\mathcal{G}(\mathbf{S}, \mathbf{W}, \mathbf{M})), Q(\mathbf{T}))]\end{aligned}$$

834 Alternatively, in the above objective function, \mathbf{W}_T can be replaced by the actually
 835 observed widefield image \mathbf{W} , although with our data this led to slightly lower
 836 reconstruction quality. The low resolution estimator network Q is trained
 837 simultaneously with the generator \mathcal{G} to produce a low resolution image from the
 838 dense PALM image \mathbf{T} that is consistent with the observed low resolution image \mathbf{W} .
 839 This training is done based on the following objective function:

$$\mathcal{L}_Q(Q) = \mathbb{E}_{(\mathbf{T}, \mathbf{W}) \sim p_{\text{data}}(\mathbf{T}, \mathbf{W})} [1 - MS_SSIM(Q(\mathbf{T}), \mathbf{W})]$$

840 Note that the reconstructed low resolution image $Q(\mathbf{T})$ is four times smaller than
 841 the dense PALM image \mathbf{T} , as described in **Supplementary Note 1**. Because the input
 842 widefield image \mathbf{W} can have a different size, we use bilinear interpolation to resize
 843 \mathbf{W} to the same size as $Q(\mathbf{T})$. (If needed, a scaling factor different from four can be
 844 obtained by adding or removing downsample layers in network Q). At inference, the
 845 low resolution estimator Q is also used to produce the error map, as shown in
 846 **Figure 1b**, and **Supplementary Figures 6, 11, 15**. This error map is defined as:

$$E_Q(\mathbf{A}, \mathbf{W}) = (1 - MS_SSIM(Q(\mathbf{A}), \mathbf{W}))(Q(\mathbf{A}) + \mathbf{W})$$

847 High (respectively low) values of the error map indicate large (respectively small)
 848 inconsistencies, between the reconstructed super-resolution image \mathbf{A} and the
 849 observed widefield image \mathbf{W} .

850 The third term of $\mathcal{L}_{\mathcal{G}}$ draws from recent work on generative adversarial
851 networks (GAN)^{21,23,53} and is noted $\mathcal{L}_{\text{cGAN}}(\mathcal{G}, \mathcal{D})$. In a GAN, a generator network \mathcal{G}
852 learns to transform random input vectors \mathbf{z} (drawn from a probability density
853 $p_{\mathbf{z}}(\mathbf{z})$) into new samples of a data probability density $p_{\text{data}}(\mathbf{x})$. In our case, the data
854 samples \mathbf{x} are the dense PALM images \mathbf{T} . The generator \mathcal{G} learns by working against
855 a discriminator network \mathcal{D} that simultaneously learns to discriminate between
856 original data samples and samples generated by \mathcal{G} . Adversarial training thus
857 consists in playing a minmax game such that $(\mathcal{G}^*, \mathcal{D}^*) = \arg \min_{\mathcal{G}} \max_{\mathcal{D}} \mathcal{L}_{\text{GAN}}(\mathcal{G}, \mathcal{D})$,
858 with an objective function of the form²³: $\mathcal{L}_{\text{GAN}}(\mathcal{G}, \mathcal{D}) = \mathbb{E}_{\mathbf{x} \sim p_{\text{data}}(\mathbf{x})} [\log \mathcal{D}(\mathbf{x})] +$
859 $\mathbb{E}_{\mathbf{z} \sim p_{\mathbf{z}}(\mathbf{z})} \log[1 - \mathcal{D}(\mathcal{G}(\mathbf{z}))]$, or equivalently by simultaneous optimization of two
860 coupled loss functions:

$$\begin{cases} \mathcal{D}^* = \arg \max_{\mathcal{D}} (\mathbb{E}_{\mathbf{x} \sim p_{\text{data}}(\mathbf{x})} [\log \mathcal{D}(\mathbf{x})] + \mathbb{E}_{\mathbf{z} \sim p_{\mathbf{z}}(\mathbf{z})} \log[1 - \mathcal{D}(\mathcal{G}(\mathbf{z}))]) \\ \mathcal{G}^* = \arg \min_{\mathcal{G}} (\mathbb{E}_{\mathbf{z} \sim p_{\mathbf{z}}(\mathbf{z})} \log[1 - \mathcal{D}(\mathcal{G}(\mathbf{z}))]) \end{cases}$$

861 In a conditional GAN (cGAN), the generator and the discriminator have an extra
862 input vector \mathbf{c} and the first objective function above becomes: $\mathcal{L}_{\mathcal{D}}(\mathcal{G}, \mathcal{D}) =$
863 $\mathbb{E}_{(\mathbf{c}, \mathbf{x}) \sim p_{\text{data}}(\mathbf{c}, \mathbf{x})} [\log \mathcal{D}(\mathbf{c}, \mathbf{x})] + \mathbb{E}_{\mathbf{c} \sim p_{\text{data}}(\mathbf{c}), \mathbf{z} \sim p_{\mathbf{z}}(\mathbf{z})} \log[1 - \mathcal{D}(\mathbf{c}, \mathcal{G}(\mathbf{c}, \mathbf{z}))]$, such that the
864 generator learns a conditional probability density $p_{\text{data}}(\mathbf{x}|\mathbf{c})$; and the second
865 objective function likewise becomes $\mathcal{L}_{\text{cGAN}}(\mathcal{G}, \mathcal{D}) = \mathbb{E}_{\mathbf{c} \sim p_{\text{data}}(\mathbf{c}), \mathbf{z} \sim p_{\mathbf{z}}(\mathbf{z})} \log[1 -$
866 $\mathcal{D}(\mathcal{G}(\mathbf{z}))]$. In our A-net, we replaced the logarithmic losses above by least square
867 losses⁵³, as they empirically yielded better results. Thus, we used the objective
868 functions:

869 $\mathcal{L}_{\mathcal{D}}(\mathcal{G}, \mathcal{D}) = \mathbb{E}_{(\mathbf{c}, \mathbf{x}) \sim p_{\text{data}}(\mathbf{c}, \mathbf{x})} (\mathcal{D}(\mathbf{c}, \mathbf{x}) - 1)^2 + \mathbb{E}_{\mathbf{c} \sim p_{\text{data}}(\mathbf{c}), \mathbf{z} \sim p_{\mathbf{z}}(\mathbf{z})} [\mathcal{D}(\mathbf{c}, \mathcal{G}(\mathbf{c}, \mathbf{z}))]^2$ and

870 $\mathcal{L}_{\text{cGAN}}(\mathcal{G}, \mathcal{D}) = \mathbb{E}_{\mathbf{c} \sim p_{\text{data}}(\mathbf{c}), \mathbf{z} \sim p_{\mathbf{z}}(\mathbf{z})} [1 - \mathcal{D}(\mathbf{c}, \mathcal{G}(\mathbf{c}, \mathbf{z}))]^2$. In our case, the input \mathbf{c} is the
871 sparse PALM image \mathbf{S} combined with the upsampled version $\mathbf{L} = \mathcal{B}(\mathbf{W})$ of the
872 widefield image \mathbf{W} , where \mathcal{B} denotes bilinear interpolation. Note that in practice the
873 noise \mathbf{z} in our ANN was introduced only through the use of dropout layers, as in the
874 pix2pix implementation²¹. Thus, the objective functions are:

$$\begin{aligned} \mathcal{L}_{\mathcal{D}}(\mathcal{D}) = & \mathbb{E}_{\mathbf{S}, \mathbf{T}, \mathbf{W}, \mathbf{M} \sim p_{\text{data}}(\mathbf{S}, \mathbf{T}, \mathbf{W}, \mathbf{M})} (\mathcal{D}(\mathcal{B}(\mathbf{W}), \mathbf{S}, \mathbf{T}) - 1)^2 \\ & + \mathbb{E}_{\mathbf{z} \sim p_{\mathbf{z}}(\mathbf{z}), \mathbf{S} \sim p_{\text{data}}(\mathbf{S})} (\mathcal{D}(\mathcal{B}(\mathbf{W}), \mathbf{S}, \mathcal{G}(\mathbf{S}, \mathbf{W}, \mathbf{M})))^2 \end{aligned}$$

875 and:

$$\mathcal{L}_{\text{cGAN}}(\mathcal{G}, \mathcal{D}) = \mathbb{E}_{(\mathbf{S}, \mathbf{T}, \mathbf{W}, \mathbf{M}) \sim p_{\text{data}}(\mathbf{S}, \mathbf{T}, \mathbf{W}, \mathbf{M})} (\mathcal{D}(\mathcal{B}(\mathbf{W}), \mathbf{S}, \mathcal{G}(\mathbf{S}, \mathbf{W}, \mathbf{M})) - 1)^2$$

876 In the end, combining the three loss terms described above, we implemented
877 the following optimization problem :

$$\begin{cases} Q^* = \arg \min_Q \mathcal{L}_Q(Q) \\ D^* = \arg \max_D \mathcal{L}_D(D) \\ G^* = \arg \min_G [\alpha \mathcal{L}_{\text{SuperRes}}(G) + \beta \mathcal{L}_{\text{LowRes}}(G, Q) + \gamma \mathcal{L}_{\text{cGAN}}(G, D)] \end{cases}$$

878 The weights α , β and γ are hyperparameters, which we set manually to $\alpha = 50$,
879 $\beta = 25$ and $\gamma = 1$ for most experiments. In absence of widefield images \mathbf{W} , β was
880 simply set to zero. The reported results are not very sensitive to these parameters.

881 We trained the A-net end-to-end using stochastic gradient descent (SGD)
882 with Adam⁵⁴ and a batch size of 1 with 200,000 or more iterations (backpropagation
883 steps). Our implementation was adapted from `affinelay`'s TensorFlow⁵⁵
884 implementation, which is ported from the Torch implementation of pix2pix²¹. Both
885 network training and inference were performed on Tesla P100, Tesla M40, Tesla

886 K80 or GTX TitanXP graphical processing units (GPUs) from Nvidia. A-net training
887 from scratch typically takes from hours to days on a single GPU. Once trained, the A-
888 net takes only ~ 1 second or less to reconstruct a super-resolution image of
889 2560x2560 pixels (corresponding to an entire FoV). Training time could be further
890 reduced by pretraining (or transfer learning), use of GPU clusters, or optimized data
891 augmentation.

892

893 **Experimental training images and data augmentation**

894 Experimental training data are obtained from standard localization microscopy data
895 (dense PALM images). To achieve good performance, ANNs generally necessitate
896 large amounts of training data. However, ANNA-PALM typically requires PALM
897 images from no more than 10 FoVs (of $55 \mu\text{m} \times 55 \mu\text{m}$ each) and can even be trained
898 with a single FoV. This is possible thanks to an extensive on-the-fly data
899 augmentation strategy, as described below. Each of the dense PALM training images
900 corresponds to a list of localizations $(f_i, x_i, y_i)_{i=1..n}$, where $f_i \in [1, K]$ is the index of
901 the diffraction limited frame from which localization x_i, y_i originates, and K is the
902 total frame number. PALM images are obtained as plain 2D histograms of these
903 localizations with typical pixel sizes of 10-20 nm. From each list of localizations
904 (corresponding to a dense PALM image of a single FoV), we generate 10-30 pairs of
905 input and target images (S, T) for training. To define the target image T , we take a
906 random consecutive subset $[k_T, k_T + 0.95K]$ of 95% of all available K frames (k_T is
907 chosen randomly between 0 and $0.05K$) and create the 2D histogram image based
908 on localizations from those frames only, i.e. from all (x_j, y_j) such that $f_j \in$

909 $[k_T, k_T + 0.95K]$. To define the sparse input image \mathbf{S} , we take random subsets of
910 300-500 consecutive frames from the first half of the image sequence and similarly
911 create a 2D histogram of the localizations from those frames only. When a widefield
912 image \mathbf{W} is available, this image must first be aligned with the corresponding dense
913 PALM image \mathbf{T} . This is done using an FFT-based phase correlation algorithm⁵⁶ after
914 histogram equalization of image \mathbf{T} , smoothing by convolution with a Gaussian
915 Kernel of standard deviation 6 pixels, and resizing with bilinear interpolation to the
916 same size as image \mathbf{W} . The registered widefield image \mathbf{W} is then scaled up using
917 bilinear interpolation to an image $\mathbf{L} = \mathcal{B}(\mathbf{W})$ with the same size as image \mathbf{T} .

918 During training, for each iteration of SGD, we crop the images \mathbf{S} , \mathbf{L} and \mathbf{T} with
919 a randomly placed 712x712 pixel sized region $\mathcal{R} = [x_{\min}, x_{\min} + 712] \times$
920 $[y_{\min}, y_{\min} + 712]$. We then use random geometric transformations and apply them
921 identically to the three images. Specifically, we rotate the images by a random angle
922 between 0 and 360 degrees, apply elastic transformations⁵⁷, and then crop the
923 center region of size 512x512 pixels. In addition to geometric transformations, we
924 also introduce realistic noise from experimental background images. This is done by
925 manually outlining regions of background in selected PALM training images,
926 splitting these regions into small patches of 40x40 pixels, grouping them according
927 to their summed pixel values, then assembling them into a larger image with the
928 same size as \mathbf{T} . During training, these semi-synthetic noise images are randomly
929 selected and added to the input image \mathbf{S} without altering \mathbf{T} or \mathbf{W} . Finally, we
930 normalize the input image \mathbf{S} by subtracting its mean and dividing by standard
931 deviation. If a widefield image \mathbf{W} is provided, its pixel values are scaled to a

932 minimum of 0 and a maximum of 1. Otherwise, \mathbf{W} is replaced by an image containing
933 zeros only. The target image \mathbf{T} is truncated at a maximum value of 255 and then
934 scaled to have a minimum of 0 and a maximum of 1. For the switch \mathbf{M} , we used an
935 integer number to define the type of training images, e.g. 0 for microtubules, 1 for
936 nucleoporins, 2 for mitochondria. When training on different types of images, e.g.
937 microtubules and nucleoporins (**Supplementary Figure 13**), we assign the
938 corresponding switch value to \mathbf{M} and use it as additional input to the A-net together
939 with images \mathbf{S} and \mathbf{W} , as described in **Supplementary Note 1**.

940

941 **Image simulations**

942 Our procedure to simulate localization microscopy (PALM) images of microtubules
943 is illustrated in **Supplementary Figure 1**. To simulate microtubule filaments, we
944 used a Langevin dynamics simulation²⁹ that generates random configurations of
945 semiflexible curves with a specified rigidity (persistence length), starting from a
946 random initial configuration (**Supplementary Figure 1a,b**). The initial
947 configurations were generated with a Python library named cpolymer and the
948 Langevin dynamics was implemented using the molecular dynamics code
949 LAMMPS⁵⁸. Although the simulation generates 3D polymer chains, we only
950 considered their 2D projections, consisting of N_p connected positions $(x_k, y_k)_{k=1..N_p}$.
951 To obtain smooth filaments we further interpolated these connected segments using
952 spline functions with the Scipy function `scipy.interpolate.splev`. Next, we turned
953 these 2D curves into a grey scale image of 800x800 pixels, with an assumed pixel
954 size of 7.8 nm, using the Python library Matplotlib. This image was further

955 convolved with a Gaussian kernel of standard deviation 1.5 pixels, resulting in a
956 smooth image $I(i, j)$ as shown in **Supplementary Figure 1c**, and normalized to a
957 probability density ($\sum \sum_{i,j} I(i, j) = 1$, with all $I(i, j) \geq 0$). This image was used to
958 mimic a “perfect” PALM image of filaments corresponding to an infinite number of
959 localizations ($n = \infty$). Such perfect images were used as targets during ANN
960 training for simulated data and defined as ground truth for the quantification of
961 reconstruction quality by MS-SSIM (**Figure 2g**). During training, we applied the
962 same rotations and elastic transformations described for experimental data in the
963 previous section.

964 Localization microscopy images obtained from a finite number of
965 localizations $n < \infty$ (sparse PALM images \mathcal{S}), can be considered as a sampling of the
966 probability density $I(i, j)$ with n samples. These images can therefore be simulated
967 by applying Poisson noise to a rescaled version of the perfect PALM image, i.e.:
968 $\mathcal{S}(\lambda, I) = \mathcal{P}(\lambda I / I_{\max})$, where I_{\max} is the maximum value of I , $\mathcal{P}(\mu)$ denotes the
969 Poisson probability distribution of mean μ and where the peak parameter λ controls
970 the level of sampling. In order to simulate sparse PALM images for various levels of
971 sampling, we varied the peak value λ following a log-normal distribution where
972 $\ln(\lambda)$ has mean -0.5 and standard deviation 0.001 and applied Poisson noise using
973 the numpy library function `random.poisson`. An example of a simulated sparse
974 PALM image is shown in **Supplementary Figure 1d**. Besides finite sampling,
975 localization microscopy images are corrupted by additional noise sources such as
976 false detections from background noise due to out-of-focus light or unspecific
977 binding of antibodies. To mimic this, we first created a probability density

978 $I_b = I * G_{\sigma_b}$ for the background noise by convolving I with a Gaussian kernel G_{σ_b} of
979 large standard deviation $\sigma_b=25$ pixels, and applied Poisson noise with $\lambda = 0.06$. To
980 create training images, we added this background noise image to the sparse PALM
981 image S above (**Supplementary Figure 2**). We did not add background noise to the
982 test images used during inference (**Figure 2**). To simulate the widefield images
983 (**Figure 2a**), we first blurred the perfect PALM image by convolution with a
984 Gaussian kernel of standard deviation 8 pixels, then added Gaussian noise with zero
985 mean and standard deviation chosen randomly between 0.5 and 1.5.

986 For simulations of nuclear pore images (**Supplementary Figure 15**), we
987 applied a similar procedure, except that the perfect PALM images were obtained by
988 randomly distributing circles of diameter 150 nm in the plane (avoiding overlaps)
989 and placing eight Gaussian spots (of standard deviation 1.7 pixels) at equal distance
990 from each other on each circle to mimic the octogonal shape of nuclear pores.

991

992 **Sample preparation**

993 For microtubule imaging experiments (**Figures 3-5** and **Supplementary Figures 8-**
994 **10**), except those using DNA-PAINT (**Figure 5j,l**), U-373 MG (Uppsala) cells were
995 cultured in Dulbecco's Modified Eagle Medium: Nutrient Mixture F-12 (DMEM/F12;
996 Gibco) supplemented with 10% (v/v) fetal bovine serum (FBS; Gibco), 1% (v/v)
997 penicillin-streptomycin (Gibco), in a 5% CO₂ environment at 37°C on 18-mm
998 cleaned coverslips in 12-well plates. 24 hours after plating, cells were pre-extracted
999 for 10 s in 0.25% (v/v) Triton X-100 (Triton) in BRB80 (80 mM PIPES, 1 mM MgCl₂,
1000 1 mM EGTA, adjusted to pH 6.8 with KOH) supplemented with 4 mM EGTA, and

1001 immediately fixed for 10 min with 0.25% (v/v) Triton + 0.5% Glutaraldehyde in
1002 BRB80, followed by reduction for 7 min with 0.1% NaBH₄ solution in PBS and
1003 another washing step in PBS. Cells were directly incubated for 1h at room
1004 temperature in PBS with 1:500 rat alpha-tubulin antibodies (Bio-Rad MCA77G),
1005 followed by 3 washing steps with PBS, and then incubated for 45min in PBS with
1006 1:500 anti-rat Alexa-647 conjugated secondary antibodies from donkey (Jackson
1007 ImmunoResearch Laboratories, ref. 712-605-153).

1008 For the DNA-PAINT experiment on microtubules (**Figure 5k-m**), U-373 cells
1009 stuck on 18 mm diameter coverslips were fixed at 37°C with 4% PFA in PHEM
1010 buffer and permeabilized in 0.2% glutaldehyde. Next, cells were incubated for 1 h
1011 with 1:500 primary mouse antibodies against alpha-tubulin. The sample was
1012 washed 3 times in PBS, then incubated with 1:100 anti-mouse oligo-conjugated
1013 antibodies from Ultivue Kit 2 for DNA-PAINT imaging³³. After washing the sample 3
1014 times in PBS, and just before imaging, 2nM of complementary oligos coupled to Cy3
1015 fluorophores were added to the sample.

1016 Nuclear pore imaging data of gp210 and WGA (**Figure 6a-c** and
1017 **Supplementary Figure 14**) were kindly provided by J. Sellés and O. Falklaris and
1018 obtained from nuclear membranes of *Xenopus* frog eggs prepared as described
1019 previously³⁶.

1020 For mitochondria imaging experiments (**Figure 6e-f**), COS7 cells were
1021 cultured under the same conditions as U-373 cells above using phenol-red free
1022 DMEM medium and fixed with 4% PFA in PBS for 10 min. The sample was blocked
1023 with 3% BSA in PBS for 20 min and immunostained with 1:500 mouse antibodies

1024 against TOM22 (Sigma, ref. T6319) in wash buffer (PBS with 0.5% BSA) for 1 h.
1025 After extensive washing with wash buffer, the sample was incubated with 1:500
1026 anti-mouse secondary antibodies from donkey conjugated to Alexa-647 dyes
1027 (Jackson ImmunoResearch Laboratories, ref. 715-605-151) in wash buffer for 30
1028 min. After washing 5 times with wash buffer and 2 times with PBS, samples were
1029 post-fixed with 2% PFA in PBS for 10 min and washed 5 times with PBS.

1030 For all localization microscopy experiments except DNA-PAINT, we used a
1031 photoswitching buffer⁵⁹ composed of 50 mM Tris-HCl + 10 mM NaCl + 10% (w/v)
1032 glucose + 168 AU/mL Glucose-Oxidase + 1404 AU/mL Catalase + 1% 2-
1033 Mercaptoethanol. For microtubule imaging experiments, we used this buffer to fill a
1034 square hole that was manually cut in a parafilm sheet, which was deposited on a
1035 rectangular coverglass. The round coverslips were sealed with nail polish.

1036

1037 **Image acquisition in localization and high-throughput microscopy**

1038 We performed single molecule localization microscopy experiments (PALM/STORM
1039 and DNA-PAINT) on custom built microscopy systems, as previously described⁵⁹⁻⁶¹.
1040 The system used for PALM/STORM imaging of microtubules is based on an inverted
1041 microscope body (Nikon Ti Eclipse) equipped with a either a 60x 1.49 NA oil
1042 immersion objective (Nikon) or a 60x 1.2 NA water immersion objective (Nikon)
1043 and with the Perfect Focus System active. A 642 nm wavelength laser with 500 mW
1044 power was used to excite Alexa-647 fluorophores and an AOTF (AA optics) was used
1045 to modulate laser excitation. Sequences of diffraction limited single molecule image
1046 frames were acquired either on a sCMOS camera (Hamamatsu ORCA-Flash4.0),

1047 which can capture images of 2,042x2,042 pixels (for **Figures 4, 5a-i**), or on an
1048 EMCCD (Andor IXON ULTRA 897) with 512x512 pixels (for **Figures 3, 6d-f**). Both
1049 cameras were controlled by MicroManager software⁶². For experiments using the
1050 sCMOS camera, the effective pixel size was 108 nm and we used a 512x512 region of
1051 interest, which resulted in an imaged FoV of 55.3 μm x 55.3 μm . For experiments
1052 using the EMCCD camera, we used a 2x telescope and the effective pixel size was
1053 107 nm, resulting in a FoV of 54.8 μm x 54.8 μm . The exposure time was set to Δt
1054 =10 ms or 30 ms per frame. The number of frames acquired ranged from $k=1,000$
1055 (**Figure 4**) to $K=60,000$ (e.g. **Figure 5c**) per FoV.

1056 For the DNA-PAINT experiment (**Figure 5j,l**), we used an inverted Nikon Ti-E
1057 Eclipse microscope equipped with a 100x 1.49 NA TIRF objective and with the
1058 Perfect Focus System active. A 561 nm wavelength laser with 500 mW power was
1059 used to excite Cy3 dyes. Highly inclined laser illumination was used to reduce out-
1060 of-focus background signal. Images were acquired on an EMCCD camera as above,
1061 with a 1.5 x telescope, resulting in an effective pixel size of 106 nm and a FoV of
1062 54 μm x 54 μm . The sample was mounted in a magnetic sample holder filled with
1063 the imaging buffer provided with the Ultivue kit. Exposure time was set to $\Delta t =30$ ms
1064 and the EM gain of the EMCCD was set to 300. The laser power was increased until
1065 isolated fluorescent spots were observed. For the experiment shown in **Figure 5g,i**,
1066 $K=60,000$ frames were acquired.

1067 The *Xenopus* nuclear pore data (**Figure 6a-c** and **Supplementary**
1068 **Figure 14**), were acquired on a Zeiss Elyra P.S.1 microscope as described
1069 previously³⁶.

1070 For high-throughput imaging of microtubules (**Figure 4**), we used the Multi-
1071 Dimensional Acquisition tool in Micro-manager to define the positions of 1,089 FoVs
1072 of 55.3 μm x 55.3 μm on a 33x33 grid, with overlaps of 1 μm ; the stage was
1073 automatically shifted to each of these 1,089 positions. We first acquired only
1074 widefield images, taking five frames at each of these positions (the first two were
1075 ignored because of motion blur), in a total acquisition time of 12 minutes. Then, the
1076 laser power was raised to bleach out preactivated molecules and $k=1,000$ frames of
1077 single molecule images were acquired at each of the 1,089 positions, in a total
1078 acquisition time of 3 hours and 8 minutes. Raw image frames were written directly
1079 to a remote storage server via Samba networking protocol.

1080

1081 **Localization microscopy image analysis**

1082 The input to ANNA-PALM reconstruction is a localization image, defined as a 2D
1083 histogram of n single molecule positions $(x_i, y_i)_{i=1..n}$. The histogram bin, i.e. the
1084 pixel size of the localization image, was set to 7.8 nm for the simulated data
1085 (**Figure 2** and **Supplementary Figures 1-6,15**) and 20 nm for the experimental
1086 data (**Figures 3-6** and **Supplementary Figures 7-14**). The positions $(x_i, y_i)_{i=1..n}$
1087 were obtained by analyzing sequences of diffraction limited frames using standard
1088 single molecule localization algorithms. For experimental microtubule images, we
1089 used the ThunderSTORM⁶³ plugin of ImageJ, applying wavelet filters for detection
1090 and weighted least squares Gaussian fitting for precise estimation of subpixelic
1091 positions. We used the cross-correlation feature in ThunderSTORM for drift
1092 correction, and filtered out the least certain localizations based on the fitted

1093 Gaussian's standard deviation and the χ^2 of the residual. Localizations in
1094 consecutive frames separated by less than 20 nm were assumed to originate from
1095 the same molecule and merged into a single localization. The final number n of
1096 localizations was ~ 7 million for the full $55 \mu\text{m} \times 55 \mu\text{m}$ FoV of the images shown in
1097 **Figure 3** and **Supplementary Figures 8,9** (obtained from $K=30,000$ frames). For
1098 the high-throughput experiment (**Figure 4** and **Supplementary Figure 12**), the
1099 number of localizations per $55 \mu\text{m} \times 55 \mu\text{m}$ FoV ranged from $n=2,949$ to
1100 $n=1,442,048$ with an average $\langle n \rangle = 610,983$ and standard deviation $\sigma(n) = 273,606$.
1101 The total number of localizations across all 1,089 FoVs was ≈ 665 million.
1102 ThunderSTORM analyses were performed either on high end workstations or on
1103 Institut Pasteur's high performance computer (HPC) cluster. For the high-
1104 throughput experiments, we used Python scripts to run ThunderSTORM in batch
1105 mode (without user intervention) on the HPC cluster and assembled mosaic images
1106 (**Figure 4a,b** and **Supplementary Figure 12a,b**) using a stitching plugin of
1107 ImageJ⁶⁴.

1108 The nuclear pore images were analyzed using the ZEN software from Zeiss as
1109 previously described³⁶. For the DNA-PAINT experiments, we used PALMTT, a
1110 modified version of the single molecule tracking algorithm MTT⁶⁵, based on Matlab
1111 (Mathworks). This algorithm uses Gaussian smoothing and thresholding for
1112 detection, and Gaussian fitting for precise estimation of subpixelic positions. Drift
1113 correction was performed computationally by tracking fluorescent beads used as
1114 fiducial markers.

1115

1116 **Quality metrics and sampling resolution**

1117 In order to quantitatively assess the quality of PALM images and ANNA-PALM
1118 reconstructions, we calculated the multi-scale structural similarity index (MS-SSIM)
1119 between either image and the ground truth (**Figure 2g** and **Supplementary**
1120 **Figures 5,9**). For the simulated data, the ground truth was simply defined as the
1121 “perfect” PALM image, corresponding to an infinite number of localizations (see
1122 ‘Image simulations’ above, **Figure 2e** and **Supplementary Figure 1c**). For the
1123 experimental data, the ground truth was defined as the ANNA-PALM reconstruction
1124 of a dense PALM image obtained from all available frames (e.g. **Supplementary**
1125 **Figure 9c**). Before calculation of the MS-SSIM, all simulated images were linearly
1126 normalized without clipping to a maximum value of 255.

1127 In order to evaluate the effect of sampling on the resolution of PALM images,
1128 we computed the double mean distance, $R_{\text{Nyq}} = 2\langle d \rangle$ between nearest neighbors in
1129 the underlying sets of localizations⁴⁹ as function of localization number
1130 (**Supplementary Figure 3d**). For the simulated sparse PALM data, sets of
1131 localizations were obtained by interpreting each image \mathbf{S} as a 2D histogram of
1132 localizations, and creating a random subpixelic position $(x_k, y_k)_{k=1..m}$ within each
1133 pixel (i, j) , as many times as given by the pixel value $m = S(i, j)$ (therefore resulting
1134 in a set of $n = \sum_{i,j} S(i, j)$ localizations). The quantity $R_{\text{Nyq}}(n) = 2\langle d(n) \rangle$ decreases
1135 towards zero with increasing number of localizations, n . A Nyquist criterion
1136 introduced in ref.⁴⁹ suggests that the resolution is limited by sampling to no less
1137 than R_{Nyq} , implying that at least $n \geq N_{\text{Nyq}} = R_{\text{Nyq}}^{-1}(R)$ localizations are needed to
1138 achieve a given resolution R . However, a more stringent and realistic criterion³

1139 prescribes a five-fold larger number of localizations to reach resolution R :
1140 $n \geq N_{5 \times Nyq} = 5 \times N_{Nyq}$, implying that the sampling limit to resolution is
1141 $R_{5 \times Nyq} = 2\langle d(n/5) \rangle$. Accordingly, if this condition is met, the resolution is no longer
1142 limited by sampling, but by the localization precision, $R_{loc} \approx 2.3\sigma_{loc}$, where σ_{loc} is
1143 the standard deviation of localization errors along each coordinate. In general, the
1144 resolution of a PALM image, as limited by both sampling and localization precision,
1145 can be written: $R = \max(R_{5 \times Nyq}, R_{loc}) = \max(2\langle d(n/5) \rangle, 2.3\sigma_{loc})$.

1146

1147 **Life Sciences Reporting Summary.**

1148 Further information is available in the Life Sciences Reporting Summary.

1149

1150 **Code availability statement**

1151 The source code of ANNA-PALM is available from <https://annapalm.pasteur.fr/>.

1152

1153 **Data availability statement**

1154 The localization data used in this paper can be downloaded directly from
1155 <https://annapalm.pasteur.fr/>.

1156

1157 **Methods-only references**

- 1158 51. Xu, L., Choy, C. S. & Li, Y. W. Deep sparse rectifier neural networks for speech
1159 denoising. in *2016 International Workshop on Acoustic Signal Enhancement,*
1160 *IWAENC 2016* (2016). doi:10.1109/IWAENC.2016.7602891
1161 52. Maas, A. L., Hannun, A. Y. & Ng, A. Y. Rectifier Nonlinearities Improve Neural
1162 Network Acoustic Models. *Proc. 30 th Int. Conf. Mach. Learn.* (2013).
1163 53. Mao, X. *et al.* Least Squares Generative Adversarial Networks. in *ICCV 2794–*
1164 *2802* (2017). doi:10.1109/ICCV.2017.304

- 1165 54. Kingma, D. P. & Ba, J. Adam: A Method for Stochastic Optimization. *ICLR* 1–15
1166 (2015).
1167 doi:<http://doi.acm.org.ezproxy.lib.ucf.edu/10.1145/1830483.1830503>
1168 55. Rampasek, L. & Goldenberg, A. TensorFlow: Biology’s Gateway to Deep
1169 Learning? *Cell Syst.* **2**, 12–14 (2016).
1170 56. Srinivasa Reddy, B. & Chatterji, B. N. An FFT-based technique for translation,
1171 rotation, and scale-invariant image registration. *IEEE Trans. Image Process.* **5**,
1172 1266–1271 (1996).
1173 57. Simard, P. Y., Steinkraus, D. & Platt, J. C. Best practices for convolutional neural
1174 networks applied to visual document analysis. *Seventh Int. Conf. Doc. Anal.*
1175 *Recognition, 2003. Proceedings.* **1**, 958–963 (2003).
1176 58. Plimpton, S. Fast Parallel Algorithms for Short-Range Molecular Dynamics. *J.*
1177 *Comput. Phys.* **117**, 1–19 (1995).
1178 59. van de Linde, S. *et al.* Direct stochastic optical reconstruction microscopy with
1179 standard fluorescent probes. *Nat. Protoc.* **6**, 991–1009 (2011).
1180 60. Henriques, R. *et al.* QuickPALM: 3D real-time photoactivation nanoscopy
1181 image processing in ImageJ. *Nat. Methods* **7**, 339–340 (2010).
1182 61. Lelek, M. *et al.* Superresolution imaging of HIV in infected cells with FLAsH-
1183 PALM. *Proc. Natl. Acad. Sci. U. S. A.* **109**, 8564–9 (2012).
1184 62. Edelstein, A., Amodaj, N., Hoover, K., Vale, R. & Stuurman, N. Computer control
1185 of microscopes using manager. *Current Protocols in Molecular Biology* (2010).
1186 doi:10.1002/0471142727.mb1420s92
1187 63. Ovesny, M., Kiek, P., Borkovec, J., Vindrych, Z. & Hagen, G. M. ThunderSTORM:
1188 a comprehensive ImageJ plug-in for PALM and STORM data analysis and
1189 super-resolution imaging. *Bioinformatics* **30**, 2389–2390 (2014).
1190 64. Preibisch, S., Saalfeld, S. & Tomancak, P. Globally optimal stitching of tiled 3D
1191 microscopic image acquisitions. *Bioinformatics* **25**, 1463–1465 (2009).
1192 65. Sergé, A., Bertaux, N., Rigneault, H. & Marguet, D. Dynamic multiple-target
1193 tracing to probe spatiotemporal cartography of cell membranes. *Nat Methods*
1194 **5**, 687–694 (2008).
1195
1196

1197

1198

1199

1200

1 **ANNA-PALM: Deep learning accelerates super-resolution localization**
2 **microscopy by orders of magnitude**

3

4

5 Wei Ouyang^{1,2,3}, Andrey Aristov^{1,2,3}, Mickaël Lelek^{1,2,3}, Xian Hao^{1,2,3}, Christophe
6 Zimmer^{1,2,3}

7

8 ¹ Institut Pasteur, Unité Imagerie et Modélisation, Paris, France

9 ² UMR 3691, CNRS

10 ³ C3BI, USR 3756, IP CNRS

11

12

13

14

15

16

17

18

19

20

21

22 Corresponding author: C. Zimmer

23 **The speed of super-resolution microscopy methods based on single molecule**
24 **localization, e.g. PALM or STORM, is severely limited by the need to record**
25 **many thousands of frames with a low number of observed molecules in each.**
26 **Here, we present ANNA-PALM, a computational strategy that uses artificial**
27 **neural networks to reconstruct super-resolution views from sparse, rapidly**
28 **acquired localization images and/or widefield images. Simulations and**
29 **experimental imaging of microtubules, nuclear pores and mitochondria show**
30 **that high-quality super-resolution images can be reconstructed from up to two**
31 **orders of magnitude fewer frames than usually needed, without**
32 **compromising spatial resolution. Super-resolution reconstructions are even**
33 **possible from widefield images alone, though adding localization data**
34 **improves image quality. We demonstrate super-resolution imaging of >1,000**
35 **fields of view containing >1,000 cells in ~3 h, yielding an image spanning**
36 **spatial scales from ~20 nm to ~2 mm. The drastic reduction in acquisition**
37 **time and sample irradiation afforded by ANNA-PALM enables faster and**
38 **gentler high-throughput and live cell super-resolution imaging.**

39
40 Fluorescence microscopy methods that overcome the diffraction limit of resolution
41 (~200-300 nm) allow imaging of biological structures with molecular specificity
42 closer to the molecular scale. Among super-resolution microscopy approaches,
43 those based on single molecule localization, such as PALM¹ or STORM² (hereafter
44 referred to collectively as PALM) are particularly attractive owing to their exquisite
45 spatial resolution and ease of implementation. In these methods, random subsets of
46 fluorophores are imaged in many consecutive diffraction-limited frames,
47 computationally localized to high precision, and the combined localizations are used
48 to generate a super-resolution view. In practice, typically 10^3 - 10^5 diffraction-limited
49 frames are needed to assemble a single super-resolution image. This requirement
50 follows from two conditions that must be simultaneously satisfied to ensure high
51 spatial resolution: (i) a low number (~ 10 - 10^2) of active fluorophores per frame, to
52 avoid overlaps between diffraction limited spots and enable precise localization of
53 individual molecules, and (ii) a large number of independent localizations to ensure
54 a sufficiently dense sampling of the underlying biological structures^{3,4}. The large
55 number of required frames makes localization microscopy inherently slow, thereby
56 limiting its potential for high-throughput imaging, where many fields of view (FoVs)
57 are to be imaged, and for imaging live cell dynamics. As a result, most localization
58 microscopy studies are restricted to analyzing a small number of cells (typically less
59 than ten).

60 Multiple approaches have been explored to accelerate localization
61 microscopy. Using bright dyes with rapid switching kinetics, high power lasers and
62 fast cameras allows to minimize exposure time without losing signal to noise

63 ratio^{5,6}, but reaching sub-millisecond exposure remains challenging, and intense
64 irradiation exacerbates phototoxicity in live cell imaging^{7,8}. Increasing the number
65 of active fluorophores per frame can reduce acquisition time, but despite algorithms
66 designed to handle overlapping fluorescent spots⁹⁻¹³ this approach necessarily
67 compromises spatial resolution^{14,15}.

68 Here, we introduce a computational strategy that allows reducing the total
69 number of frames and independent localizations without losing spatial resolution.
70 Unlike previous approaches, our method leverages the structural redundancy of
71 most biological images to reconstruct high quality images from vastly under-
72 sampled localization microscopy data. Our method leverages deep learning, which
73 employs artificial neural networks (ANNs) to learn complex non-linear mappings
74 between numerical inputs and outputs¹⁶. Accordingly, we call it ‘artificial neural
75 network accelerated PALM’, or ANNA-PALM.

76

77 **RESULTS**

78 **A deep learning approach to super-resolution image reconstruction**

79 We aim to reconstruct a super-resolution image of approximately similar
80 information content as a standard PALM acquisition (with K frames and N
81 localizations) from a much smaller number of raw frames ($k \ll K$) without changing
82 the average density of localizations, ρ , i.e. from a much smaller number of total
83 localizations ($n = \rho k \ll N = \rho K$). If PALM images are defined as 2D histograms of
84 independent localizations, this task can be formulated as restoring an image
85 corrupted by Poisson noise (and potentially additional forms of noise). Image

86 restoration is an ill-posed problem that has an infinity of solutions in the high-
87 dimensional space of all possible images, unless additional constraints (priors) are
88 imposed that restrict the solution to a lower dimensional subspace. Suitable
89 subspaces exist because most natural images are highly redundant, and can be
90 represented to very good approximation with a much smaller number of coefficients
91 than pixels, via appropriate functions that map feature space to pixel space^{17,18}. In
92 recent years, ANNs with multiple layers (deep nets) have proven very successful at
93 learning meaningful features and non-linear mappings for image classification,
94 segmentation, restoration and many other tasks^{16,18,19}. Inspired by these
95 developments, we designed ANNA-PALM, a deep learning approach for restoring
96 super-resolution views from under-sampled (sparse) localization microscopy data.

97 ANNA-PALM comprises a training stage and an inference stage (**Figure 1**).
98 For training (**Figure 1a**), a few super-resolution images representative of the
99 structure of interest (e.g. microtubules, nuclear pores, or mitochondria) are
100 obtained using standard PALM imaging, i.e. by acquiring long diffraction limited
101 image sequences (e.g. $K \sim 10^4 - 10^5$, $N \sim 10^5 - 10^7$) and processing them with
102 standard localization software²⁰, resulting in highly sampled (dense) PALM images.
103 In addition, a low resolution (widefield) image can also be acquired, as is commonly
104 done before single molecule imaging when bleaching out preactivated fluorophores.
105 Next, the dense PALM images are under-sampled by using a much smaller number
106 of input frames, $k \ll K$, thus yielding sparse PALM images from the same
107 localization data. Then, an ANN is trained to recover approximations of the dense
108 PALM images from these sparse PALM images (and the optional widefield image).

109 Once trained, the ANN is applied to new sparse PALM images (with or without a
110 widefield image), obtained from new image sequences with small numbers of
111 frames ($k \ll K$) -and hence in much shorter time- in order to reconstruct high
112 quality super-resolution images not previously seen (inference, **Figure 1b**).

113

114 **Neural net architecture and learning strategy**

115 Our ANN, hereafter called A-net, contains a total of 25 convolutional layers, and
116 roughly 42 million trainable parameters. A-net is adapted from the pix2pix
117 network²¹, which itself builds on U-nets²² and generative adversarial networks
118 (GANs)²³, two recent successful deep learning techniques. U-nets are special types of
119 convolutional neural networks (CNNs) that have proven effective at learning multi-
120 scale representations of images and accurate, pixel-wise mappings^{22,24}. GANs can
121 generate new samples from real image distributions using a generator network that
122 outputs synthetic images, and a discriminator network that outputs the probability
123 that an input image is real or synthetic, both networks being trained simultaneously
124 to compete against each other²³. Importantly, the generator can be conditioned on
125 input data (conditional GAN, or cGAN)^{21,23}, e.g. on images as in the pix2pix network.
126 We modified the pix2pix architecture to accept a computational switch as additional
127 input to handle multiple types of data, and introduced an additional network to
128 evaluate the consistency between the reconstructed image and the widefield input
129 image.

130 Training of our A-net proceeds as follows. Randomly under-sampled (i.e.
131 sparse) versions of PALM images are fed as input to the A-net, while the

132 corresponding dense PALM images are defined as the A-net's targets, i.e. desired
133 outputs (**Figure 1a**). Additional, optional inputs are widefield images, if available,
134 and the switch, which indicates the image type when multiple types of images (e.g.
135 microtubules and nuclear pores) are used during training. ANN training requires
136 defining an objective function (also called loss), which measures how well the
137 outputs match the targets. We implemented a loss function containing three terms.
138 The first term measures the difference between the A-net output and the dense
139 PALM image. Instead of the widely used mean squared error (MSE), which poorly
140 reflects visual quality²⁵, we used a combination of the absolute difference (L1 norm)
141 with a multi-scale version of the structural similarity index, a perceptually
142 motivated quality metric shown to improve image restoration with deep learning
143 (MS-SSIM)²⁶. The second term measures the consistency between the A-net output
144 and the widefield image. Although in theory the latter should simply be a blurred
145 version of the PALM image, this is often not the case in practice²⁷. Therefore, we
146 introduced another CNN (with 4-layers), called 'low resolution estimator' to predict
147 the widefield image from the super-resolution image. The corresponding loss was
148 defined as the MS-SSIM between this CNN's output and the observed widefield
149 image. (In absence of a widefield image, this loss is set to zero). The third term
150 contains a cGAN discriminator loss²¹, where the discriminator is a 5-layer CNN,
151 whose inputs are the sparse PALM (and widefield) image(s) and either the dense
152 PALM image or the output of the generator above; the discriminator's output is
153 compared to 0s and 1s (for synthetic and real, respectively), respectively, via the
154 MSE. We use dropout²⁸ and extensive data augmentation, including random

155 rotations, translations, elastic deformations and addition of noise in the input image
156 to mimic false detections and unspecific labeling. As a result, only a few dense PALM
157 images are required for successful training without overfitting. On graphical
158 processing units (GPU), training ANNA-PALM from scratch takes on the order of
159 hours to days, but when starting from a previously trained A-net, retraining can be
160 done in an hour or less.

161 Once trained, the A-net can take sparse localization data with an optional
162 widefield image as input(s), and output a reconstructed super-resolution image in
163 less than a second (**Figure 1b**). In addition, the A-net produces an ‘error map’ that
164 measures the consistency of this super-resolution image with the widefield image²⁷
165 (when available) and can be used to estimate the degree of reliability and highlight
166 potential reconstruction artifacts. For more details, see **Online Methods** and
167 **Supplementary Note 1**.

168

169 **Validating ANNA-PALM on simulated images**

170 We first sought to validate ANNA-PALM on synthetic data. For this, we used
171 Brownian dynamics simulations²⁹ to generate 200 dense PALM images of semi-
172 flexible filaments mimicking microtubules, with a resolution $R_{loc} \approx 23$ nm. These
173 represent “perfect” PALM images that would be obtained with an infinite number of
174 localizations. We applied varying levels of Poisson noise to these perfect images to
175 create sparse PALM images corresponding to finite numbers of localizations
176 (**Supplementary Figure 1**). We then trained our A-net using the perfect images as

177 targets and the sparse images (and widefield image) as inputs, varying the number
178 of localizations over a large range.

179 Next, we applied the trained A-net to a distinct set of PALM images generated
180 by the same stochastic simulation (**Supplementary Figure 2**). **Figure 2a** shows a
181 widefield image and **Figure 2b** a corresponding sparse PALM image obtained from
182 $n=6,834$ localizations. Although curvilinear structures can be seen in this image
183 despite its sparsity, small-scale features remain highly ambiguous (**Figure 2b**,
184 inset), and the resolution according to a recently proposed five-fold Nyquist
185 criterion³ is limited by sampling to $R_{5 \times Nyq} \approx 85$ nm; according to this criterion,
186 $N > N_{5 \times Nyq} = 60,000$ localizations are needed to achieve 23 nm resolution
187 (**Supplementary Figure 3d**). **Figure 2c** shows the ANNA-PALM image
188 reconstructed from the wide-field image alone, which exhibits clear and continuous
189 filaments that were not previously recognizable. Most of the relatively isolated
190 filaments roughly agree with the perfect PALM image (**Figure 2e**). In the denser
191 regions, however, many small features are erroneous, e.g. filaments are incorrectly
192 joined, displaced, split or merged (**Figure 2c**, blue arrows and **Supplementary**
193 **Figure 4, top**). By contrast, the ANNA-PALM image reconstructed from the sparse
194 PALM image alone or in combination with the widefield image exhibits continuous
195 and sharp filaments in very good agreement with the perfect PALM image
196 (**Supplementary Figure 3b,c** and **Figure 2d,e,f**). The spatial resolution of these
197 reconstructed images is limited neither by diffraction nor sampling, but only by the
198 localization precision, and is thus $R_{loc} \approx 23$ nm, as in the perfect images
199 (**Supplementary Figure 3e,f**). These results indicate that high quality super-

200 resolution images can be obtained from only a small fraction of the number of
201 localizations traditionally required (here, approximately $\sim 11\%$ of $N_{5\times Nyq}$ above; see
202 **Supplementary Figure 3d**), hence enabling a strong reduction in acquisition time.
203 Nevertheless, reconstruction errors can still occur in areas where the sparse
204 localization data are most ambiguous, e.g. where filament density is highest
205 (**Figure 2d,e,f**, white arrow). These errors can be reduced by increasing the
206 localization number n , implying a trade-off between acquisition time and
207 reconstruction quality (**Supplementary Figure 4**).

208 To quantify this trade-off, we computed the MS-SSIM between reconstructed
209 ANNA-PALM and perfect PALM images ($n = \infty$) as function of localization number,
210 from $n \sim 200$ to $n \sim 2 \times 10^6$, in comparison with the standard PALM images
211 (**Figure 2g**). The MS-SSIM ranges from 0 to 1 and reaches 1 for perfect
212 reconstructions. For standard PALM images, the MS-SSIM increases monotonically,
213 as expected, from < 0.2 to > 0.95 for $n = 2 \times 10^6$ million localizations (**Figure 2g**, black
214 curve). Using only the sparse image as input, ANNA-PALM reconstructions achieve
215 MS-SSIM that are consistently higher and increase with localization number n much
216 more rapidly than standard PALM, already exceeding 0.9 for $n \approx 10,000$
217 localizations (**Figure 2**, dashed blue curve). ANNA-PALM achieves the same MS-
218 SSIM as standard PALM at the five-fold Nyquist sampling level (≈ 0.65) with only
219 $n = 2,248$ localizations instead of $n = 58,588$, suggesting a ~ 26 -fold speed-up. If the
220 widefield image is used as additional input, the MS-SSIM further increases, and
221 dramatically so for low localization numbers (**Figure 2g**, solid blue curve). For
222 example, with $n = 7,477$ localizations, ANNA-PALM achieves a MS-SSIM (≈ 0.95)

223 similar to standard PALM with $n = 644,844$, implying a speed-up of roughly two
224 orders of magnitude. (Note that, if the perfect PALM image was not available for
225 these quantifications, it could be replaced by the ANNA-PALM reconstruction of a
226 dense PALM image with a large number of localizations, e.g. $n = 10^5$, with similar
227 results- see **Supplementary Figure 5**).

228 As any image restoration method, ANNA-PALM can make errors. The low
229 resolution error map described above (**Figure 1b**) provides a means to estimate
230 where errors are most likely to occur. When applied to ANNA-PALM reconstructions
231 of a sparse PALM image, this error map highlights regions containing the highest
232 density of filament crossings, where reconstructions tend to be least accurate
233 (**Supplementary Figure 6i,k**). If we artificially displace a small piece of filament in
234 this image to simulate a false positive and a false negative in the reconstruction
235 (**Supplementary Figure 6b,d**, white and blue arrows, respectively), the affected
236 regions also light up in the error map (**Supplementary Figure 6j,l**). Thus, the error
237 map offers a useful tool to highlight regions most likely to contain reconstruction
238 errors, and conversely, to outline regions where reconstructions are most
239 trustworthy. Thus, simulations suggest that ANNA-PALM can considerably reduce
240 acquisition time in localization microscopy and also map reconstruction reliability.

241

242 **ANNA-PALM reconstructions of immunostained microtubules**

243 We next tested our method on real images of immunolabeled microtubules
244 (**Figure 3**). We trained our A-net on seven dense PALM images (with corresponding
245 widefield images) obtained during 10 minute long acquisitions ($K=60,000$;

246 $\Delta t=10$ ms exposure time) (not shown). We then considered a sparse PALM image of
247 microtubules in a distinct FoV obtained from only 9 s of acquisition ($k=300$; $\Delta t=30$
248 ms), together with a widefield image ($\Delta t=2 \times 50$ ms) (**Figure 3a,b**). Whereas
249 microtubule filaments can already be seen in this sparse PALM image, structural
250 details below the diffraction limit are hard to discern, making it difficult to follow
251 the path of individual filaments in the denser regions and to identify features such
252 as filament crossings (**Figure 3b**). By contrast, the ANNA-PALM images, whether
253 reconstructed from the widefield image alone, the sparse PALM image alone, or
254 both, all display sharp and continuous filaments and clearly reveal many structural
255 details (**Figure 3d-f**). Their resolution is similar to or even better than the dense
256 PALM image (**Supplementary Figure 7a**). As for the simulations, in regions where
257 microtubule filaments are isolated, the ANNA-PALM image reconstructed from the
258 widefield image alone is in good agreement with the dense PALM image
259 (**Figure 3d,g**). However, it is often incorrect in areas of high microtubule density
260 (e.g. **Figure 3d,g** white and gray arrows). Most of these reconstruction errors are
261 corrected when applying ANNA-PALM to the sparse PALM image instead
262 (**Figure 3e,h**). For example, parallel sections of two microtubules unresolved in the
263 widefield image and incorrectly merged in **Figure 3d** are now clearly separated and
264 positioned correctly, and missed portions of other filaments are now recovered
265 (**Figure 3h**, white and gray arrows). Counter-intuitively, the sparse PALM image
266 exhibits high signal in some locations where the dense PALM image does not,
267 presumably because of spurious localizations due e.g. to unspecific binding
268 (**Figure 3b**, blue arrow). Such signal can lead to incorrect features in the ANNA-

269 PALM reconstruction from the sparse localization data alone (**Figure 3e,h**, blue
270 arrows). However, when combining the widefield and sparse PALM data, these
271 artifacts are largely removed and reconstructions agree very well with the dense
272 PALM image (**Figure 3f,i**). Reconstruction quality increases with the number of
273 frames k (**Figure 3j**, **Supplementary Figures 8-9** and **Supplementary Video 1**).
274 More quantitatively, a MS-SSIM analysis similar to that for the simulated data above
275 (with the ANNA-PALM output of the dense PALM image defined as ground truth; see
276 **Supplementary Figures 5, 9f**) suggests that ANNA-PALM allows a hundred-fold
277 reduction of acquisition time compared to standard PALM (**Supplementary**
278 **Figure 9g**). **Supplementary Figure 10** shows other examples of sparse
279 microtubule images reconstructed by ANNA-PALM.

280 As for simulations above, we used the widefield image to compute an error
281 map (**Supplementary Figures 6,11**). Bright areas in this error map highlight
282 regions where the reconstruction indeed disagrees with the dense PALM image;
283 conversely, reconstructions are of high quality in the majority of regions where the
284 error map is dim (**Supplementary Figure 11d-f**). These results demonstrate
285 experimentally that ANNA-PALM can restore high quality approximations of super-
286 resolution images from much shorter acquisition time than typical for PALM
287 imaging, and also predict where reconstruction errors are most likely.

288

289 **ANNA-PALM enables high-throughput super-resolution imaging**

290 The drastic improvement in imaging efficiency afforded by ANNA-PALM permits
291 super-resolution imaging of orders of magnitude more cells and FoVs per unit time.

292 To demonstrate this, we used an automated acquisition protocol to image >1,000
293 cells with immunolabeled microtubules in 1,089 (33x33), partly overlapping, FoVs
294 of 55.3 μm x 55.3 μm each (**Figure 4, Supplementary Figure 12**). We first acquired
295 widefield images at each of these positions, in a total of \sim 12 minutes, mostly
296 consisting of stage stabilization delays (**Supplementary Figure 12a**). Next, we
297 obtained 1,089 sparse PALM images using only 10 s of imaging time per FoV
298 ($k=1,000$ frames, $\Delta t = 10$ ms), in a total of only \sim 3.1 hours (**Figure 4a**). Neither the
299 widefield nor the sparse PALM images provided much small scale information
300 (**Figure 4c, Supplementary Figure 12 c,e**). However, ANNA-PALM reconstructions
301 led to high quality super-resolution images, allowing to visualize the microtubule
302 network with clarity and to distinguish microtubule filaments in dense areas that
303 appeared as unstructured regions in the sparse PALM image (**Figure 4b,d**). The
304 FWHM across filaments in the reconstructed image was \sim 51 nm (**Figure 4d**), within
305 the range measured for the training data (**Supplementary Figure 7a**). Similar
306 images can be obtained by ANNA-PALM using the widefield images alone
307 (**Supplementary Figure 12**), although of lower quality, as discussed above.
308 Stitching the reconstructed images together yielded a single super-resolution image
309 that contained approximately seven billion 20x20 nm pixels and covered an area of
310 1.8 mm x 1.8 mm, thereby spanning almost five orders of magnitude in spatial scales
311 (**Figure 4b,d, Supplementary Figure 12b and Supplementary Video 2**).

312

313 **ANNA-PALM is robust to experimental perturbations**

314 ANNA-PALM can reconstruct accurate super-resolution images from sparse data
315 because it was trained on similar images before. This raises the question of whether
316 an ANN trained in one experimental condition can be successfully applied to
317 another condition. To test this, we used the A-net as trained above to analyze
318 microtubule images of cells subjected to drugs affecting the cytoskeletal network.
319 We first treated U373 cells with 1 μ M of Taxol, an antimicrotubule agent that inhibits the
320 depolymerization of microtubules and increases their bending rigidity^{30,31}.
321 **Figure 5d** shows a sparse PALM image of these cells ($k=800$, $k\Delta t=8$ s), in which the
322 microtubule network is barely recognizable. By contrast, the ANNA-PALM
323 reconstructions clearly display a complex microtubule network and agree well with
324 the dense PALM image obtained from $K=60,000$ frames ($K\Delta t=10$ min)
325 (**Figure 5d,e,f**). These images display a larger density of straighter and more
326 parallel filaments with less frequent crossings than in the untreated cells
327 (**Figure 5a-c**), consistent with microtubule stabilization and increased rigidity³¹.

328 Next, we treated cells with 1 μ M of Nocodazole, a drug that, on the opposite,
329 promotes microtubule depolymerization and is expected to more dramatically alter
330 the cytoskeletal network³². Again, whereas the sparse image obtained from $k=300$
331 frames ($k\Delta t=3$ s) contained little exploitable information (**Figure 5g**), the ANNA-
332 PALM reconstruction offered clear and detailed views of the disrupted microtubule
333 network (**Figure 5h**), exhibiting a much smaller number of filaments, with higher
334 curvature, than in untreated cells. These reconstructions were in good (though not
335 perfect) agreement with dense PALM images obtained from $K=60,000$ frames
336 ($K\Delta t=10$ min) (**Figure 5i**). Thus, ANNA-PALM, when trained on microtubules in

337 one experimental condition, may be successfully applied to new experimental
338 conditions without retraining, thereby highlighting the method's robustness to
339 biologically relevant structural alterations.

340 We further asked if ANNA-PALM is robust to changes in technical imaging
341 conditions. To address this, we performed localization microscopy on microtubules
342 by simultaneously changing multiple important imaging parameters relative to the
343 training data. Instead of PALM/STORM, we used DNA-PAINT a technique where
344 single molecule detection relies on transient binding of fluorophore-conjugated
345 short DNA strands to complementary, antibody-conjugated, DNA strands³³, rather
346 than on fluorophore blinking. The continuously emitting freely diffusing dyes lead to
347 higher background noise in DNA-PAINT compared to PALM/STORM. Moreover, we
348 used primary mouse antibodies instead of rat antibodies, Cy3 dyes instead of Alexa-
349 647 dyes, and an EMCCD instead of a sCMOS camera. Despite all these differences,
350 when ANNA-PALM was applied without retraining on a sparse microtubule image
351 ($k=400$ frames, $k\Delta t=12$ s) , the reconstructed image still agreed very well with the
352 dense DNA-PAINT image obtained from $K=60,000$ frames ($K\Delta t=30$ min) (**Figure 5j-**
353 **I**). These data demonstrate the high robustness of ANNA-PALM to changes in
354 experimental imaging conditions.

355

356 **ANNA-PALM adapts to different biological structures**

357 To demonstrate that ANNA-PALM is not restricted to filamentary structure, we
358 turned to nuclear pores, a very different biological structure, and another popular
359 target of super-resolution imaging studies³⁴⁻³⁶. We retrained A-net simultaneously

360 on microtubule images and on a single PALM image of the nucleoporin gp210 in
361 immunolabeled nuclear membranes of *Xenopus* frog eggs^{34,36} ($K=30,000$). With the
362 switch (**Figure 1**) set to microtubules ('MT'), this newly trained A-net can still
363 reconstruct sparse images of microtubules as when trained exclusively on
364 microtubule data (**Supplementary Figure 13a-c**). We then applied the same A-net
365 with the switch set to nuclear pores ('NPC') to reconstruct a new sparse PALM
366 image of gp210 obtained from the first $k=3,000$ frames (**Figure 6a**). The sparsity of
367 this image makes it difficult to clearly distinguish individual nuclear pores. ANNA-
368 PALM, however, reconstructs a much clearer image, containing many easily
369 identifiable ring-like structures, as expected for nuclear pores³⁴ (**Figure 6b**), and in
370 good agreement with the dense PALM image obtained from $K=30,000$ frames (even
371 though the latter shows mostly incomplete, open rings, presumably due to
372 suboptimal labeling) (**Figure 6c**). An automated procedure based on cross-
373 correlation with a ring template indeed identified ~ 2.7 times more putative nuclear
374 pores from the ANNA-PALM image than the sparse image (**Supplementary Figure**
375 **14a-c**). Moreover, computed pore locations were in good agreement with a PALM
376 image of wheat germ agglutinin (WGA), a lectin that concentrates in the inner
377 nuclear pore channel³⁶ (**Supplementary Figure 14 d-f**). These results show that
378 ANNA-PALM can successfully analyze non-filamentary structures, when properly
379 retrained, and that a single ANN, with a simple computational switch, can
380 reconstruct very different types of structures.

381 Finally, we imaged TOM22, a protein of the mitochondrial outer membrane³⁷.
382 Whereas, at the resolution of our experiments, microtubules and nucleoporins are

383 essentially one-dimensional and zero-dimensional structures, mitochondrial
384 membranes are two-dimensional surfaces. Furthermore, their complex 3D
385 morphology might seem less predictable than filaments or nuclear pores, potentially
386 hampering ANNA-PALM reconstruction. Despite these differences, after being
387 trained on nine PALM images of TOM22 (with frame numbers ranging from
388 $K=24,000$ to $K=40,000$), ANNA-PALM reconstructions of distinct sparse PALM
389 images ($k=400$ frames) displayed mitochondrial morphologies in good agreement
390 with the dense PALM images (**Figure 6d-f**) - although the protein's localization
391 along the membrane was less well reproduced. Taken together, our results illustrate
392 the versatility of ANNA-PALM and its applicability to images of very different
393 structural content.

394

395 **Discussion**

396 We introduced ANNA-PALM, a computational method based on deep learning, that
397 reconstructs high quality super-resolution images from sparse, rapidly acquired,
398 single molecule localization data (and/or widefield images). Our method enables
399 considerable gains in acquisition time compared to standard localization
400 microscopy without increasing active fluorophore density, thereby preserving
401 spatial resolution. In fact, ANNA-PALM even improves spatial resolution when
402 applied to images of lower resolution than the training data
403 (**Supplementary Figures 7a, 10**), and greatly diminishes the detrimental effect of
404 drift. The improvement in imaging efficiency afforded by ANNA-PALM alleviates the
405 incompatibility between high resolution and high-throughput microscopy by

406 enabling super-resolution imaging of thousands of cells within a few hours or even
407 less (**Figure 4, Supplementary Figure 12**). This will facilitate super-resolution
408 studies of rare events, cellular heterogeneity and of partly stochastic structures such
409 as cytoskeletal polymers or chromosomes, whose characterization requires
410 statistics on many configurations^{38,39}. ANNA-PALM may also be beneficial for high-
411 throughput imaging screens, e.g. of drug treatments or gene knock-outs⁴⁰⁻⁴². In
412 addition, we envision applications to super-resolution imaging of large samples by
413 stitching together multiple images of spatially adjacent fields. The ability to generate
414 images spanning many orders of magnitude in scale could be well adapted to
415 expansion microscopy, a super-resolution technique that physically increases
416 sample size, but often requires tiling many fields of view to image even a single
417 cell^{43,44}. With correlative microscopy⁴⁵, it might also be possible to train ANNA-
418 PALM to reconstruct electron microscopy (EM) images from fluorescence images,
419 potentially extending the method to molecular resolutions currently out of reach of
420 localization microscopy. Adaptation of ANNA-PALM to 3D^{15,46} and multi-color^{47,48}
421 localization microscopy should be relatively straightforward. Localization
422 microscopy of cellular dynamics remains very challenging^{3,49}. By using much fewer
423 frames (or even only widefield images), ANNA-PALM could dramatically improve
424 the temporal resolution of live cell localization microscopy without sacrificing
425 spatial resolution or increasing phototoxicity and photobleaching. Thus, ANNA-
426 PALM provides multiple novel avenues for multi-scale imaging beyond standard
427 spatio-temporal resolution limits.

428 Nevertheless, important caveats should be stressed. First, although ANNA-
429 PALM can be applied successfully to very different types of images (**Figure 6**), the
430 method fails in absence of statistical redundancies between molecular localizations,
431 e.g. for entirely random distributions of molecules. Second, ANNA-PALM requires
432 prior training on dense PALM images with structures similar to those in the images
433 to be reconstructed. We showed that ANNA-PALM is robust, i.e. does not require
434 retraining, for some experimentally induced changes in structures and variations in
435 imaging parameters (**Figure 5**). Nevertheless, indiscriminate application of ANNA-
436 PALM to very different structures without retraining, or incorrect setting of the
437 switch, may result in artifacts (**Supplementary Figure 13h**). Third, even when
438 applied to data similar to the training images, ANNA-PALM can produce errors -as
439 any reconstruction method in a context of information scarcity. The frequency of
440 errors can be reduced by increasing the number of recorded frames, at the cost of
441 reduced acceleration (see **Figures 2,3** and **Supplementary Figures 4, 8, 9**). In
442 addition, ANNA-PALM can use widefield images to estimate the reliability of
443 reconstructions, thereby helping their interpretation, providing some protection
444 against artifacts and indicating when retraining may be needed (**Supplementary**
445 **Figures 11, 15**). Future work, e.g. using Bayesian deep learning⁵⁰, may provide
446 additional assessments of reconstruction uncertainty and shed more light on the
447 scope and limitations of our approach.

448 As a purely computational technique, ANNA-PALM does not necessitate any
449 changes to existing microscopy systems, but only requires one or a few standard
450 PALM images for training. To facilitate its adoption and future development, we

451 make our source code, an ImageJ plugin and a cloud-computing based web
452 application available on <https://annapalm.pasteur.fr/> along with sample data.
453 Because the performance of deep learning methods improves with the amount and
454 variety of training data, we designed our web application to enable sharing of data
455 and trained ANNs. As ANNA-PALM will learn from an increasing large and diverse
456 collection of images, we expect it to reach even higher accuracy or efficiency and to
457 expand its scope of application in the future.

458

459

460 **Acknowledgements**

461 We thank the following colleagues for useful discussions and suggestions and/or
462 critical reading of the manuscript: C. Leduc, S. Etienne-Manneville, S. Lévêque-Fort,
463 N. Bourg, A. Echard, J-B. Masson, T. Rose, P. Hersen, F. Mueller, M. Cohen, Z. Zhang,
464 and P. Kanchanawong. We also thank the four anonymous reviewers for their
465 constructive criticism, which led to significant improvements of ANNA-PALM. We
466 further thank O. Faklaris, J. Sellés and M. Penrad (Institut Jacques Monod), and F.
467 Montel (Ecole Normale Supérieure de Lyon) for providing *Xenopus* nuclear pore
468 data, B. Jian (Institut Pasteur) for TOM22 antibodies, and C. Leterrier for fixation
469 protocols. We thank E. Rensen and C. Weber for help with experiments and
470 suggestions, B. Lelandais for help with PALM image processing, J-B. Arbona for
471 polymer simulations and J. Parmar for suggestions that led to the name ANNA-
472 PALM. We thank the IT service of Institut Pasteur, including J-B. Denis, N. Joly, and S.
473 Fournier, for access to the HPC cluster and relevant assistance, and T. Huynh for
474 help with GPU computing. This work was funded by Institut Pasteur, Agence

475 Nationale de la Recherche grant (ANR 14 CE10 0018 02), Fondation pour la
476 Recherche Médicale (Equipe FRM, DEQ 20150331762), and the Région Ile de France
477 (DIM Malinf). We also acknowledge Investissement d’Avenir grant ANR-16-CONV-
478 0005 for funding a GPU farm used in this work. A.A. and X.H. are recipients of
479 Pasteur-Roux fellowships from Institut Pasteur. W.O. is a scholar in the Pasteur -
480 Paris University (PPU) International PhD program.

481
482

483 **Author contributions**

484 W.O.: conceived method, developed ANNA-PALM software and web application,
485 performed experiments and analyses. A.A., M.L., X.H.: performed experiments. C.Z.:
486 conceived method, supervised project and wrote manuscript.

487
488

489 **Competing financial interests statement**

490 W.O. and C.Z. are listed as inventors on European patent application EP17306022
491 filed by Institut Pasteur.

492
493

494 **REFERENCES**

495

- 496 1. Betzig, E. *et al.* Imaging intracellular fluorescent proteins at nanometer
497 resolution. *Science (80-.)*. **313**, 1642–1645 (2006).
- 498 2. Rust, M. J., Bates, M. & Zhuang, X. Sub-diffraction-limit imaging by stochastic
499 optical reconstruction microscopy (STORM). *Nat Methods* **3**, 793–795 (2006).
- 500 3. Legant, W. R. *et al.* High-density three-dimensional localization microscopy
501 across large volumes. *Nat. Methods* **13**, 359–365 (2016).
- 502 4. Deschout, H. *et al.* Precisely and accurately localizing single emitters in
503 fluorescence microscopy. *Nat. Methods* **11**, 253–266 (2014).
- 504 5. Jones, S. A., Shim, S. H., He, J. & Zhuang, X. Fast, three-dimensional super-
505 resolution imaging of live cells. *Nat Methods* **8**, 499–505 (2011).
- 506 6. Huang, F. *et al.* Video-rate nanoscopy using sCMOS camera-specific single-
507 molecule localization algorithms. *Nat. Methods* **10**, 653–8 (2013).
- 508 7. Carlton, P. M. *et al.* Fast live simultaneous multiwavelength four-dimensional
509 optical microscopy. *Proc. Natl. Acad. Sci. U. S. A.* **107**, 16016–22 (2010).
- 510 8. Stelzer, E. H. K. Light-sheet fluorescence microscopy for quantitative biology.
511 *Nat. Methods* **12**, 23–26 (2014).
- 512 9. Huang, F., Schwartz, S. L., Byars, J. M. & Lidke, K. A. Simultaneous multiple-
513 emitter fitting for single molecule super-resolution imaging. *Biomed. Opt.*
514 *Express* **2**, 1377–93 (2011).
- 515 10. Burnette, D. T., Sengupta, P., Dai, Y., Lippincott-Schwartz, J. & Kachar, B.
516 Bleaching/blinking assisted localization microscopy for superresolution
517 imaging using standard fluorescent molecules. *Proc Natl Acad Sci U S A* **108**,
518 21081–21086 (2011).
- 519 11. Simonson, P. D., Rothenberg, E. & Selvin, P. R. Single-molecule-based super-
520 resolution images in the presence of multiple fluorophores. *Nano Lett* **11**,
521 5090–5096 (2011).
- 522 12. Zhu, L., Zhang, W., Elnatan, D. & Huang, B. Faster STORM using compressed
523 sensing. *Nat. Methods* **9**, 721–723 (2012).
- 524 13. Cox, S. *et al.* Bayesian localization microscopy reveals nanoscale podosome
525 dynamics. *Nat Methods* **9**, 195–200 (2012).
- 526 14. Ram, S., Ward, E. S. & Ober, R. J. Beyond Rayleigh’s criterion: A resolution
527 measure with application to single-molecule microscopy. *Proc. Natl. Acad. Sci.*
528 **103**, 4457–4462 (2006).
- 529 15. Deschout, H. *et al.* Precisely and accurately localizing single emitters in
530 fluorescence microscopy. *Nat. Methods* **11**, 253–266 (2014).
- 531 16. LeCun, Y., Bengio, Y. & Hinton, G. Deep learning. *Nature* **521**, 436–444 (2015).
- 532 17. Michael, E. *Sparse and Redundant Representations: From Theory to*
533 *Applications in Signal and Image Processing*. Springer (Springer Verlag, 2010).
- 534 18. Hinton, G. E. & Salakhutdinov, R. R. Reducing the Dimensionality of Data with
535 Neural Networks. *Science (80-.)*. **313**, (2006).
- 536 19. Schmidhuber, J. Deep learning in neural networks: An overview. *Neural*
537 *Networks* **61**, 85–117 (2014).
- 538 20. Sage, D. *et al.* Quantitative evaluation of software packages for single-molecule
539 localization microscopy. *Nat. Methods* **12**, 717–724 (2015).

- 540 21. Isola, P., Zhu, J.-Y., Zhou, T. & Efros, A. A. Image-to-Image Translation with
541 Conditional Adversarial Networks. <http://arxiv.org/abs/1611.07004> (2016).
- 542 22. Ronneberger, O., Fischer, P. & Brox, T. U-net: Convolutional networks for
543 biomedical image segmentation. in *Medical Image Computing and Computer-*
544 *Assisted Intervention – MICCAI 2015. Lecture Notes in Computer Science*, **9351**,
545 234–241 (Springer International Publishing, 2015).
- 546 23. Goodfellow, I. *et al.* Generative Adversarial Nets. *Adv. Neural Inf. Process. Syst.*
547 *27* 2672–2680 (2014). doi:10.1017/CBO9781139058452
- 548 24. Ciresan, D., Giusti Alessandro, Luca, G. & Schmidhuber, J. Mitosis Detection in
549 Breast Cancer Histology Images with Deep Neural Networks. *Med. Image*
550 *Comput. Comput. Interv. – MICCAI 2013* **8150**, (2013).
- 551 25. Wang, Z. W. Z. & Bovik, A. C. A. C. Mean squared error: Love it or leave it? A
552 new look at Signal Fidelity Measures. *IEEE Signal Process. Mag.* **26**, 98–117
553 (2009).
- 554 26. Zhao, H., Gallo, O., Frosio, I. & Kautz, J. Loss Functions for Image Restoration
555 with Neural Networks. *IEEE Trans. Comput. IMAGING* **3**, 47–57 (2017).
- 556 27. Culley, S. *et al.* NanoJ-SQUIRREL: quantitative mapping and minimisation of
557 super-resolution optical imaging artefacts. *bioRxiv* 158279 (2017).
558 doi:10.1101/158279
- 559 28. Srivastava, N., Hinton, G., Krizhevsky, A., Sutskever, I. & Salakhutdinov, R.
560 Dropout: A Simple Way to Prevent Neural Networks from Overfitting. *J. Mach.*
561 *Learn. Res.* **15**, (2014).
- 562 29. Arbona, J.-M., Herbert, S., Fabre, E. & Zimmer, C. Inferring the physical
563 properties of yeast chromatin through Bayesian analysis of whole nucleus
564 simulations. *Genome Biol.* **18**, 81 (2017).
- 565 30. Arnal, I. & Wade, R. H. How does taxol stabilize microtubules? *Curr. Biol.* **5**,
566 900–908 (1995).
- 567 31. Wu, S. *et al.* Microtubule motors regulate ISOC activation necessary to
568 increase endothelial cell permeability. *J. Biol. Chem.* **282**, 34801–8 (2007).
- 569 32. De Brabander, M., De May, J., Joniau, M. & Geuens, G. Ultrastructural
570 immunocytochemical distribution of tubulin in cultured cells treated with
571 microtubule inhibitors. *Cell Biol. Int. Rep.* **1**, 177–83 (1977).
- 572 33. Schnitzbauer, J., Strauss, M. T., Schlichthaerle, T., Schueder, F. & Jungmann, R.
573 Super-resolution microscopy with DNA-PAINT. *Nat. Protoc.* **12**, 1198–1228
574 (2017).
- 575 34. Löscherberger, A. *et al.* Super-resolution imaging visualizes the eightfold
576 symmetry of gp210 proteins around the nuclear pore complex and resolves
577 the central channel with nanometer resolution. *J. Cell Sci.* **125**, 570–5 (2012).
- 578 35. Szymborska, A. *et al.* Nuclear pore scaffold structure analyzed by super-
579 resolution microscopy and particle averaging. *Science* **341**, 655–8 (2013).
- 580 36. Sellés, J. *et al.* Nuclear pore complex plasticity during developmental process
581 as revealed by super-resolution microscopy. *Sci. Rep.* **7**, 14732 (2017).
- 582 37. Bellot, G. *et al.* TOM22, a core component of the mitochondria outer
583 membrane protein translocation pore, is a mitochondrial receptor for the
584 proapoptotic protein Bax. *Cell Death Differ.* **14**, 785–794 (2007).
- 585 38. Boettiger, A. N. *et al.* Super-resolution imaging reveals distinct chromatin

- 586 folding for different epigenetic states. *Nature* **529**, 418–422 (2016).
- 587 39. Zhang, Z., Nishimura, Y. & Kanchanawong, P. Extracting microtubule networks
588 from superresolution single-molecule localization microscopy data. *Mol. Biol.*
589 *Cell* **28**, 333–345 (2017).
- 590 40. Neumann, B. *et al.* Phenotypic profiling of the human genome by time-lapse
591 microscopy reveals cell division genes. *Nature* **464**, 721–727 (2010).
- 592 41. Beghin, A. *et al.* Localization-based super-resolution imaging meets high-
593 content screening. *Nat. Methods* **14**, 1184–1190 (2017).
- 594 42. Ouyang, W. & Zimmer, C. The imaging tsunami: Computational opportunities
595 and challenges. *Curr. Opin. Syst. Biol.* **4**, 105–113 (2017).
- 596 43. Chen, F., Tillberg, P. W. & Boyden, E. S. Expansion microscopy. *Science (80-.)*.
597 **347**, 543–548 (2015).
- 598 44. Chang, J.-B. *et al.* Iterative expansion microscopy. *Nat. Methods* (2017).
599 doi:10.1038/nmeth.4261
- 600 45. de Boer, P., Hoogenboom, J. P. & Giepmans, B. N. G. Correlated light and
601 electron microscopy: ultrastructure lights up! *Nat. Methods* **12**, 503–513
602 (2015).
- 603 46. Huang, B., Wang, W., Bates, M. & Zhuang, X. Three-dimensional super-
604 resolution imaging by stochastic optical reconstruction microscopy. *Science*
605 *(80-.)*. **319**, 810–813 (2008).
- 606 47. Bates, M., Huang, B., Dempsey, G. T. & Zhuang, X. Multicolor Super-Resolution
607 Imaging with Photo-Switchable Fluorescent Probes. *Science (80-.)*.
608 1146598v1 (2007).
- 609 48. Jungmann, R. *et al.* Multiplexed 3D cellular super-resolution imaging with
610 DNA-PAINT and Exchange-PAINT. *Nat. Methods* **11**, 313–318 (2014).
- 611 49. Shroff, H., Galbraith, C. G., Galbraith, J. A. & Betzig, E. Live-cell photoactivated
612 localization microscopy of nanoscale adhesion dynamics. *Nat Methods* **5**, 417–
613 423 (2008).
- 614 50. Kendall, A. & Gal, Y. What Uncertainties Do We Need in Bayesian Deep
615 Learning for Computer Vision? *Adv. Neural Inf. Process. Syst. 30 (NIPS 2017)*
616 *pre-proceedings* 5580–5590 (2017).
- 617

618 **FIGURE LEGENDS**

619

620 **FIGURE 1: Overview of ANNA-PALM**

621 ANNA-PALM consists of two main stages: **(a)** acquisition of training images using
622 standard localization microscopy (PALM) followed by artificial neural network
623 (ANN) training, and **(b)** reconstruction of super-resolution views and low resolution
624 error maps from new sparse PALM and/or widefield images (inference).

625 **(a)** Training images are obtained by acquiring one or a few long sequences, of
626 $K \sim 10^3 - 10^5$ diffraction limited, single molecule image frames, as in standard PALM
627 experiments; optionally, a widefield image W can also be acquired (top). The
628 acquisition time for each image sequence is $K\Delta t$, where Δt is the single frame
629 exposure time. Standard localization microscopy algorithms (grey 'localization'
630 boxes) are used to generate super-resolution images. For each experiment, a highly
631 sampled (dense) super-resolution image (PK) is generated using all (or in practice
632 $\geq 95\%$) available K frames. Sparse PALM images (P_k) from the same experiment are
633 obtained by using only $k \ll K$ frames. A switch (light blue) can be set to distinguish
634 different types of structures, e.g. nuclear pore complexes ('NPC'), mitochondria
635 ('Mito') or microtubules ('MT'). An ANN (labeled \mathcal{G} for 'generator', orange) is trained
636 by using the sparse PALM images P_k (plus an upsampled version L of the widefield
637 image W and the switch setting) as inputs and the corresponding dense PALM image
638 PK as target output. During training, the output of the generator \mathcal{G} (A_k) is compared
639 to the target image PK and the widefield image L (if available) via three loss, or error
640 functions (gray bordered boxes): (i) the 'super-resolution reconstruction error'

641 measures the difference between the reconstructed image A_k and the target PK
642 using a combination of the L1 norm and the MS-SSIM; (ii) the ‘low resolution
643 reconstruction error’ measures the MS-SSIM between the low resolution image WA
644 predicted from the reconstruction A_k and the low resolution image WP predicted
645 from the target image PK . Images WA and WP are predicted using a second ANN,
646 called low-resolution estimator (labeled Q , blue) that is trained to produce an
647 approximation of the actual widefield image W based on the MS-SSIM metric; (iii)
648 the ‘conditional GAN error’ uses a third ANN (labeled D for ‘discriminator’, red) that
649 attempts to distinguish between real dense PALM images PK and the generator’s
650 output A_k . The combined loss functions are iteratively optimized using stochastic
651 gradient descent. **(b)** A short sequence of diffraction limited single molecule images
652 (with $k \ll K$ frames, i.e. acquisition time $k\Delta t$), and an optional widefield image (W'),
653 are acquired. Standard localization algorithms generate a sparse (under-sampled)
654 PALM image ($P'k$). This sparse image $P'k$ (and the upscaled widefield image L' and
655 switch setting) are fed as inputs to the trained generator \mathcal{G} , which outputs a
656 reconstructed ANNA-PALM image ($A'k$). In addition, the low resolution estimator Q
657 predicts a low resolution image WA' , which can be compared to the input widefield
658 image W' via the MS-SSIM to produce a low resolution error map (top).

659

660 **FIGURE 2: Validation of ANNA-PALM on simulated images**

661 **(a)** Simulated widefield image of microtubules. **(b)** Simulated sparse PALM image of
662 microtubules with $n= 6,834$ localizations. **(c)** ANNA-PALM reconstruction using only
663 the widefield image **a** as input. **(d)** ANNA-PALM reconstruction using both the

664 widefield image **a** and the sparse PALM **b** image as inputs. **(e)** Simulated “perfect”
665 PALM image, equivalent to a PALM image with an infinite number of localizations
666 ($n=\infty$) and a resolution of 23 nm. This image was used to generate **a** (by convolution
667 with a Gaussian kernel approximating the microscope point spread function) and **b**
668 (by application of Poisson noise). **(f)** Merged image showing the perfect PALM image
669 **e** in green and the ANNA-PALM reconstruction **d** in red. Note that the ANNA-PALM
670 images **c,d** provide many high resolution details that are absent from the widefield
671 image **a** and the sparse PALM image **b** and that are in good (**c**) or very good (**d**)
672 agreement with the perfect PALM image **e**. Some reconstruction errors are
673 highlighted by arrows. Blue arrows in panel **c** point to errors of ANNA-PALM
674 reconstruction from the widefield image only, the white arrow in panel **d** points to
675 an error of ANNA-PALM reconstruction from both widefield and sparse PALM
676 images combined. Reconstruction errors diminish for larger numbers of
677 localizations, n (**Supplementary Figure 4**). **(g)** Reconstruction quality of PALM and
678 ANNA-PALM images, measured by the MS-SSIM with the perfect PALM image **e**, as
679 function of localization number n . Black curve: reconstruction quality of the
680 standard PALM images. Dashed blue curve: reconstruction quality of ANNA-PALM
681 using the sparse PALM images as input. Solid blue curve: reconstruction quality of
682 ANNA-PALM using both the sparse PALM and widefield images as inputs. Red
683 dashed line: reconstruction quality of ANNA-PALM using the widefield images as
684 input only. Dots are averages from 10 simulations; error bars show standard
685 deviations. The vertical dashed orange line indicates the minimum number of
686 localizations needed to achieve a resolution of $R_{5\times Nyq} = 23$ nm according to the five-

687 fold Nyquist criterion³. The dashed grey line indicates the minimum number of
688 localizations needed to achieve a double mean nearest neighbor distance less than
689 23 nm. ANNA-PALM reconstructions from sparse PALM images only (i.e. without
690 widefield images) achieve the same average MS-SSIM as standard PALM at the five-
691 fold Nyquist sampling limit with 26 times less localizations (blue double arrow).
692 ANNA-PALM reconstruction quality is highest when using both widefield and sparse
693 PALM images as inputs.

694

695 **FIGURE 3: ANNA-PALM imaging of microtubules**

696 ANNA-PALM reconstructions of a localization microscopy image of immunostained
697 microtubules. **(a)** Widefield image. **(b)** Sparse PALM image obtained from the first
698 9 s of acquisition ($k=300$ frames, $n=11,740$ localizations). **(c)** Dense PALM image
699 obtained from a 15 min long acquisition ($K=30,000$ frames, $N=409,364$
700 localizations). **(d)** ANNA-PALM reconstruction from the widefield image **a** only.
701 **(e)** ANNA-PALM reconstruction from the sparse PALM image **b** only. **(f)** ANNA-
702 PALM reconstruction from the widefield image **a** and sparse PLAM image **b**
703 combined. In panels **b-f**, pixel values are linearly mapped to colors from the look-up
704 table shown below. Black and white correspond to values V_{\min} and V_{\max} ,
705 respectively, with $V_{\min}=0$ for all panels, $V_{\max}=3, 24, 102, 102$ and 102 for panels **b, c,**
706 **d, e** and **f**, respectively. **(g-i)** Merged images comparing ANNA-PALM
707 reconstructions from panels **d-f** to the dense PALM image **c**. ANNA-PALM
708 reconstructions are shown in red, the dense PALM image in green. **(j)** Gradual
709 improvement of image quality for increasing acquisition time $k\Delta t$, shown for the

710 area highlighted in the insets of panels **a-i**. Top row: sparse PALM images. Middle
711 row: ANNA-PALM reconstructions from the sparse PALM images only (without
712 widefield). Bottom row: ANNA-PALM reconstructions from the widefield and sparse
713 PALM images combined. **Supplementary Video 1** shows the gradual increase in
714 quality of PALM and ANNA-PALM images with increased acquisition time for the
715 larger region of interest shown in panels **a-i**.

716

717 **FIGURE 4: High-throughput imaging with ANNA-PALM**

718 Application of ANNA-PALM to high-throughput imaging of a 1.8 mm x 1.8 mm area
719 containing more than 1,000 cells. **(a)** Sparse PALM image of this area, constructed
720 by assembling a mosaic of $33 \times 33 = 1,089$ sparse PALM images of individual fields of
721 view, obtained from $k=1,000$ raw frames each (with $\Delta t=10$ ms exposure time per
722 frame, i.e. in $k\Delta t=10$ s). Total image acquisition time was $1,089 \times 10$ s, i.e. ~ 3.1 hours.
723 The sparsity of the image is not apparent at this large scale. **(b)** ANNA-PALM
724 reconstruction of the image in **a**, obtained by assembling a mosaic of 1,089
725 individual reconstructions (one per field of view). **(c)** Magnified view of the green
726 boxed region in **a**. The inset shows a further magnified view of the yellow boxed
727 region, highlighting the sparsity of the image. **(d)** Same as **c**, but for the ANNA-PALM
728 reconstruction. A line profile across a microtubule is shown, with a $\text{FWHM} \approx 51$ nm.
729 Non-linear contrast adjustment was applied manually for panels **a** and **b**, with black
730 corresponding to values of zero in both panels. In panels **c** and **d**, pixel values were
731 linearly mapped to colors from the look-up table in **Figure 3**; Black and white
732 correspond to values V_{\min} and V_{\max} , respectively, with $V_{\min}=0$ for all panels, and

733 $V_{\max}=3$ and 51 for panels **c** and **d**, respectively. See also **Supplementary Video 2** for
734 an animated 'zoom-in' highlighting the spatial scales covered by the assembled
735 image. See also **Supplementary Figure 12** for ANNA-PALM reconstructions of the
736 same area from the widefield images only.

737

738 **FIGURE 5: Robustness of ANNA-PALM to experimental perturbations**

739 This figure shows ANNA-PALM reconstructions using an ANN trained on PALM
740 images of microtubules in untreated cells and applied without retraining to sparse
741 localization images of microtubules in different experimental conditions: untreated
742 control cells (**a-c**); cells treated with 1 μM of Taxol (**d-f**); cells treated with 1 μM of
743 Nocodazole (**g-i**); untreated cells imaged with DNA-PAINT (**j-l**). (**a,d,g,j**) Sparse
744 localization images obtained from the first k frames of the acquired image sequence,
745 with $k=500, 800, 300,$ and 400 for **a, d, g,** and **j**, respectively. (**b,e,h,k**) ANNA-PALM
746 reconstructions using the sparse localization images immediately to the left as
747 input. (**c,f,i,l**) Dense localization images obtained from $K=60,000$ frames. Pixel
748 values are linearly mapped to colors from the look-up table in **Figure 3**. Black and
749 white correspond to values V_{\min} and V_{\max} , respectively, with $V_{\min}=0$ for all panels,
750 and $V_{\max}=10, 120, 90, 25, 150, 40, 18, 150, 50, 18, 120,$ and 200 for panels **a, b, c, d,**
751 **e, f, g, h, i, j, k,** and **l**, respectively.

752

753 **FIGURE 6: ANNA-PALM reconstructions of nuclear pores and mitochondria**

754 PALM and ANNA-PALM images of nuclear pores (**a-c**) and mitochondria (**d-f**).
755 (**a**) Sparse PALM image of the immunolabeled *Xenopus* nucleoporin gp210 obtained

756 from the first $k=3,000$ frames. Note that individual nuclear pores are hard to
757 identify. **(b)** ANNA-PALM reconstruction of image **a**. **(c)** Dense PALM image obtained
758 from all $K=30,000$ frames. **(d)** Sparse PALM image of the immunolabeled
759 mitochondrial outer membrane protein TOM22, obtained from the first $k=400$
760 frames. **(e)** ANNA-PALM reconstruction of image **d**. **(f)** Dense PALM image obtained
761 from all $K=30,000$ frames. Pixel values are linearly mapped to colors from the look-
762 up table shown in **Figure 3**. Black and white correspond to values V_{\min} and V_{\max} ,
763 respectively, with $V_{\min}=0$ for all panels, and $V_{\max}=3, 51, 3, 3, 128,$ and 18 for panels **a**,
764 **b, c, d, e,** and **f**, respectively

765 **ONLINE METHODS**

766

767 **Artificial neural network**

768 Our ANN, called ‘A-net’, is based on the pix2pix architecture²¹, which is a special
769 conditional generative adversarial network (cGAN)²³ for image to image
770 “translation”, i.e. mapping from one type of image to another. The A-net consists of
771 three distinct neural networks: (i) a generator network \mathcal{G} that produces the
772 reconstructed super-resolution image, (ii) a network Q called ‘low resolution
773 estimator’ that produces the low resolution error map, (iii) a cGAN discriminator
774 network D that provides the adversarial loss (**Figure 1a**). The generator network \mathcal{G}
775 builds on the U-net architecture, and consists of an encoder-decoder network with
776 skip connections²² and 16 convolutional layers. Its inputs and outputs are image
777 patches containing $(256m) \times (256m)$ pixels, where m is an integer (we used $m=1$ or 2
778 but this can be adjusted for different sizes of CPU/GPU memory or input images).
779 The input is a sparse PALM image, a widefield image upscaled to the same size (see
780 below), and a computational switch number that allows the network to switch
781 between different types of image structures (e.g. nuclear pores or microtubules).
782 The switch setting is encoded numerically and coupled by convolutional operations
783 into the A-net encoder. The output of the generator \mathcal{G} is a reconstructed image
784 (called ANNA-PALM reconstruction or ANNA-PALM image elsewhere) of the same
785 size as the input images. The low resolution estimator Q has four convolutional
786 layers. It takes the $(256m) \times (256m)$ dense PALM image patch or the ANNA-PALM
787 image patch as input and outputs a low resolution image with $(64m) \times (64m)$ pixels.

788 The cGAN discriminator network D has five convolutional layers. Its inputs are three
789 $(256m) \times (256m)$ pixel image patches (the sparse PALM image, the widefield image,
790 and either the ANNA-PALM reconstruction or the corresponding dense PALM
791 image), plus the upscaled widefield image, and its output is a $(30m) \times (30m)$ image
792 whose pixel values indicate whether the corresponding input patch is real (i.e. an
793 experimentally obtained conventional PALM image) or produced by the generator \mathcal{G} .
794 All convolutional layers are followed by batch normalization⁵¹. Dropout layers²⁸
795 (with dropout probability $p=0.5$) are introduced in the central layers of the A-net
796 generator and turned on during training, but switched off during inference.
797 Activation functions are rectified linear units (ReLU) $x \rightarrow \sup(x, 0)$ or “leaky” ReLUs
798 $x \rightarrow \sup(x, 0) + \inf(\epsilon x, 0)$ with $\epsilon = 0.2$ ⁵², except for the last layer of \mathcal{G} , which uses the
799 hyperbolic tangent $x \rightarrow \tanh(x)$ and the last layer of Q , which uses a sigmoid
800 function $x \rightarrow (1 + \exp(-x))^{-1}$. The A-net architecture is fully described in
801 **Supplementary Note 1 and Supplementary Tables 1-4.**

802

803 **Training objectives and error map**

804 Each of the three networks mentioned above (\mathcal{G} , Q , and D) is associated to a distinct
805 objective function - also called loss- and hereafter noted $\mathcal{L}_{\mathcal{G}}$, \mathcal{L}_Q , and \mathcal{L}_D respectively.
806 These loss functions are specified in detail below. In the following equations, for
807 notational simplicity, we designate the sparse input image as \mathbf{S} , the low resolution
808 (widefield) input image as \mathbf{W} , the corresponding dense PALM image (i.e. the target)
809 as \mathbf{T} , and the A-net’s output as $\mathbf{A} = \mathcal{G}(\mathbf{S}, \mathbf{W})$ (in **Figure 1a**, images \mathbf{S} , \mathbf{T} and \mathbf{A} are
810 labeled Pk, PK and Ak, respectively); the computational switch indicating the image

811 type is noted \mathbf{M} . Low resolution images produced by the low resolution estimator
 812 network Q from \mathbf{A} and \mathbf{T} are designated as $\mathbf{W}_A = Q(\mathbf{A})$ and $\mathbf{W}_T = Q(\mathbf{T})$,
 813 respectively.

814 The generator loss function \mathcal{L}_G is the sum of three terms. The first term of \mathcal{L}_G
 815 is the super-resolution reconstruction error, hereafter called $\mathcal{L}_{\text{SuperRes}}(\mathcal{G})$. This term
 816 penalizes the difference between the generator output \mathbf{A} and the target image \mathbf{T} .
 817 Based on a recent analysis of loss functions for image restoration with neural
 818 networks²⁶, we defined this difference as a weighted average of two quantities:
 819 (i) the multi-scale structural similarity index (MS-SSIM) between \mathbf{A} and \mathbf{T} and (ii) a
 820 modification of the L1 norm, where the absolute difference between \mathbf{A} and \mathbf{T} is
 821 smoothed by a Gaussian kernel:

$$\begin{aligned} \mathcal{L}_{\text{SuperRes}}(\mathcal{G}) &= \mathbb{E}_{(\mathbf{S}, \mathbf{T}, \mathbf{W}, \mathbf{M}) \sim p_{\text{data}}(\mathbf{S}, \mathbf{T}, \mathbf{W}, \mathbf{M})} [\rho (1 - MS_SSIM(\mathbf{A}, \mathbf{T})) + (1 \\ &\quad - \rho) \langle G_\sigma * |\mathbf{A} - \mathbf{T}| \rangle] \\ &= \mathbb{E}_{(\mathbf{S}, \mathbf{T}, \mathbf{W}, \mathbf{M}) \sim p_{\text{data}}(\mathbf{S}, \mathbf{T}, \mathbf{W}, \mathbf{M})} [\rho (1 - MS_SSIM(\mathcal{G}(\mathbf{S}, \mathbf{W}, \mathbf{M}), \mathbf{T})) + (1 \\ &\quad - \rho) \langle G_\sigma * |\mathcal{G}(\mathbf{S}, \mathbf{W}, \mathbf{M}) - \mathbf{T}| \rangle] \end{aligned}$$

822 where \mathbb{E} denotes expectation; $p_{\text{data}}(\mathbf{S}, \mathbf{T}, \mathbf{W}, \mathbf{M})$ is the joint probability density of the
 823 sparse PALM images \mathbf{S} , dense PALM images \mathbf{T} , widefield images \mathbf{W} and switch
 824 settings \mathbf{M} from the training data set; $MS_SSIM(\mathbf{A}, \mathbf{T})$ is the multi-scale structural
 825 similarity index between \mathbf{A} and \mathbf{T} ; G_σ is a Gaussian smoothing kernel; $*$ denotes
 826 convolution; $|\mathbf{A} - \mathbf{T}|$ is the absolute difference image (i.e. pixel (i,j) has value
 827 $|\mathbf{A}(i, j) - \mathbf{T}(i, j)|$ and $\rho \in [0, 1]$ is a scalar weight that balances the relative
 828 contributions of MS-SSIM and the modified L1 norm and is set to $\rho = 0.84$ as in ref.
 829 ²⁶.

830 The second term of $\mathcal{L}_{\mathcal{G}}$ is called $\mathcal{L}_{\text{LowRes}}(\mathcal{G}, Q)$ and measures the consistency
 831 between the low resolution images \mathbf{W}_A and \mathbf{W}_T predicted by the low resolution
 832 estimator network Q :

$$\begin{aligned}\mathcal{L}_{\text{LowRes}}(\mathcal{G}, Q) &= \mathbb{E}_{(\mathbf{S}, \mathbf{T}, \mathbf{W}, \mathbf{M}) \sim p_{\text{data}}(\mathbf{S}, \mathbf{T}, \mathbf{W}, \mathbf{M})} [1 - MS_SSIM(\mathbf{W}_A, \mathbf{W}_T)] \\ &= \mathbb{E}_{(\mathbf{S}, \mathbf{T}, \mathbf{W}, \mathbf{M}) \sim p_{\text{data}}(\mathbf{S}, \mathbf{T}, \mathbf{W}, \mathbf{M})} [1 - MS_SSIM(Q(\mathcal{G}(\mathbf{S}, \mathbf{W}, \mathbf{M})), Q(\mathbf{T}))]\end{aligned}$$

833 Alternatively, in the above objective function, \mathbf{W}_T can be replaced by the actually
 834 observed widefield image \mathbf{W} , although with our data this led to slightly lower
 835 reconstruction quality. The low resolution estimator network Q is trained
 836 simultaneously with the generator \mathcal{G} to produce a low resolution image from the
 837 dense PALM image \mathbf{T} that is consistent with the observed low resolution image \mathbf{W} .
 838 This training is done based on the following objective function:

$$\mathcal{L}_Q(Q) = \mathbb{E}_{(\mathbf{T}, \mathbf{W}) \sim p_{\text{data}}(\mathbf{T}, \mathbf{W})} [1 - MS_SSIM(Q(\mathbf{T}), \mathbf{W})]$$

839 Note that the reconstructed low resolution image $Q(\mathbf{T})$ is four times smaller than
 840 the dense PALM image \mathbf{T} , as described in **Supplementary Note 1**. Because the input
 841 widefield image \mathbf{W} can have a different size, we use bilinear interpolation to resize
 842 \mathbf{W} to the same size as $Q(\mathbf{T})$. (If needed, a scaling factor different from four can be
 843 obtained by adding or removing downsample layers in network Q). At inference, the
 844 low resolution estimator Q is also used to produce the error map, as shown in
 845 **Figure 1b**, and **Supplementary Figures 6, 11, 15**. This error map is defined as:

$$E_Q(\mathbf{A}, \mathbf{W}) = (1 - MS_SSIM(Q(\mathbf{A}), \mathbf{W}))(Q(\mathbf{A}) + \mathbf{W})$$

846 High (respectively low) values of the error map indicate large (respectively small)
 847 inconsistencies, between the reconstructed super-resolution image \mathbf{A} and the
 848 observed widefield image \mathbf{W} .

849 The third term of $\mathcal{L}_{\mathcal{G}}$ draws from recent work on generative adversarial
850 networks (GAN)^{21,23,53} and is noted $\mathcal{L}_{\text{cGAN}}(\mathcal{G}, \mathcal{D})$. In a GAN, a generator network \mathcal{G}
851 learns to transform random input vectors \mathbf{z} (drawn from a probability density
852 $p_{\mathbf{z}}(\mathbf{z})$) into new samples of a data probability density $p_{\text{data}}(\mathbf{x})$. In our case, the data
853 samples \mathbf{x} are the dense PALM images \mathbf{T} . The generator \mathcal{G} learns by working against
854 a discriminator network \mathcal{D} that simultaneously learns to discriminate between
855 original data samples and samples generated by \mathcal{G} . Adversarial training thus
856 consists in playing a minmax game such that $(\mathcal{G}^*, \mathcal{D}^*) = \arg \min_{\mathcal{G}} \max_{\mathcal{D}} \mathcal{L}_{\text{GAN}}(\mathcal{G}, \mathcal{D})$,
857 with an objective function of the form²³: $\mathcal{L}_{\text{GAN}}(\mathcal{G}, \mathcal{D}) = \mathbb{E}_{\mathbf{x} \sim p_{\text{data}}(\mathbf{x})} [\log \mathcal{D}(\mathbf{x})] +$
858 $\mathbb{E}_{\mathbf{z} \sim p_{\mathbf{z}}(\mathbf{z})} \log[1 - \mathcal{D}(\mathcal{G}(\mathbf{z}))]$, or equivalently by simultaneous optimization of two
859 coupled loss functions:

$$\begin{cases} \mathcal{D}^* = \arg \max_{\mathcal{D}} (\mathbb{E}_{\mathbf{x} \sim p_{\text{data}}(\mathbf{x})} [\log \mathcal{D}(\mathbf{x})] + \mathbb{E}_{\mathbf{z} \sim p_{\mathbf{z}}(\mathbf{z})} \log[1 - \mathcal{D}(\mathcal{G}(\mathbf{z}))]) \\ \mathcal{G}^* = \arg \min_{\mathcal{G}} (\mathbb{E}_{\mathbf{z} \sim p_{\mathbf{z}}(\mathbf{z})} \log[1 - \mathcal{D}(\mathcal{G}(\mathbf{z}))]) \end{cases}$$

860 In a conditional GAN (cGAN), the generator and the discriminator have an extra
861 input vector \mathbf{c} and the first objective function above becomes: $\mathcal{L}_{\mathcal{D}}(\mathcal{G}, \mathcal{D}) =$
862 $\mathbb{E}_{(\mathbf{c}, \mathbf{x}) \sim p_{\text{data}}(\mathbf{c}, \mathbf{x})} [\log \mathcal{D}(\mathbf{c}, \mathbf{x})] + \mathbb{E}_{\mathbf{c} \sim p_{\text{data}}(\mathbf{c}), \mathbf{z} \sim p_{\mathbf{z}}(\mathbf{z})} \log[1 - \mathcal{D}(\mathbf{c}, \mathcal{G}(\mathbf{c}, \mathbf{z}))]$, such that the
863 generator learns a conditional probability density $p_{\text{data}}(\mathbf{x}|\mathbf{c})$; and the second
864 objective function likewise becomes $\mathcal{L}_{\text{cGAN}}(\mathcal{G}, \mathcal{D}) = \mathbb{E}_{\mathbf{c} \sim p_{\text{data}}(\mathbf{c}), \mathbf{z} \sim p_{\mathbf{z}}(\mathbf{z})} \log[1 -$
865 $\mathcal{D}(\mathcal{G}(\mathbf{z}))]$. In our A-net, we replaced the logarithmic losses above by least square
866 losses⁵³, as they empirically yielded better results. Thus, we used the objective
867 functions:

868 $\mathcal{L}_{\mathcal{D}}(\mathcal{G}, \mathcal{D}) = \mathbb{E}_{(\mathbf{c}, \mathbf{x}) \sim p_{\text{data}}(\mathbf{c}, \mathbf{x})} (\mathcal{D}(\mathbf{c}, \mathbf{x}) - 1)^2 + \mathbb{E}_{\mathbf{c} \sim p_{\text{data}}(\mathbf{c}), \mathbf{z} \sim p_{\mathbf{z}}(\mathbf{z})} [\mathcal{D}(\mathbf{c}, \mathcal{G}(\mathbf{c}, \mathbf{z}))]^2$ and

869 $\mathcal{L}_{\text{cGAN}}(\mathcal{G}, \mathcal{D}) = \mathbb{E}_{\mathbf{c} \sim p_{\text{data}}(\mathbf{c}), \mathbf{z} \sim p_{\mathbf{z}}(\mathbf{z})} [1 - \mathcal{D}(\mathbf{c}, \mathcal{G}(\mathbf{c}, \mathbf{z}))]^2$. In our case, the input \mathbf{c} is the
870 sparse PALM image \mathbf{S} combined with the upsampled version $\mathbf{L} = \mathcal{B}(\mathbf{W})$ of the
871 widefield image \mathbf{W} , where \mathcal{B} denotes bilinear interpolation. Note that in practice the
872 noise \mathbf{z} in our ANN was introduced only through the use of dropout layers, as in the
873 pix2pix implementation²¹. Thus, the objective functions are:

$$\begin{aligned} \mathcal{L}_{\mathcal{D}}(\mathcal{D}) = & \mathbb{E}_{\mathbf{S}, \mathbf{T}, \mathbf{W}, \mathbf{M} \sim p_{\text{data}}(\mathbf{S}, \mathbf{T}, \mathbf{W}, \mathbf{M})} (\mathcal{D}(\mathcal{B}(\mathbf{W}), \mathbf{S}, \mathbf{T}) - 1)^2 \\ & + \mathbb{E}_{\mathbf{z} \sim p_{\mathbf{z}}(\mathbf{z}), \mathbf{S} \sim p_{\text{data}}(\mathbf{S})} (\mathcal{D}(\mathcal{B}(\mathbf{W}), \mathbf{S}, \mathcal{G}(\mathbf{S}, \mathbf{W}, \mathbf{M})))^2 \end{aligned}$$

874 and:

$$\mathcal{L}_{\text{cGAN}}(\mathcal{G}, \mathcal{D}) = \mathbb{E}_{(\mathbf{S}, \mathbf{T}, \mathbf{W}, \mathbf{M}) \sim p_{\text{data}}(\mathbf{S}, \mathbf{T}, \mathbf{W}, \mathbf{M})} (\mathcal{D}(\mathcal{B}(\mathbf{W}), \mathbf{S}, \mathcal{G}(\mathbf{S}, \mathbf{W}, \mathbf{M})) - 1)^2$$

875 In the end, combining the three loss terms described above, we implemented
876 the following optimization problem :

$$\begin{cases} Q^* = \arg \min_Q \mathcal{L}_Q(Q) \\ D^* = \arg \max_D \mathcal{L}_D(D) \\ G^* = \arg \min_G [\alpha \mathcal{L}_{\text{SuperRes}}(G) + \beta \mathcal{L}_{\text{LowRes}}(G, Q) + \gamma \mathcal{L}_{\text{cGAN}}(G, D)] \end{cases}$$

877 The weights α , β and γ are hyperparameters, which we set manually to $\alpha = 50$,
878 $\beta = 25$ and $\gamma = 1$ for most experiments. In absence of widefield images \mathbf{W} , β was
879 simply set to zero. The reported results are not very sensitive to these parameters.

880 We trained the A-net end-to-end using stochastic gradient descent (SGD)
881 with Adam⁵⁴ and a batch size of 1 with 200,000 or more iterations (backpropagation
882 steps). Our implementation was adapted from `affinelay`'s TensorFlow⁵⁵
883 implementation, which is ported from the Torch implementation of pix2pix²¹. Both
884 network training and inference were performed on Tesla P100, Tesla M40, Tesla

885 K80 or GTX TitanXP graphical processing units (GPUs) from Nvidia. A-net training
886 from scratch typically takes from hours to days on a single GPU. Once trained, the A-
887 net takes only ~ 1 second or less to reconstruct a super-resolution image of
888 2560×2560 pixels (corresponding to an entire FoV). Training time could be further
889 reduced by pretraining (or transfer learning), use of GPU clusters, or optimized data
890 augmentation.

891

892 **Experimental training images and data augmentation**

893 Experimental training data are obtained from standard localization microscopy data
894 (dense PALM images). To achieve good performance, ANNs generally necessitate
895 large amounts of training data. However, ANNA-PALM typically requires PALM
896 images from no more than 10 FoVs (of $55 \mu\text{m} \times 55 \mu\text{m}$ each) and can even be trained
897 with a single FoV. This is possible thanks to an extensive on-the-fly data
898 augmentation strategy, as described below. Each of the dense PALM training images
899 corresponds to a list of localizations $(f_i, x_i, y_i)_{i=1..n}$, where $f_i \in [1, K]$ is the index of
900 the diffraction limited frame from which localization x_i, y_i originates, and K is the
901 total frame number. PALM images are obtained as plain 2D histograms of these
902 localizations with typical pixel sizes of 10-20 nm. From each list of localizations
903 (corresponding to a dense PALM image of a single FoV), we generate 10-30 pairs of
904 input and target images (S, T) for training. To define the target image T , we take a
905 random consecutive subset $[k_T, k_T + 0.95K]$ of 95% of all available K frames (k_T is
906 chosen randomly between 0 and $0.05K$) and create the 2D histogram image based
907 on localizations from those frames only, i.e. from all (x_j, y_j) such that $f_j \in$

908 $[k_T, k_T + 0.95K]$. To define the sparse input image \mathbf{S} , we take random subsets of
909 300-500 consecutive frames from the first half of the image sequence and similarly
910 create a 2D histogram of the localizations from those frames only. When a widefield
911 image \mathbf{W} is available, this image must first be aligned with the corresponding dense
912 PALM image \mathbf{T} . This is done using an FFT-based phase correlation algorithm⁵⁶ after
913 histogram equalization of image \mathbf{T} , smoothing by convolution with a Gaussian
914 Kernel of standard deviation 6 pixels, and resizing with bilinear interpolation to the
915 same size as image \mathbf{W} . The registered widefield image \mathbf{W} is then scaled up using
916 bilinear interpolation to an image $\mathbf{L} = \mathcal{B}(\mathbf{W})$ with the same size as image \mathbf{T} .

917 During training, for each iteration of SGD, we crop the images \mathbf{S} , \mathbf{L} and \mathbf{T} with
918 a randomly placed 712x712 pixel sized region $\mathcal{R} = [x_{\min}, x_{\min} + 712] \times$
919 $[y_{\min}, y_{\min} + 712]$. We then use random geometric transformations and apply them
920 identically to the three images. Specifically, we rotate the images by a random angle
921 between 0 and 360 degrees, apply elastic transformations⁵⁷, and then crop the
922 center region of size 512x512 pixels. In addition to geometric transformations, we
923 also introduce realistic noise from experimental background images. This is done by
924 manually outlining regions of background in selected PALM training images,
925 splitting these regions into small patches of 40x40 pixels, grouping them according
926 to their summed pixel values, then assembling them into a larger image with the
927 same size as \mathbf{T} . During training, these semi-synthetic noise images are randomly
928 selected and added to the input image \mathbf{S} without altering \mathbf{T} or \mathbf{W} . Finally, we
929 normalize the input image \mathbf{S} by subtracting its mean and dividing by standard
930 deviation. If a widefield image \mathbf{W} is provided, its pixel values are scaled to a

931 minimum of 0 and a maximum of 1. Otherwise, \mathbf{W} is replaced by an image containing
932 zeros only. The target image \mathbf{T} is truncated at a maximum value of 255 and then
933 scaled to have a minimum of 0 and a maximum of 1. For the switch \mathbf{M} , we used an
934 integer number to define the type of training images, e.g. 0 for microtubules, 1 for
935 nucleoporins, 2 for mitochondria. When training on different types of images, e.g.
936 microtubules and nucleoporins (**Supplementary Figure 13**), we assign the
937 corresponding switch value to \mathbf{M} and use it as additional input to the A-net together
938 with images \mathbf{S} and \mathbf{W} , as described in **Supplementary Note 1**.

939

940 **Image simulations**

941 Our procedure to simulate localization microscopy (PALM) images of microtubules
942 is illustrated in **Supplementary Figure 1**. To simulate microtubule filaments, we
943 used a Langevin dynamics simulation²⁹ that generates random configurations of
944 semiflexible curves with a specified rigidity (persistence length), starting from a
945 random initial configuration (**Supplementary Figure 1a,b**). The initial
946 configurations were generated with a Python library named cpolymer and the
947 Langevin dynamics was implemented using the molecular dynamics code
948 LAMMPS⁵⁸. Although the simulation generates 3D polymer chains, we only
949 considered their 2D projections, consisting of N_p connected positions $(x_k, y_k)_{k=1..N_p}$.
950 To obtain smooth filaments we further interpolated these connected segments using
951 spline functions with the Scipy function `scipy.interpolate.splev`. Next, we turned
952 these 2D curves into a grey scale image of 800x800 pixels, with an assumed pixel
953 size of 7.8 nm, using the Python library Matplotlib. This image was further

954 convolved with a Gaussian kernel of standard deviation 1.5 pixels, resulting in a
955 smooth image $I(i, j)$ as shown in **Supplementary Figure 1c**, and normalized to a
956 probability density ($\sum \sum_{i,j} I(i, j) = 1$, with all $I(i, j) \geq 0$). This image was used to
957 mimic a “perfect” PALM image of filaments corresponding to an infinite number of
958 localizations ($n = \infty$). Such perfect images were used as targets during ANN
959 training for simulated data and defined as ground truth for the quantification of
960 reconstruction quality by MS-SSIM (**Figure 2g**). During training, we applied the
961 same rotations and elastic transformations described for experimental data in the
962 previous section.

963 Localization microscopy images obtained from a finite number of
964 localizations $n < \infty$ (sparse PALM images \mathcal{S}), can be considered as a sampling of the
965 probability density $I(i, j)$ with n samples. These images can therefore be simulated
966 by applying Poisson noise to a rescaled version of the perfect PALM image, i.e.:
967 $\mathcal{S}(\lambda, I) = \mathcal{P}(\lambda I / I_{\max})$, where I_{\max} is the maximum value of I , $\mathcal{P}(\mu)$ denotes the
968 Poisson probability distribution of mean μ and where the peak parameter λ controls
969 the level of sampling. In order to simulate sparse PALM images for various levels of
970 sampling, we varied the peak value λ following a log-normal distribution where
971 $\ln(\lambda)$ has mean -0.5 and standard deviation 0.001 and applied Poisson noise using
972 the numpy library function `random.poisson`. An example of a simulated sparse
973 PALM image is shown in **Supplementary Figure 1d**. Besides finite sampling,
974 localization microscopy images are corrupted by additional noise sources such as
975 false detections from background noise due to out-of-focus light or unspecific
976 binding of antibodies. To mimic this, we first created a probability density

977 $I_b = I * G_{\sigma_b}$ for the background noise by convolving I with a Gaussian kernel G_{σ_b} of
978 large standard deviation $\sigma_b=25$ pixels, and applied Poisson noise with $\lambda = 0.06$. To
979 create training images, we added this background noise image to the sparse PALM
980 image S above (**Supplementary Figure 2**). We did not add background noise to the
981 test images used during inference (**Figure 2**). To simulate the widefield images
982 (**Figure 2a**), we first blurred the perfect PALM image by convolution with a
983 Gaussian kernel of standard deviation 8 pixels, then added Gaussian noise with zero
984 mean and standard deviation chosen randomly between 0.5 and 1.5.

985 For simulations of nuclear pore images (**Supplementary Figure 15**), we
986 applied a similar procedure, except that the perfect PALM images were obtained by
987 randomly distributing circles of diameter 150 nm in the plane (avoiding overlaps)
988 and placing eight Gaussian spots (of standard deviation 1.7 pixels) at equal distance
989 from each other on each circle to mimic the octogonal shape of nuclear pores.

990

991 **Sample preparation**

992 For microtubule imaging experiments (**Figures 3-5** and **Supplementary Figures 8-**
993 **10**), except those using DNA-PAINT (**Figure 5j,l**), U-373 MG (Uppsala) cells were
994 cultured in Dulbecco's Modified Eagle Medium: Nutrient Mixture F-12 (DMEM/F12;
995 Gibco) supplemented with 10% (v/v) fetal bovine serum (FBS; Gibco), 1% (v/v)
996 penicillin-streptomycin (Gibco), in a 5% CO₂ environment at 37°C on 18-mm
997 cleaned coverslips in 12-well plates. 24 hours after plating, cells were pre-extracted
998 for 10 s in 0.25% (v/v) Triton X-100 (Triton) in BRB80 (80 mM PIPES, 1 mM MgCl₂,
999 1 mM EGTA, adjusted to pH 6.8 with KOH) supplemented with 4 mM EGTA, and

1000 immediately fixed for 10 min with 0.25% (v/v) Triton + 0.5% Glutaraldehyde in
1001 BRB80, followed by reduction for 7 min with 0.1% NaBH₄ solution in PBS and
1002 another washing step in PBS. Cells were directly incubated for 1h at room
1003 temperature in PBS with 1:500 rat alpha-tubulin antibodies (Bio-Rad MCA77G),
1004 followed by 3 washing steps with PBS, and then incubated for 45min in PBS with
1005 1:500 anti-rat Alexa-647 conjugated secondary antibodies from donkey (Jackson
1006 ImmunoResearch Laboratories, ref. 712-605-153).

1007 For the DNA-PAINT experiment on microtubules (**Figure 5k-m**), U-373 cells
1008 stuck on 18 mm diameter coverslips were fixed at 37°C with 4% PFA in PHEM
1009 buffer and permeabilized in 0.2% glutaldehyde. Next, cells were incubated for 1 h
1010 with 1:500 primary mouse antibodies against alpha-tubulin. The sample was
1011 washed 3 times in PBS, then incubated with 1:100 anti-mouse oligo-conjugated
1012 antibodies from Ultivue Kit 2 for DNA-PAINT imaging³³. After washing the sample 3
1013 times in PBS, and just before imaging, 2nM of complementary oligos coupled to Cy3
1014 fluorophores were added to the sample.

1015 Nuclear pore imaging data of gp210 and WGA (**Figure 6a-c** and
1016 **Supplementary Figure 14**) were kindly provided by J. Sellés and O. Falklaris and
1017 obtained from nuclear membranes of *Xenopus* frog eggs prepared as described
1018 previously³⁶.

1019 For mitochondria imaging experiments (**Figure 6e-f**), COS7 cells were
1020 cultured under the same conditions as U-373 cells above using phenol-red free
1021 DMEM medium and fixed with 4% PFA in PBS for 10 min. The sample was blocked
1022 with 3% BSA in PBS for 20 min and immunostained with 1:500 mouse antibodies

1023 against TOM22 (Sigma, ref. T6319) in wash buffer (PBS with 0.5% BSA) for 1 h.
1024 After extensive washing with wash buffer, the sample was incubated with 1:500
1025 anti-mouse secondary antibodies from donkey conjugated to Alexa-647 dyes
1026 (Jackson ImmunoResearch Laboratories, ref. 715-605-151) in wash buffer for 30
1027 min. After washing 5 times with wash buffer and 2 times with PBS, samples were
1028 post-fixed with 2% PFA in PBS for 10 min and washed 5 times with PBS.

1029 For all localization microscopy experiments except DNA-PAINT, we used a
1030 photoswitching buffer⁵⁹ composed of 50 mM Tris-HCl + 10 mM NaCl + 10% (w/v)
1031 glucose + 168 AU/mL Glucose-Oxidase + 1404 AU/mL Catalase + 1% 2-
1032 Mercaptoethanol. For microtubule imaging experiments, we used this buffer to fill a
1033 square hole that was manually cut in a parafilm sheet, which was deposited on a
1034 rectangular coverglass. The round coverslips were sealed with nail polish.

1035

1036 **Image acquisition in localization and high-throughput microscopy**

1037 We performed single molecule localization microscopy experiments (PALM/STORM
1038 and DNA-PAINT) on custom built microscopy systems, as previously described⁵⁹⁻⁶¹.
1039 The system used for PALM/STORM imaging of microtubules is based on an inverted
1040 microscope body (Nikon Ti Eclipse) equipped with a either a 60x 1.49 NA oil
1041 immersion objective (Nikon) or a 60x 1.2 NA water immersion objective (Nikon)
1042 and with the Perfect Focus System active. A 642 nm wavelength laser with 500 mW
1043 power was used to excite Alexa-647 fluorophores and an AOTF (AA optics) was used
1044 to modulate laser excitation. Sequences of diffraction limited single molecule image
1045 frames were acquired either on a sCMOS camera (Hamamatsu ORCA-Flash4.0),

1046 which can capture images of 2,042x2,042 pixels (for **Figures 4, 5a-i**), or on an
1047 EMCCD (Andor IXON ULTRA 897) with 512x512 pixels (for **Figures 3, 6d-f**). Both
1048 cameras were controlled by MicroManager software⁶². For experiments using the
1049 sCMOS camera, the effective pixel size was 108 nm and we used a 512x512 region of
1050 interest, which resulted in an imaged FoV of 55.3 μm x 55.3 μm . For experiments
1051 using the EMCCD camera, we used a 2x telescope and the effective pixel size was
1052 107 nm, resulting in a FoV of 54.8 μm x 54.8 μm . The exposure time was set to Δt
1053 =10 ms or 30 ms per frame. The number of frames acquired ranged from $k=1,000$
1054 (**Figure 4**) to $K=60,000$ (e.g. **Figure 5c**) per FoV.

1055 For the DNA-PAINT experiment (**Figure 5j,l**), we used an inverted Nikon Ti-E
1056 Eclipse microscope equipped with a 100x 1.49 NA TIRF objective and with the
1057 Perfect Focus System active. A 561 nm wavelength laser with 500 mW power was
1058 used to excite Cy3 dyes. Highly inclined laser illumination was used to reduce out-
1059 of-focus background signal. Images were acquired on an EMCCD camera as above,
1060 with a 1.5 x telescope, resulting in an effective pixel size of 106 nm and a FoV of
1061 54 μm x 54 μm . The sample was mounted in a magnetic sample holder filled with
1062 the imaging buffer provided with the Ultivue kit. Exposure time was set to $\Delta t =30$ ms
1063 and the EM gain of the EMCCD was set to 300. The laser power was increased until
1064 isolated fluorescent spots were observed. For the experiment shown in **Figure 5g,i**,
1065 $K=60,000$ frames were acquired.

1066 The *Xenopus* nuclear pore data (**Figure 6a-c** and **Supplementary**
1067 **Figure 14**), were acquired on a Zeiss Elyra P.S.1 microscope as described
1068 previously³⁶.

1069 For high-throughput imaging of microtubules (**Figure 4**), we used the Multi-
1070 Dimensional Acquisition tool in Micro-manager to define the positions of 1,089 FoVs
1071 of 55.3 μm x 55.3 μm on a 33x33 grid, with overlaps of 1 μm ; the stage was
1072 automatically shifted to each of these 1,089 positions. We first acquired only
1073 widefield images, taking five frames at each of these positions (the first two were
1074 ignored because of motion blur), in a total acquisition time of 12 minutes. Then, the
1075 laser power was raised to bleach out preactivated molecules and $k=1,000$ frames of
1076 single molecule images were acquired at each of the 1,089 positions, in a total
1077 acquisition time of 3 hours and 8 minutes. Raw image frames were written directly
1078 to a remote storage server via Samba networking protocol.

1079

1080 **Localization microscopy image analysis**

1081 The input to ANNA-PALM reconstruction is a localization image, defined as a 2D
1082 histogram of n single molecule positions $(x_i, y_i)_{i=1..n}$. The histogram bin, i.e. the
1083 pixel size of the localization image, was set to 7.8 nm for the simulated data
1084 (**Figure 2** and **Supplementary Figures 1-6,15**) and 20 nm for the experimental
1085 data (**Figures 3-6** and **Supplementary Figures 7-14**). The positions $(x_i, y_i)_{i=1..n}$
1086 were obtained by analyzing sequences of diffraction limited frames using standard
1087 single molecule localization algorithms. For experimental microtubule images, we
1088 used the ThunderSTORM⁶³ plugin of ImageJ, applying wavelet filters for detection
1089 and weighted least squares Gaussian fitting for precise estimation of subpixelic
1090 positions. We used the cross-correlation feature in ThunderSTORM for drift
1091 correction, and filtered out the least certain localizations based on the fitted

1092 Gaussian's standard deviation and the χ^2 of the residual. Localizations in
1093 consecutive frames separated by less than 20 nm were assumed to originate from
1094 the same molecule and merged into a single localization. The final number n of
1095 localizations was ~ 7 million for the full $55\ \mu\text{m} \times 55\ \mu\text{m}$ FoV of the images shown in
1096 **Figure 3** and **Supplementary Figures 8,9** (obtained from $K=30,000$ frames). For
1097 the high-throughput experiment (**Figure 4** and **Supplementary Figure 12**), the
1098 number of localizations per $55\ \mu\text{m} \times 55\ \mu\text{m}$ FoV ranged from $n=2,949$ to
1099 $n=1,442,048$ with an average $\langle n \rangle = 610,983$ and standard deviation $\sigma(n) = 273,606$.
1100 The total number of localizations across all 1,089 FoVs was ≈ 665 million.
1101 ThunderSTORM analyses were performed either on high end workstations or on
1102 Institut Pasteur's high performance computer (HPC) cluster. For the high-
1103 throughput experiments, we used Python scripts to run ThunderSTORM in batch
1104 mode (without user intervention) on the HPC cluster and assembled mosaic images
1105 (**Figure 4a,b** and **Supplementary Figure 12a,b**) using a stitching plugin of
1106 ImageJ⁶⁴.

1107 The nuclear pore images were analyzed using the ZEN software from Zeiss as
1108 previously described³⁶. For the DNA-PAINT experiments, we used PALMTT, a
1109 modified version of the single molecule tracking algorithm MTT⁶⁵, based on Matlab
1110 (Mathworks). This algorithm uses Gaussian smoothing and thresholding for
1111 detection, and Gaussian fitting for precise estimation of subpixelic positions. Drift
1112 correction was performed computationally by tracking fluorescent beads used as
1113 fiducial markers.

1114

1115 **Quality metrics and sampling resolution**

1116 In order to quantitatively assess the quality of PALM images and ANNA-PALM
1117 reconstructions, we calculated the multi-scale structural similarity index (MS-SSIM)
1118 between either image and the ground truth (**Figure 2g** and **Supplementary**
1119 **Figures 5,9**). For the simulated data, the ground truth was simply defined as the
1120 “perfect” PALM image, corresponding to an infinite number of localizations (see
1121 ‘Image simulations’ above, **Figure 2e** and **Supplementary Figure 1c**). For the
1122 experimental data, the ground truth was defined as the ANNA-PALM reconstruction
1123 of a dense PALM image obtained from all available frames (e.g. **Supplementary**
1124 **Figure 9c**). Before calculation of the MS-SSIM, all simulated images were linearly
1125 normalized without clipping to a maximum value of 255.

1126 In order to evaluate the effect of sampling on the resolution of PALM images,
1127 we computed the double mean distance, $R_{\text{Nyq}} = 2\langle d \rangle$ between nearest neighbors in
1128 the underlying sets of localizations⁴⁹ as function of localization number
1129 (**Supplementary Figure 3d**). For the simulated sparse PALM data, sets of
1130 localizations were obtained by interpreting each image \mathbf{S} as a 2D histogram of
1131 localizations, and creating a random subpixelic position $(x_k, y_k)_{k=1..m}$ within each
1132 pixel (i, j) , as many times as given by the pixel value $m = S(i, j)$ (therefore resulting
1133 in a set of $n = \sum_{i,j} S(i, j)$ localizations). The quantity $R_{\text{Nyq}}(n) = 2\langle d(n) \rangle$ decreases
1134 towards zero with increasing number of localizations, n . A Nyquist criterion
1135 introduced in ref.⁴⁹ suggests that the resolution is limited by sampling to no less
1136 than R_{Nyq} , implying that at least $n \geq N_{\text{Nyq}} = R_{\text{Nyq}}^{-1}(R)$ localizations are needed to
1137 achieve a given resolution R . However, a more stringent and realistic criterion³

1138 prescribes a five-fold larger number of localizations to reach resolution R :
1139 $n \geq N_{5 \times Nyq} = 5 \times N_{Nyq}$, implying that the sampling limit to resolution is
1140 $R_{5 \times Nyq} = 2\langle d(n/5) \rangle$. Accordingly, if this condition is met, the resolution is no longer
1141 limited by sampling, but by the localization precision, $R_{loc} \approx 2.3\sigma_{loc}$, where σ_{loc} is
1142 the standard deviation of localization errors along each coordinate. In general, the
1143 resolution of a PALM image, as limited by both sampling and localization precision,
1144 can be written: $R = \max(R_{5 \times Nyq}, R_{loc}) = \max(2\langle d(n/5) \rangle, 2.3\sigma_{loc})$.

1145

1146 **Life Sciences Reporting Summary.**

1147 Further information is available in the Life Sciences Reporting Summary.

1148

1149 **Code availability statement**

1150 The source code of ANNA-PALM is available from <https://annapalm.pasteur.fr/>.

1151

1152 **Data availability statement**

1153 The localization data used in this paper can be downloaded directly from

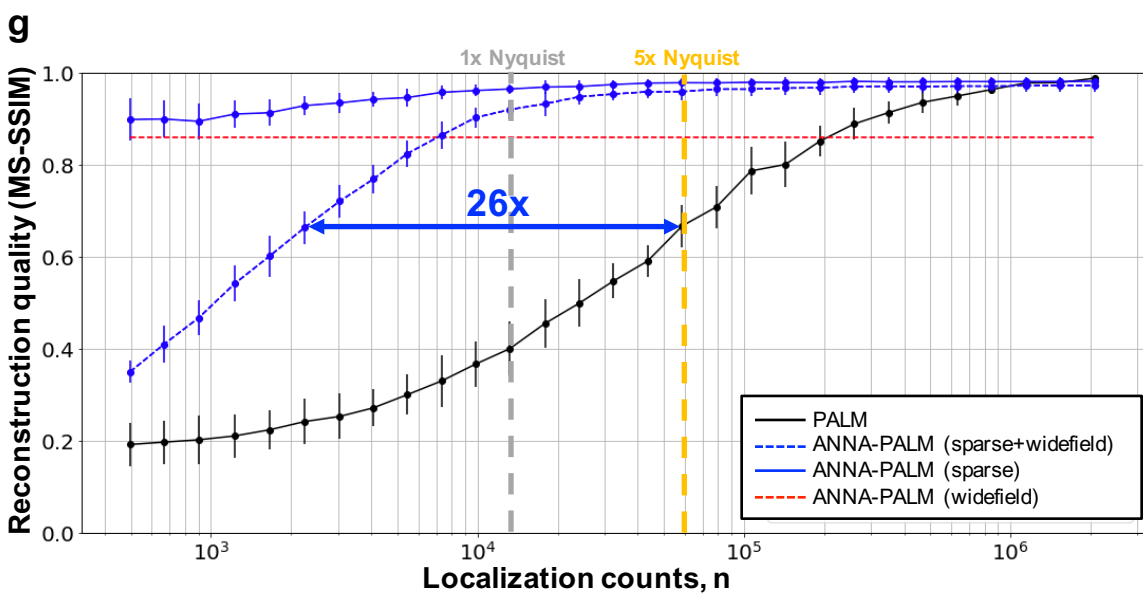
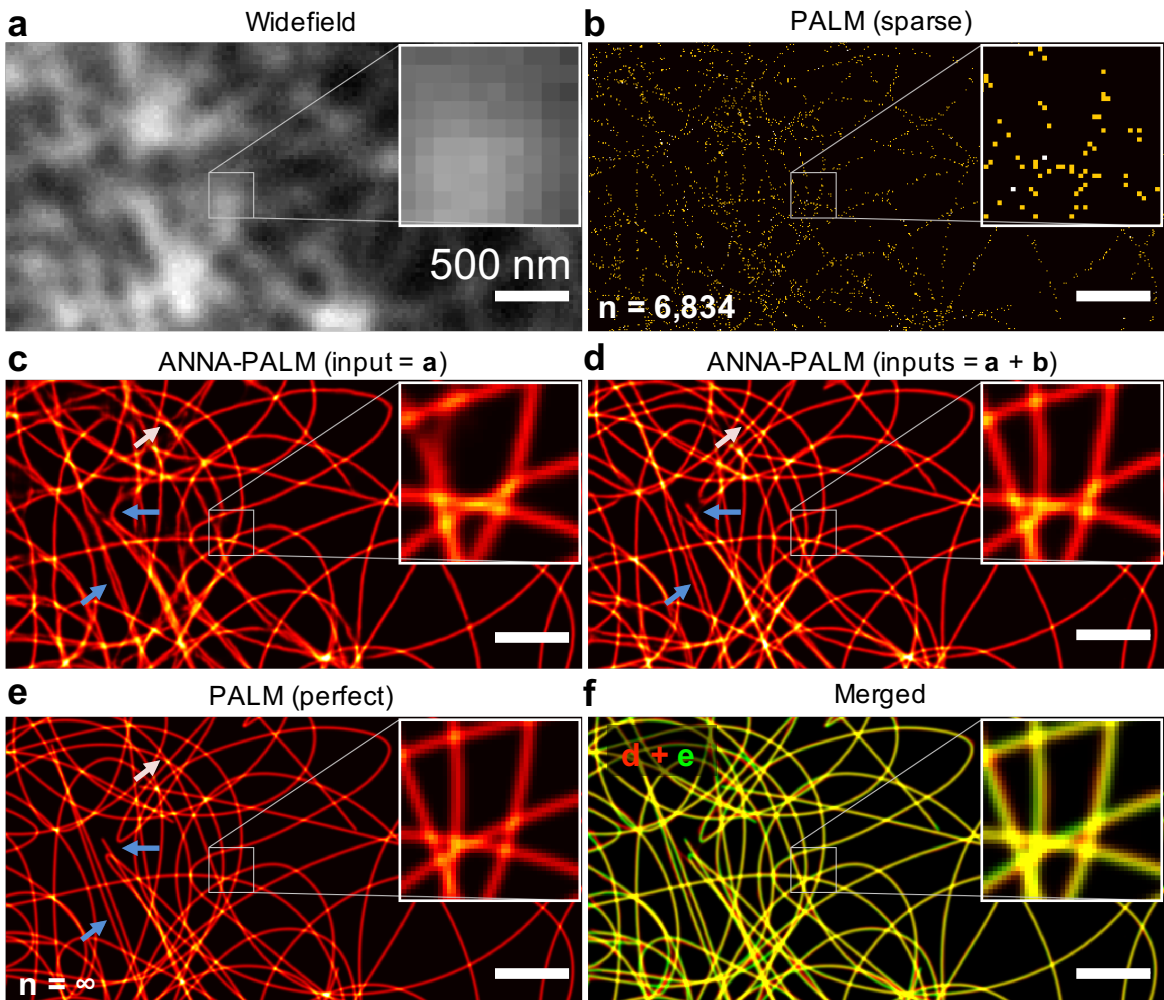
1154 <https://annapalm.pasteur.fr/>.

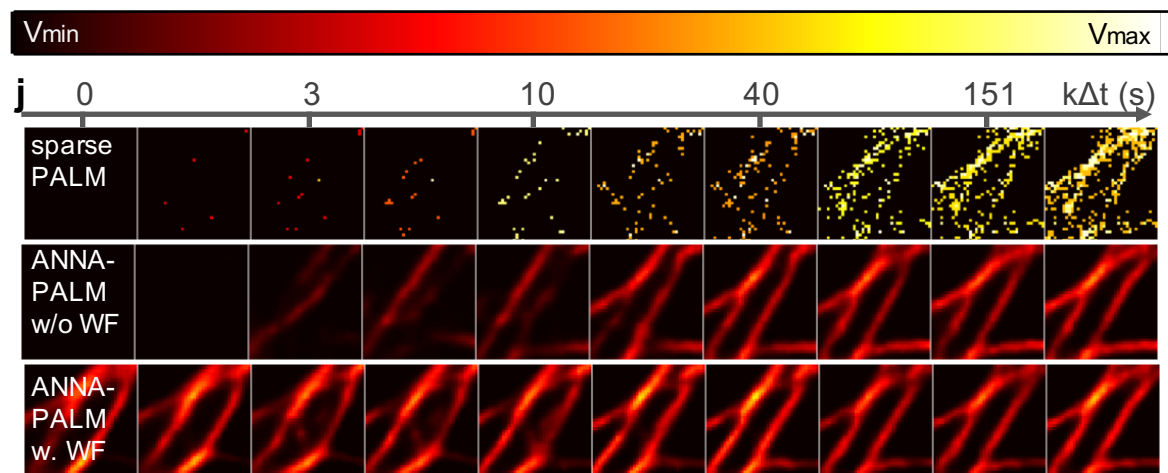
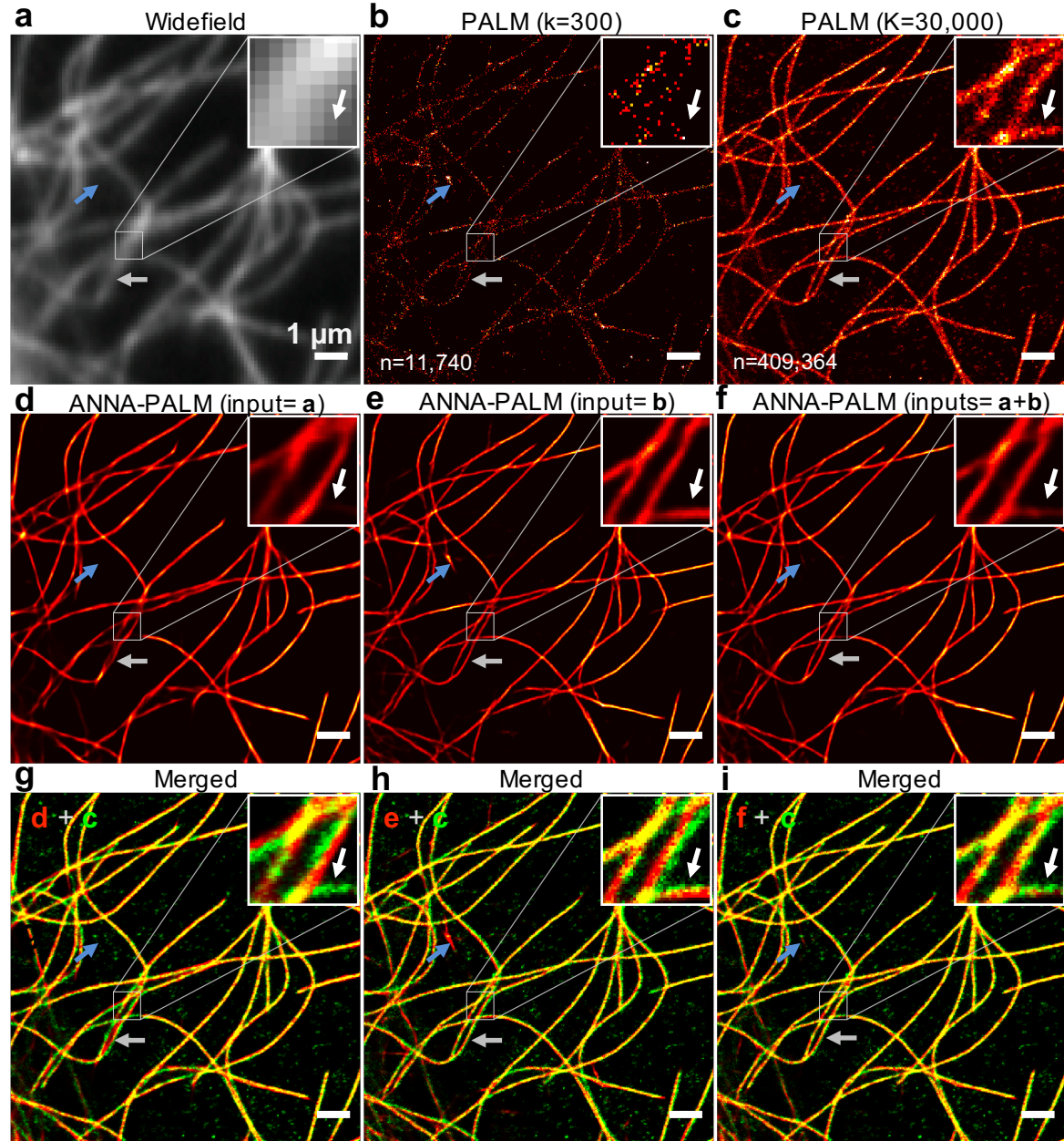
1155

1156 **Methods-only references**

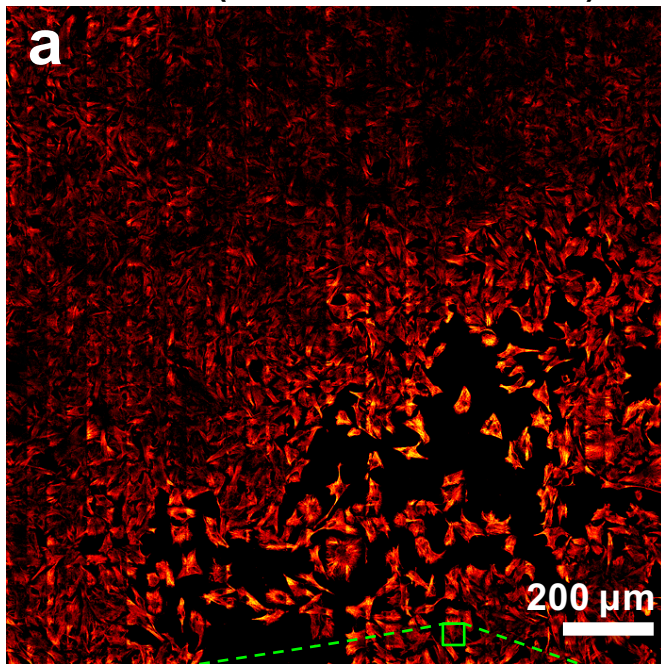
- 1157 51. Xu, L., Choy, C. S. & Li, Y. W. Deep sparse rectifier neural networks for speech
1158 denoising. in *2016 International Workshop on Acoustic Signal Enhancement,*
1159 *IWAENC 2016* (2016). doi:10.1109/IWAENC.2016.7602891
1160 52. Maas, A. L., Hannun, A. Y. & Ng, A. Y. Rectifier Nonlinearities Improve Neural
1161 Network Acoustic Models. *Proc. 30 th Int. Conf. Mach. Learn.* (2013).
1162 53. Mao, X. *et al.* Least Squares Generative Adversarial Networks. in *ICCV 2794–*
1163 *2802* (2017). doi:10.1109/ICCV.2017.304

- 1164 54. Kingma, D. P. & Ba, J. Adam: A Method for Stochastic Optimization. *ICLR* 1–15
1165 (2015).
1166 doi:<http://doi.acm.org.ezproxy.lib.ucf.edu/10.1145/1830483.1830503>
1167 55. Rampasek, L. & Goldenberg, A. TensorFlow: Biology’s Gateway to Deep
1168 Learning? *Cell Syst.* **2**, 12–14 (2016).
1169 56. Srinivasa Reddy, B. & Chatterji, B. N. An FFT-based technique for translation,
1170 rotation, and scale-invariant image registration. *IEEE Trans. Image Process.* **5**,
1171 1266–1271 (1996).
1172 57. Simard, P. Y., Steinkraus, D. & Platt, J. C. Best practices for convolutional neural
1173 networks applied to visual document analysis. *Seventh Int. Conf. Doc. Anal.*
1174 *Recognition, 2003. Proceedings.* **1**, 958–963 (2003).
1175 58. Plimpton, S. Fast Parallel Algorithms for Short-Range Molecular Dynamics. *J.*
1176 *Comput. Phys.* **117**, 1–19 (1995).
1177 59. van de Linde, S. *et al.* Direct stochastic optical reconstruction microscopy with
1178 standard fluorescent probes. *Nat. Protoc.* **6**, 991–1009 (2011).
1179 60. Henriques, R. *et al.* QuickPALM: 3D real-time photoactivation nanoscopy
1180 image processing in ImageJ. *Nat. Methods* **7**, 339–340 (2010).
1181 61. Lelek, M. *et al.* Superresolution imaging of HIV in infected cells with FLAsH-
1182 PALM. *Proc. Natl. Acad. Sci. U. S. A.* **109**, 8564–9 (2012).
1183 62. Edelstein, A., Amodaj, N., Hoover, K., Vale, R. & Stuurman, N. Computer control
1184 of microscopes using manager. *Current Protocols in Molecular Biology* (2010).
1185 doi:10.1002/0471142727.mb1420s92
1186 63. Ovesny, M., Kiek, P., Borkovec, J., Vindrych, Z. & Hagen, G. M. ThunderSTORM:
1187 a comprehensive ImageJ plug-in for PALM and STORM data analysis and
1188 super-resolution imaging. *Bioinformatics* **30**, 2389–2390 (2014).
1189 64. Preibisch, S., Saalfeld, S. & Tomancak, P. Globally optimal stitching of tiled 3D
1190 microscopic image acquisitions. *Bioinformatics* **25**, 1463–1465 (2009).
1191 65. Sergé, A., Bertaux, N., Rigneault, H. & Marguet, D. Dynamic multiple-target
1192 tracing to probe spatiotemporal cartography of cell membranes. *Nat Methods*
1193 **5**, 687–694 (2008).
1194
1195





PALM ($k=1000 \times 1089$, $t=3.1\text{h}$)



ANNA-PALM ($t=3.1\text{h}$)

